

THÈSE

présentée devant

L'Université de Valenciennes et du Hainaut-Cambrésis

pour obtenir

LE GRADE DE DOCTEUR

SPÉCIALITÉ : AUTOMATIQUE, GÉNIE INFORMATIQUE, TRAITEMENT DU SIGNAL
ET DES IMAGES

par

Christine Boydev

Ingénieure ENSPG et Physicienne médicale

**Automatic segmentation of cone-beam computed
tomography images for prostate cancer radiation therapy**

soutenue le

xx xx 2015

Ecole doctorale :

Sciences Pour l'Ingénieur (SPI)

Laboratoires :

Laboratoire d'Automatique, de Mécanique et d'Informatique Industrielles et Humaines (LAMIH,
UVHC, Valenciennes, France)

et

Laboratoire de Traitement des Signaux 5 (LTS5, EPFL, Lausanne, Suisse)

Jury :

David Sarrut	Directeur de recherche, CNRS, Lyon	Rapporteur
Youcef Chahir	Maître de conférence, CNRS, Caen	Rapporteur
David Pasquier	Radiothérapeute, Centre Oscar Lambret, Lille	Examineur
Foued Derraz	Enseignant-chercheur, Faculté Libre de Médecine, Lille	Examineur
Abdelmalik Taleb-Ahmed	Professeur, UVHC, Valenciennes	Directeur de thèse
Jean-Philippe Thiran	Professeur, EPFL, Lausanne	Co-directeur de thèse

Invité :

Loïc Dibout Ingénieur d'Application, ELEKTA SAS, Paris

Acknowledgments

Résumé

Dans le contexte du traitement du cancer de la prostate, l'utilisation de la tomodensitométrie à faisceau conique (CBCT) pour la radiothérapie guidée par l'image, éventuellement adaptative, présente certaines difficultés en raison du faible contraste et du bruit important dans les images pelviennes. L'objectif principal de cette thèse est d'apporter des contributions méthodologiques pour le recalage automatique entre l'image scanner CT de référence et l'image CBCT acquise le jour du traitement.

La première partie de nos contributions concerne le développement d'une stratégie de correction du positionnement du patient à l'aide du recalage rigide (RR) CT/CBCT. Nous avons comparé plusieurs algorithmes entre eux : (a) RR osseux, (b) RR osseux suivi d'un RR local dans une région qui correspond au clinical target volume (CTV) de la prostate dans l'image CT élargie d'une marge allant de 1 à 20 mm. Une analyse statistique complète des résultats quantitatifs et qualitatifs utilisant toute la base de données, composée de 115 images cone beam computed tomography (CBCT) et de 10 images computed tomography (CT) de 10 patients atteints du cancer de la prostate, a été réalisée. Nous avons également défini une nouvelle méthode pratique pour automatiquement estimer la distension rectale produite dans le voisinage de la prostate entre l'image CT et l'image CBCT. A l'aide de notre mesure de distension rectale, nous avons évalué l'impact de la distension rectale sur la qualité du RR local et nous avons fourni un moyen de prédire les échecs de recalage. Sur cette base, nous avons élaboré des recommandations concernant l'utilisation du RR automatique pour la localisation de la prostate sur les images CBCT en pratique clinique.

La seconde partie de la thèse concerne le développement méthodologique d'une nouvelle méthode qui combine le recalage déformable et la segmentation. Pour contourner le problème du faible rapport qualité/bruit dans les images CBCT qui peut induire le processus de recalage en erreur, nous avons imaginé une nouvelle énergie composée de deux termes : un terme de similarité globale (la corrélation croisée normalisée (NCC) a été utilisée, mais tout autre mesure de similarité pourrait être utilisée à la place) et un terme de segmentation qui repose sur une adaptation locale du modèle de l'image homogène par morceaux de Chan-Vese utilisant un contour actif dans l'image CBCT. Notre but principal était d'améliorer la précision du recalage comparé à une énergie constituée de la NCC seule. Notre algorithme de recalage est complètement automatique et accepte comme entrées (1) l'image CT de planification, (2) l'image CBCT du jour et (3) l'image binaire associée à l'image CT et correspondant à l'organe d'intérêt que l'on cherche à segmenter dans l'image CBCT au cours du recalage.

Summary

The use of CBCT imaging for image-guided radiation therapy (IGRT), and beyond that, image-guided adaptive radiation therapy (IGART), in the context of prostate cancer is challenging due to the poor contrast and high noise in pelvic CBCT images. The principal aim of the thesis is to provide methodological contributions for automatic intra-patient image registration between the planning CT scan and the treatment CBCT scan.

The first part of our contributions concerns the development of a CBCT-based prostate setup correction strategy using CT-to-CBCT rigid registration (RR). We established a comparison between different RR algorithms: (a) global RR, (b) bony RR, and (c) bony RR refined by a local RR using the prostate CTV in the CT scan expanded with 1-to-20-mm varying margins. A comprehensive statistical analysis of the quantitative and qualitative results was carried out using the whole dataset composed of 115 daily CBCT scans and 10 planning CT scans from 10 prostate cancer patients. We also defined a novel practical method to automatically estimate rectal distension occurred in the vicinity of the prostate between the CT and the CBCT scans. Using our measure of rectal distension, we evaluated the impact of rectal distension on the quality of local RR and we provided a way to predict registration failure. On this basis, we derived recommendations for clinical practice for the use of automatic RR for prostate localization on CBCT scans.

The second part of the thesis provides a methodological development of a new joint segmentation and deformable registration framework. To deal with the poor contrast-to-noise ratio in CBCT images likely to misguide registration, we conceived a new metric (or energy) which included two terms: a global similarity term (the normalized cross correlation (NCC) was used, but any other one could be used instead) and a segmentation term based on a localized adaptation of the piecewise-constant region-based model of Chan-Vese using an evolving contour in the CBCT image. Our principal aim was to improve the accuracy of the registration compared with an ordinary NCC metric. Our registration algorithm is fully automatic and takes as inputs (1) the planning CT image, (2) the daily CBCT image and (3) the binary image associated with the CT image and corresponding to the organ of interest we want to segment in the CBCT image in the course of the registration process.

Contents

List of figures	14
List of tables	15
List of abbreviations and acronyms	17
1 Introduction: medical and scientific context	19
1.1 Prostate cancer	20
1.1.1 Anatomy	20
1.1.2 Epidemiology	20
1.1.3 Symptoms	21
1.1.4 Types of prostate cancer	23
1.1.5 Screening	23
1.1.6 Diagnosis	23
1.1.7 Treatments	24
1.2 Radiotherapy	25
1.2.1 Types	25
1.2.2 Brief history of radiotherapy	25
1.2.3 Definition of volumes	26
1.2.4 Workflow of radiotherapy	27
1.2.5 Radiation Fractionation	29
1.2.6 Image guidance	29
1.3 Principles of image registration	33
1.4 Contributions and organization of the manuscript	37
Bibliography	39
2 Data preparation	47
2.1 Data description	48
2.2 Shape-based interpolation of a set of two-dimensional (2D) slices	49
2.2.1 Material and methods	49
2.2.2 Results	51
2.2.3 Conclusion	53
Bibliography	54

3	Development of CBCT-based prostate setup correction strategies and impact of rectal distension	55
3.1	Background	56
3.2	Methods	57
3.2.1	Data description	57
3.2.2	Registration algorithm	57
3.2.3	Software	59
3.2.4	Validation	59
3.2.5	Treatment margin calculations	62
3.3	Results	64
3.3.1	Without applying a replace-gas-by-tissue filter	64
3.3.2	Application of a replace-gas-by-tissue filter to improve registration quality	67
3.4	Discussion	77
3.5	Conclusion	80
	Bibliography	81
4	A new energy for joint segmentation and deformable registration	87
4.1	Background	88
4.2	Methods	92
4.2.1	Description of the proposed model	93
4.2.2	Implementation	99
4.2.3	Dosimetric considerations	101
4.3	Results	102
4.3.1	Preliminary segmentation study based on local statistics	102
4.3.2	The proposed method	106
4.4	Conclusion	111
	Bibliography	112
5	Conclusions and perspectives	115
5.1	Contributions	115
5.2	Perspectives	117
	Bibliography	119
	Appendices	123
	CV	135

List of Figures

1.1	Side view of the prostate and nearby organs (source: https://en.wikipedia.org/wiki/Prostate_cancer)	20
1.2	Numbers of new prostate cancer cases and deaths in Europe in 2012, for males and females separately (source: GLOBOCAN project, International Agency for Research on Cancer (IARC))	21
1.3	Estimated prostate cancer incidence and mortality in Europe in 2012, for males and females separately (source: GLOBOCAN project, IARC)	22
1.4	Illustration of a prostate cancer pressing on the prostatic urethra (source: https://en.wikipedia.org/wiki/Prostate_cancer)	23
1.5	Schematic representation of the volumes of interest (VOIs), as defined by the ICRU 50 and 62 reports for use in radiation treatment planning and dose reporting [Podgorsak 2003]	27
1.6	Example of the volumes of interest (VOIs) on a CT for a prostate treatment plan (source: [Podgorsak 2003])	28
1.7	Schematic representation of the benefit of applying off-line, and a fortiori on-line, imaging protocols for treatment position verification and correction with respect to systematic and random errors, and hence treatment margin sizes (source: [Hoskin 2008])	30
1.8	Schematic representation of the conventional, fan-beam geometry and the cone-beam geometry (source: [Scarfe & Farman 2008]).	31
1.9	Illustration of a linear accelerator (linac)-mounted kilovolts (kV) CBCT system	31
1.10	Example of (a) a planning CT scan and (b) a treatment CBCT scans for prostate cancer.	32
1.11	A general view of adaptive radiation therapy. The black arrows indicate the possible points of feedback (source: [Chen <i>et al.</i> 2006]).	33
1.12	The basic components of the registration framework are two input images (fixed and moving), a metric, an optimizer, a transform and an interpolator (source: [Ibanez <i>et al.</i> 2013]).	34
2.1	The different steps in our shape-based interpolation method.	49
2.2	3D views of (a) the cone manually drawn, (b) the same cone but with missing contours, and (c) the interpolated cone. The display software used is ParaView (http://www.paraview.org/) [Henderson 2007].	52

2.3	(a) 2D central view of the cone before interpolation. (b) Overlay of 2D central views of the original and interpolated cones. The display software used is VV (http://vv.creatis.insa-lyon.fr/) [Rit <i>et al.</i> 2011]. The display interpolation is purposely deactivated here.	52
2.4	Interpolation of a prostate binary image derived from the manual segmentation of a clinical gray-value CBCT image. 3D views of the prostate (a) before interpolation and (b) after interpolation. The display software used is ParaView (http://www.paraview.org/) [Henderson 2007].	53
3.1	Rigid registration pipeline.	58
3.2	Pre-processing pipeline.	60
3.3	Slice of a CT scan. The manual contours of (red) the prostate and (green) the rectum, as well as (brown) the ROI defined as the prostate gland extended with a margin of 8mm. The rectal distension occurred between the CT and the CBCT scans was estimated by calculating the value of F as defined in Equation 3.2. $\bar{I}_{CT,p}$ ($\bar{I}_{CBCT,p}$) was calculated within the red region on the CT (CBCT after bony rigid alignment) scan. $\bar{I}_{CT,r}$ ($\bar{I}_{CBCT,r}$) was calculated within the intersection of the green and the brown regions on the CT (CBCT after bony rigid alignment) scan.	62
3.4	The procedure followed to compare the different CBCT-based prostate setup correction strategies and evaluate their dosimetric impact. The dose-volume histograms (DVHs) for a given fraction (i.e. using a given treatment-day CBCT) obtained with the different strategies are compared.	63
3.5	Example of manual and automatic prostate contours produced by bony and 8-mm local RRs displayed on top of the corresponding CBCT image in the (a) axial, (b) coronal and (c) sagittal planes.	65
3.6	Outcome (success or failure) of 8-mm local RR	66
3.7	Success/failure results for all the RR methods w.r.t. the CT/CBCT pairs sorted in order of increasing F number (as defined in Equation 3.2) with or without the application of a replace-gas-by-tissue filter.	70
3.7	Success/failure results for all the RR methods w.r.t. the CT/CBCT pairs sorted in order of increasing F number (as defined in Equation 3.2) with or without the application of a replace-gas-by-tissue filter.	71
3.7	Success/failure results for all the RR methods w.r.t. the CT/CBCT pairs sorted in order of increasing F number (as defined in Equation 3.2) with or without the application of a replace-gas-by-tissue filter.	72
3.8	Slice of the planned dose distribution for Patient A for (a) the first intensity-modulated arc therapy (IMAT) course and (b) the second IMAT course. . .	73
3.9	Patient A - 1st course: Comparison of the DVH obtained by bony RR and all local RR methods. To compute the DVHs, the manual CBCT contours are mapped onto the planned dose map using the different setup correction strategies (see Figure 3.4). The planned DVHs are also shown.	74
3.10	Patient A - 2nd course: Comparison of the DVH obtained by bony RR and all local RR methods. To compute the DVHs, the manual CBCT contours are mapped onto the planned dose map using the different setup correction strategies (see Figure 3.4). The planned DVHs are also shown.. . . .	75
3.11	Patient B - 1st course: Comparison of the DVH obtained by bony RR and all local RR methods. To compute the DVHs, the manual CBCT contours are mapped onto the planned dose map using the different setup correction strategies (see Figure 3.4). The planned DVHs are also shown.. . . .	76

4.1	Transverse slices of CBCT scans with (A) empty rectum (visible prostate), (B) rectum containing feces and small gas pockets (visible prostate), (C) rectum with moving gas pocket (streak artifacts; hardly visible prostate), and (D) rectum with feces and a slightly moving gas pocket (white streak artifacts at gas pocket edges; large part of prostate is visible). (figure extracted from [Smitsmans <i>et al.</i> 2008])	88
4.2	Lankton <i>et al.</i> propose a localized version of region-based segmentation energies where image statistics are calculated in the neighborhood of each point along the evolving contour, divided into (a) a local interior shaded in red and (b) an a local exterior shaded in red. (figure extracted from [Lankton & Tannenbaum 2008])	91
4.3	Different coordinate systems (the index grid and the physical coordinate system) are involved in the registration process. In the ITK registration framework, the transformation being optimized is the one mapping from the physical space of the fixed image into the physical space of the moving image. (figure extracted from [Ibanez <i>et al.</i> 2005])	100
4.4	The procedure followed to estimate the dose that would be delivered to the organs on the day of the treatment. The deformation field resulting from the “RR+DIR“ (which stands for rigid registration + deformable image registration) enables the automatic segmentation of the CBCT image. After rigidly aligning the CBCT image with the planning CT using a setup correction strategy, the DVHs of the segmentations of the organs from the CBCT image are calculated using the planned dose distribution. The DVHs for a given fraction (i.e. using a given treatment-day CBCT) can be compared to the planned DVHs, obtained using the planned dose distribution and the manual CT segmentations, in order to help make a decision on whether adapting the treatment is necessary.	102
4.5	Prostate segmentation of a CBCT slice using an adaptation of the region segmentation model of Chan and Vese with local statistics based on local image statistics, as proposed by [Lankton & Tannenbaum 2008]. Figure (a) shows the prostate contour drawn manually (ground truth), Figure (b) shows the initialization and Figures (c)-(k) show the resulting segmentations using different localizing radii.	104
4.6	Rectum segmentation of a CBCT slice using an adaptation of the region segmentation model of Chan and Vese with local statistics based on local image statistics, as proposed by [Lankton & Tannenbaum 2008]. Figure (a) shows the rectum contour drawn manually, Figure (b) shows the initialization and Figures (c)-(h) show the resulting segmentations using different localizing radii.	105
4.7	Bladder segmentation of a CBCT slice using an adaptation of the region segmentation model of Chan and Vese with local statistics based on local image statistics, as proposed by [Lankton & Tannenbaum 2008]. Figure (a) shows the prostate contour drawn manually, Figure (b) shows the initialization and Figures (c)-(i) show the resulting segmentations using different localizing radii.	106

4.8	Initialization of the evolving contour used for the calculation of the segmentation term of the proposed model superimposed on the same CBCT image slice as that in Figure 4.5. The initialization corresponded to the automatic CBCT contour obtained after propagation of the manual CT prostate contour using a bony RR. Only one evolving contour was involved in the registration process, but in an extended, future version of this model, three evolving contours could be involved simultaneously.	107
4.9	Slice of a CT scan with the corresponding prostate contours: (red) the manual contour drawn by the radiation oncologist, (yellow) the automatic contour obtained with a bony RR serving as initialization for the evolving contour of the proposed method, (blue) the automatic contour obtained with an ordinary NCC deformable image registration (DIR) and (green) the automatic contour obtained with the proposed method using a 2-mm radius. We note that the automatic contours are presented onto the fixed image, that is, the CT image, as the transformation that is optimized by the registration is the one mapping from the fixed image to the moving image. .	108
4.10	Sequence of the values of the different terms constituting the total energy at each iteration during (a)-(b) the optimization process of the proposed method using $\lambda = 1$ and $\mu = 10^{-10}$, and (c) an ordinary NCC DIR. Figure (d) shows the evolution of the NCC throughout the iterative process for the two registrations (simple superimposition of (a) and (c)).	109
4.11	Comparison of the DVHs of (a) the CTV, (b) the rectum and (c) the bladder using (red dashed line) the manual segmentations and the automatic segmentations obtained with (blue line) the proposed method and (green line) the NCC DIR.	110

List of Tables

2.1	Illustration of the slice thickness and delineation ratio of the CT and CBCT images before and after shape-based interpolation	48
3.1	Dice results after CBCT-based setup correction using RR for 115 CT/CBCT pairs of 10 patients.	64
3.2	BD results after CBCT-based setup correction using RR for 115 CT/CBCT pairs of 10 patients.	65
3.3	Qualitative results after CBCT-based setup correction using RR for 115 CT/CBCT pairs of 10 patients.	66
3.4	Number of fractions and dose delivered in each course of the IMAT undergone by Patients A and B. The treatment is split into two courses. The first one treats the prostate, the lymph nodes and the seminal vesicles. The second one treats the prostate only.	67
3.5	Geometrical uncertainties (standard deviations of translations only) involved in prostate cancer treatment using CBCT daily image guidance.	68
3.6	Dice results after CBCT-based setup correction using RR for 115 CT/CBCT pairs of 10 patients. Before registration, air was replaced by soft tissue in images.	68
3.7	BD results after CBCT-based setup correction using RR for 115 CT/CBCT pairs of 10 patients. Before registration, air was replaced by soft tissue in images.	69
4.1	Results for the prostate after RR and DIR for Patient A.	107

List of abbreviations and acronyms

IARC International Agency for Research on Cancer

PSA prostate-specific antigen

DRE digital rectal examination

TRUS transrectal ultrasound

TRMR transrectal magnetic resonance

BPH benign prostatic hyperplasia

CT computed tomography

CBCT cone beam computed tomography

MRI magnetic resonance imaging

MR magnetic resonance

PET positron emission tomography

EBRT external beam radiotherapy

kV kilovolts

MV megavolts

linac linear accelerator

MLC multileaf collimator

2D two-dimensional

3D three-dimensional

4D four-dimensional

CRT conformal radiation therapy

IMRT intensity-modulated radiation therapy

IMAT intensity-modulated arc therapy

IGRT	image-guided radiation therapy
IGART	image-guided adaptive radiation therapy
ART	adaptive radiation therapy
ICRU	International Commission on Radiation Units and Measurements
GTV	gross tumor volume
CTV	clinical target volume
PTV	planning target volume
ITV	internal target volume
OAR	organ at risk
PRV	planning organ at risk volume
VOI	volume of interest
TPS	treatment planning system
DVH	dose-volume histogram
DOF	degree of freedom
RR	rigid registration
DIR	deformable image registration
SSD	sum of squared differences
SAD	sum of absolute differences
NCC	normalized cross correlation
DF	deformation field
ITK	Insight Segmentation and Registration Toolkit
ROI	region of interest
FFD	free-form deformation
BLD	bidirectional local distance
PDE	partial differential equation
BD	bidirectional distance

Introduction: medical and scientific context

Contents

2.1	Data description	48
2.2	Shape-based interpolation of a set of 2D slices	49
2.2.1	Material and methods	49
2.2.1.1	Implementation	49
2.2.1.2	Usage	51
2.2.1.3	Software requirements	51
2.2.2	Results	51
2.2.2.1	Example 1: Interpolation of a cone	51
2.2.2.2	Example 2: Interpolation of a clinical image	52
2.2.3	Conclusion	53
	Bibliography	54

1.1 Prostate cancer

1.1.1 Anatomy

The prostate is a gland of the male reproductive system. Its main function is to secrete part of the seminal fluid. It has the size of a walnut and the shape of a cone with its base pointing toward the cranial side and the apex toward the caudal side. It is located under the bladder, in front of the rectum and behind the penis (Figure 1.1). It surrounds the urethra which connects the bladder to the penis and carries urine as well as semen.

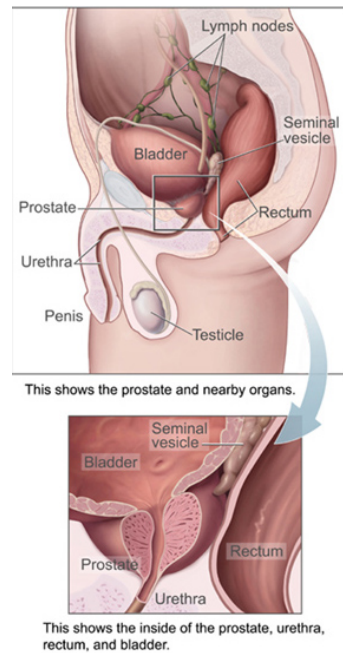


Figure 1.1: Side view of the prostate and nearby organs (source: https://en.wikipedia.org/wiki/Prostate_cancer)

1.1.2 Epidemiology

1.1.2.1 Key figures

Figures 1.2 and 1.3 are extracted from [public domain: <http://globocan.iarc.fr/Default.aspx>]. These graphs show the situation in Europe in 2012, but interested readers can learn more about what is happening in specific countries or on other continents on the GLOBOCAN's website. Indeed, the GLOBOCAN project, supported by the IARC (an intergovernmental agency created by the World Health Organization of the United Nations), provides contemporary estimates of the incidence of, mortality and prevalence from major types of cancer, at national level, for 184 countries of the world. One can create one's own graphs using GLOBOCAN data sorted by cancer, sex, and/or population.

As seen from Figure 1.2, prostate cancer is the second most commonly diagnosed cancer (with 400,364 new cases in Europe in 2012) after breast cancer, and the most common cancer in men. Nevertheless, prostate cancer is not the most deadly cancers. With 92,328 deaths in 2012, prostate cancer is two to four times less deadly than the two most deadly cancers (i.e. lung cancer with 353,848 deaths and colorectum cancer with 214,866), but it is approximately as deadly as **breast** cancer (131,347 deaths).

However, interestingly enough, it was reported that the probability of harbouring (whether diagnosed or not) prostate cancer and dying from it amounted to 3% [Hsing *et al.* 2000, Klotz & Emberton 2014]. In fact, many men are affected by slow growing/latent prostate

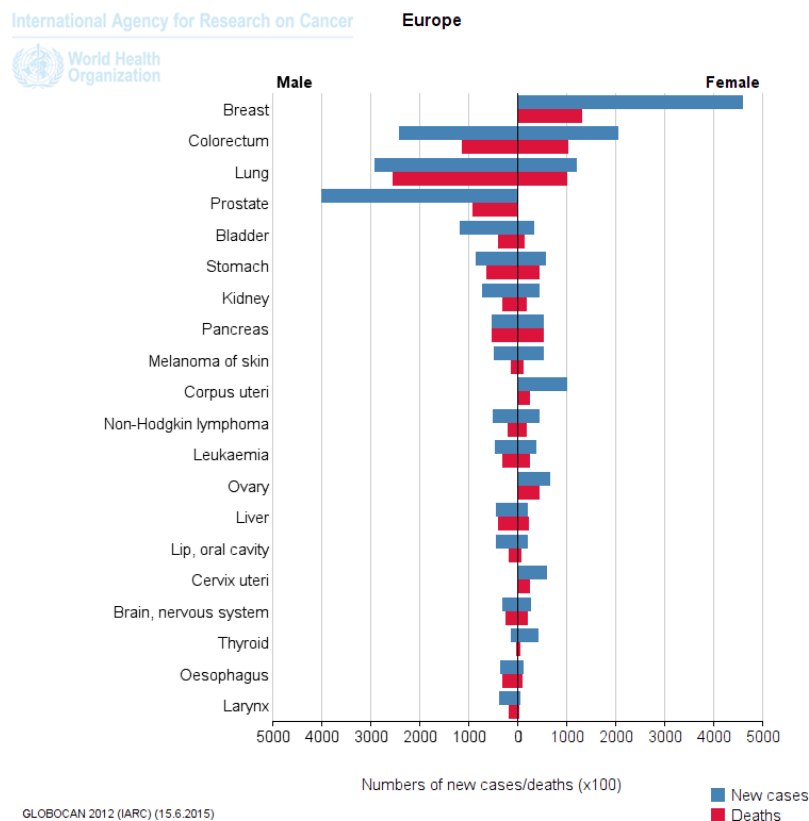


Figure 1.2: Numbers of new prostate cancer cases and deaths in Europe in 2012, for males and females separately (source: GLOBOCAN project, IARC)

cancer without knowing it, and furthermore, many men *never* know that they have prostate cancer. Autopsy studies of Chinese, German, Israeli, Jamaican, Swedish, and Ugandan men who died of other causes have found prostate cancer in 30% of men in their 50s, and in 80% of men in their 70s [Breslow *et al.* 1977].

1.1.2.2 Etiology

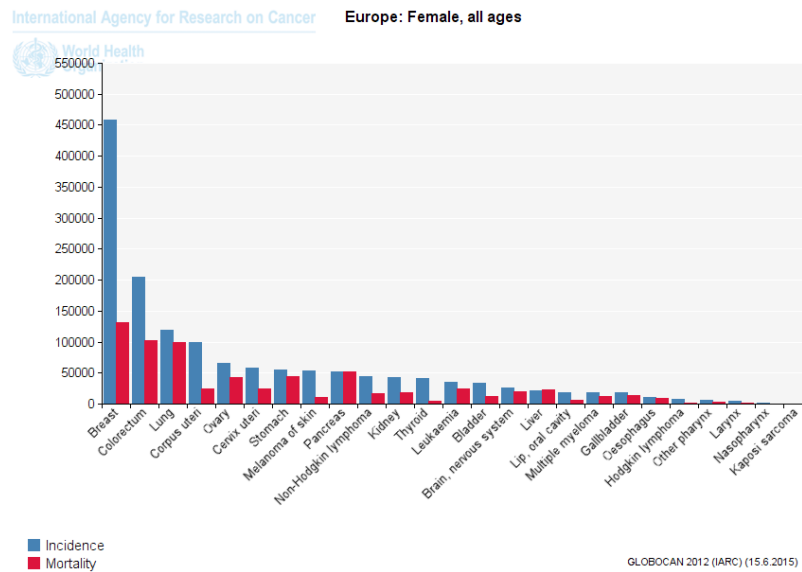
Despite its high prevalence, the etiology (the branch of medical science concerned with the causes and origins of diseases) remains poorly understood, compared to other common cancers such as breast and lung cancers. The only established risk factors are increasing age, skin color, and a family history of prostate cancer [Hsing & Chokkalingam 2006].

Incidence of prostate cancer is, moreover, increasing. The reasons for this are not precisely known, but increasing life expectancy, growing disease prevalence resulting from environmental carcinogens, and increasing use of novel diagnostic modalities have been pointed out. The most plausible explanation is probably the increasing efforts to detect the disease, which has led to considerable advances such as the introduction of prostate-specific antigen (PSA) screening tests (late 1980s) and transrectal ultrasound (TRUS)-guided biopsy technology.

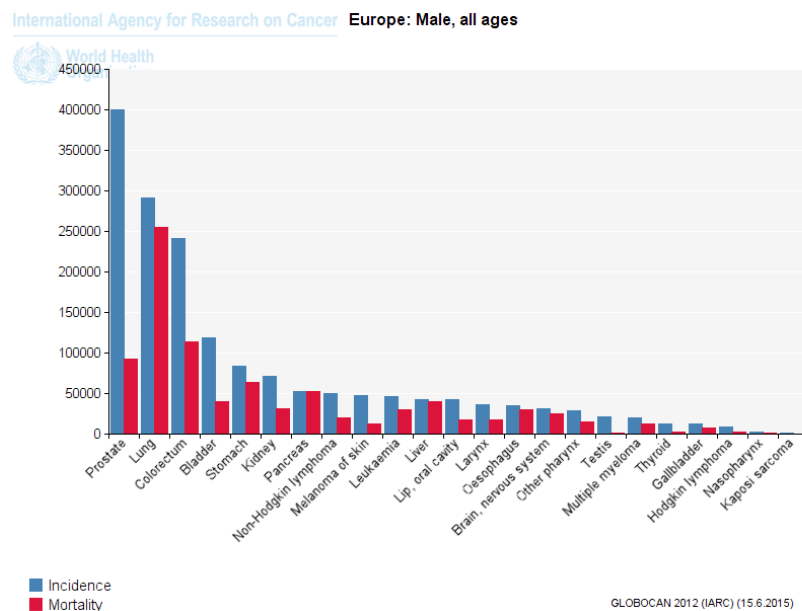
1.1.3 Symptoms

Early prostate cancer usually causes no symptoms. Symptoms appear when the prostate cancer presses on the prostatic urethra, as illustrated on Figure 1.4, causing the following problems:

- A need to urinate frequently



(a)



(b)

Figure 1.3: Estimated prostate cancer incidence and mortality in Europe in 2012, for males and females separately (source: GLOBOCAN project, IARC)

- A need to urinate urgently
- Difficulty starting or stopping a stream of urine
- Inability to urinate
- A weak or restricted stream of urine
- An interrupted stream of urine
- A feeling that the bladder has not been completely emptied
- A painful or burning sensation during urination or ejaculation
- Blood in urine or semen

These symptoms are not exclusively those of prostate cancer and can be caused by an enlarged, noncancerous prostate or by a urinary tract infection.

As the disease progresses and grows outside the prostate, it often first grows into nearby tissues (invasion) or spreads to nearby lymph nodes and lymph vessels, and subsequently spreads to the bones (metastasis), causing other symptoms such as bone pain (e.g., in the back, hips, pelvis or thighs), weight loss or fatigue.

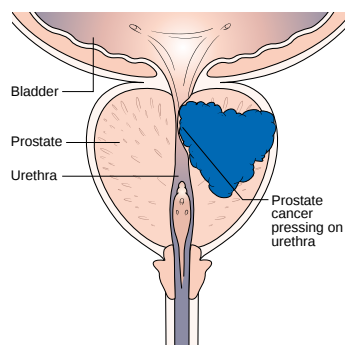


Figure 1.4: Illustration of a prostate cancer pressing on the prostatic urethra (source: https://en.wikipedia.org/wiki/Prostate_cancer)

1.1.4 Types of prostate cancer

More than 9 out of 10 prostate cancers are a type called acinar adenocarcinoma. It starts from gland cells in the prostate itself. Very often it is relatively slow growing and not likely to spread.

The remaining 1 in 10 prostate cancers are rare types. They can be classified according to the type of cells they start from. Some of them are listed below:

- Ductal adenocarcinoma starts from the cells that line the ducts (tubes) of the prostate gland. It tends to grow and spread more quickly than acinar adenocarcinoma.
- Urothelial cancer starts from the cells that line the urethra (transitional cells), more commonly, in the bladder, and spreads into the prostate.
- Squamous cell cancer starts from the flat cells that cover the prostate gland. It tends to grow and spread more quickly than adenocarcinoma of the prostate.

1.1.5 Screening

The purpose of screening tests is to detect early disease or risk factors for disease in large numbers of asymptomatic, apparently healthy, but potentially at risk individuals. Screening tests can only provide suspicion of a disease and need to be confirmed by a diagnostic test which provides a definite diagnosis.

1.1.6 Diagnosis

The purpose of a diagnostic test is to establish the presence or absence of a disease in an individual that has symptoms or that has no symptoms but has a positive screening test. There are three different steps in the process of diagnosing prostate cancer:

1. First noninvasive step (in case of screening or if the patient has symptoms):
 - The PSA test: it consists of a blood test that measures the level of the PSA, a protein released by the prostate gland. A high PSA level suggests an abnormal

activity in the prostate, which can be caused by a cancerous/noncancerous tumor, inflammation of the prostate, or benign prostatic hyperplasia (BPH), that is, an enlarged prostate gland due to old age. This test is able to detect early prostate cancer.

- The digital rectal examination (DRE): it consists of inserting a gloved, lubricated finger into the rectum to feel for abnormalities in the prostate. Early prostate cancer is difficult to be detected by DRE.
2. Second further step if the physician detects a suspicious area during the first step:
 - The TRUS imaging: this noninvasive and nondestructive technique consists of inserting a probe into the rectum and imaging the prostate in real time. It is commonly used as guidance for the biopsy.
 - The biopsy: it consists of collecting samples of prostate tissue with needles passed through the rectum wall, less commonly, the tip of the penis, or the area of skin (perineum) between the anus and scrotum. It is the only way to make a definite diagnosis of prostate cancer.
 3. Further imaging tests, such as CT, positron emission tomography (PET) or magnetic resonance (MR) imaging (including transrectal magnetic resonance (TRMR) imaging), can be performed in addition to TRUS-guided biopsy to help figure out if the disease has spread outside the prostate [Anastasiadis *et al.* 2006, Hovels *et al.* 2008, Thompson *et al.* 2013, Kitajima *et al.* 2013, de Rooij *et al.* 2015, Vali *et al.* 2015].

1.1.7 Treatments

Once the diagnosis has been established, there are different types of treatment for patients with prostate cancer depending on the disease stage:

- Watchful waiting and active surveillance can be performed for old men without signs/symptoms or with other medical conditions and when cancer was found during a screening test. In these cases, no treatment is given until signs/symptoms appear or change (watchful waiting) or until tests show a cancer growth (active surveillance) [Morash *et al.* 2015].
- Surgery is also a treatment for good health patients when tumor is localized only inside the prostate [Bill-Axelson *et al.* 2011]. Radical prostatectomy can be performed to remove the prostate, the surrounding tissues, and the seminal vesicles. Before removing the prostate, lymph node involvement and thus the relevance of a radical prostatectomy can be assessed by pelvic lymphadenectomy. More rarely, transurethral resection of the prostate is performed to treatment symptoms before other treatments.
- Radiotherapy can be used to treat the prostate itself, the seminal vesicles and the lymph nodes to stop and prevent tumor growth. This technique will be discussed in more details in the following sections.
- High intensity focused ultrasound [Cordeiro *et al.* 2012] and cryotherapy [Shah *et al.* 2014] can also allow to destroy the tumor by heating or freezing the prostate tissue.
- Hormonal therapy may be proposed in order to stop hormone production or their action required for cancer growing. Surgery, drugs or other hormones can be used to reduce the amount of male hormones [Loblaw *et al.* 2007].
- Chemotherapy is another treatment consisting of administrating drugs either in a systemic or a regional way to kill cancer cells or to prevent them from dividing.

1.2 Radiotherapy

1.2.1 Types

Radiotherapy, or radiation therapy, is the use of ionizing radiation to treat (cancerous or benign) tumors, other medical conditions, or pain in palliative cancer patients. In the field of radiation oncology, it is one of the three pillars that allows the control or death of malignant cells, along with surgery and chemotherapy. It consists of using high-energy ionizing radiation to permanently damage the DNA of cancerous tissue leading to cellular death. Depending on the way the dose is delivered, there are three main radiotherapy treatment types:

- external beam radiotherapy (EBRT) is the most common form of radiotherapy. It consists of a transcutaneous irradiation using several shaped beams at different incidence angles in order to maximize the dose to the target and minimize the dose to the surrounding normal critical structures. The radiation beams are produced by particle accelerator, or, more rarely, by cobalt machines.
- Brachytherapy: radiation sources are placed inside or next to the tumor, temporarily or permanently. Damage to surrounding healthy tissues is reduced as the irradiation affects a very localized area.
- Radioisotope therapy is a form of targeted RT. The patient is administered (orally or intravenously) a radiopharmaceutical composed of a radioactive element which emits high-energy particles capable of destroying tissue, and a drug that carries the radioactive element generally via the bloodstream to the site of treatment.

1.2.2 Brief history of radiotherapy

During an experiment on electricity in 1895, the German physicist Wilhelm Roentgen observed by chance the existence of a new kind of rays that he called X-rays (the letter x standing for something unknown), for which he received the first Nobel Prize in Physics in 1901 [Röntgen 1896]. Soon after, the first attempt to use the “Röntgen rays” to treat cancer was conducted by Victor Despeignes, a French physician, in a stomach cancer patient [Despeignes 1896]. At the same time, Henri Becquerel discovered natural radioactivity (1896), followed by Pierre and Marie Curie who isolated the radium (1898), paving the way for the first applications of brachytherapy [Thariat *et al.* 2013]. All three were awarded the Nobel Prize in Physics in 1903 in recognition of their joint researches on the radiation phenomena.

Until the 1950s, the voltage power applied to X-ray tubes to generate X-rays ranged from 50 to 200 kV, which allowed to treat mainly superficial tumors. Indeed low energy X-rays are strongly attenuated in body tissues, and therefore, most of the dose is delivered to superficial tissues.

The discovery of artificial radioactivity in 1934 by Irène and Frédéric Joliot-Curie [Curie & Joliot 1934], for which they won the Nobel Prize in Chemistry in 1935, opened the way for the use of high energy photon radiation in radiotherapy. The early 1950s witnessed the first treatments using the gamma rays from the decay of cobalt-60 (energies of 1.17 and 1.33 MeV). This period also marked the introduction of medical linacs allowing the generation of X-rays of 4 to 25 megavolts (MV), capable of treating deep tumors while minimizing cutaneous toxicities, and electron beams for the treatment of superficial tumors. The use of cobalt-60 as a radiation source in radiotherapy gradually decreased for radiation protection matters. In fact, cobalt therapy has the disadvantage that the radiation source needs to be replaced after 5 years of usage (half-life of the cobalt-60 isotope: 5.3 years), after which its activity remains high. A series of accidents were reported in relation to

disused cobalt-60 radiation sources. Nowadays, the cobalt-60 in radiotherapy centers of industrialized countries is nearly exclusively used for intra-cranial stereotactic radiosurgery (gamma knife). However, recent developments that combine cobalt therapy with real-time magnetic resonance imaging (MRI) guidance have been carried out and may renew interest in cobalt therapy.

Since the 50s, other radiation types such as neutrons, protons, α and carbone ions have been used because of their superior biological efficiency and/or their advantageous depth dose curve (Bragg peak). However, accelerating such heavy particles requires more complex and expensive facilities compared to photons and electrons.

The last major innovations in radiotherapy were due to the increasing power and availability of computers [Dutreix 1972], and the introduction of commercial CT scanners due in large part to the work of Godfrey Hounsfield and McLeod Cormack in the 1970s [Cormack 1994]. This made possible individual radiotherapy through treatment planning, dose calculation, localization of tumors, verification of patient setup, radiation beam data acquisition and computer control of irradiation units which permitted to develop completely new irradiation techniques. One very meaningful inroad made was the introduction of computer-controlled multileaf collimator (MLC) allowing a three-dimensional (3D) dose conformation to the target. This is referred to as 3D conformal radiation therapy (CRT) [Mohan 1995], including advanced modes capable to produce arbitrary complex (concave) intensity distributions such as intensity-modulated radiation therapy (IMRT) [Group 2001], and more recently, IMAT through inverse treatment planning [Yu & Tang 2011]. At the same time, treatment machines are equipped with imaging technology to help increase the precision and accuracy in radiation delivery by correcting the patient's setup (IGRT) [Bucci *et al.* 2005, Ling *et al.* 2006, Verellen *et al.* 2008], and by tracking volumetric deformation, determining its dosimetric implications and adapting the treatment plan for optimal delivery (IGART) [Yan *et al.* 1997].

1.2.3 Definition of volumes

Curative-intent radiotherapy is a localized treatment. That is why a certain number of volumes need to be defined with high precision, prior to treatment planning. The International Commission on Radiation Units and Measurements (ICRU) has the role to establish international standards for radiation units and measurements. Through a series of Reports, it gave recommendations for definitions of different volumes and dose specification points in radiotherapy to promote the use of a common language for constructive and safe exchange of information. ICRU Report 50 [ICRU 1993] supersedes and updates ICRU Report 29 [ICRU 1978]. It defines the following volumes for treatment planning and dose reporting:

- The **gross tumor volume (GTV)** is “the gross palpable or visible/demonstrable extent and location of malignant growth” [ICRU 1993]. It represents what can be seen, palpated or imaged. It is usually based on the combination of imaging modalities (CT, MRI, ultrasound, etc.), diagnostic reports and clinical examination.
- The **CTV** is “the tissue volume that contains a demonstrable GTV and/or sub-clinical microscopic malignant disease, which has to be eliminated. This volume thus has to be treated adequately in order to achieve the aim of therapy, cure or palliation” (ICRU 50). It represents the unknown extent of microscopic tumor. It contains the GTV plus a margin that accounts for invisible suspected invasion of the disease.
- The **planning target volume (PTV)** is “a geometrical concept, and it is defined to select appropriate beam arrangements, taking into consideration the net effect of all possible geometrical variations, in order to ensure that the prescribed dose is actually absorbed in the CTV” [ICRU 1993]. It contains the CTV plus a margin

that accounts for geometrical uncertainties in patient positioning (setup variations), tumor location (organ motion) and machine parameters. This is the volume used in the treatment planning process, in particular, for the selection of appropriate beam sizes and beam arrangements.

Later on, ICRU Report 62 was published as a supplement to ICRU Report 50 which provides additional definitions of volumes [ICRU 1999], as illustrated on Figure 1.5:

- The **internal target volume (ITV)** contains the CTV and an additional margin that compensates for physiological variations in position, shape and size of the CTV due to internal movements (e.g., respiration, variable filling of the bladder and rectum, swallowing, heart beat, movements of the bowel).
- The **organs at risk (OARs)** are the normal tissues that are inside the radiation field and whose sensitivity to radiation is such that the dose received from a treatment plan may be significant compared to their tolerance. They must be considered in the prescription constraints.
- The **planning organ at risk volume (PRV)** contains the OAR and an additional margin to account for variations in the position of the OAR such as movements and setup uncertainties.

The GTV and the CTV are purely oncological concepts. They have an anatomical/physiological basis and have no relation to the irradiation technique used. The ITV, PTV and PRV are geometrical concepts introduced to ensure that the absorbed dose delivered to the CTV and OARs matches the prescription constraints.

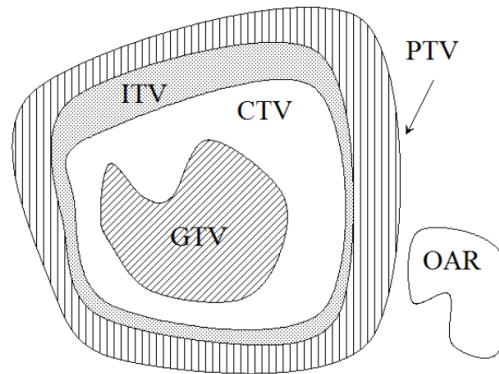


Figure 1.5: Schematic representation of the volumes of interest (VOIs), as defined by the ICRU 50 and 62 reports for use in radiation treatment planning and dose reporting [Podgorsak 2003]

A clinical example of the VOIs is shown for a prostate treatment plan on Figure 1.6. In prostate cancer, the GTV represents the whole prostate gland. The CTV is the same as the GTV, except at the location of the seminal vesicles, tissue adjacent to the prostate, where a GTV-to-CTV margin of 1 cm shall be added. A margin in the range of 5-10 mm around the CTV shall be applied to yield the PTV.

1.2.4 Workflow of radiotherapy

Radiotherapy involves a series of steps as follows:

- **Simulation and contouring**

A volumetric 3D CT scan of the patient anatomy is performed in the treatment position, and possibly with an immobilization device which will help the patient

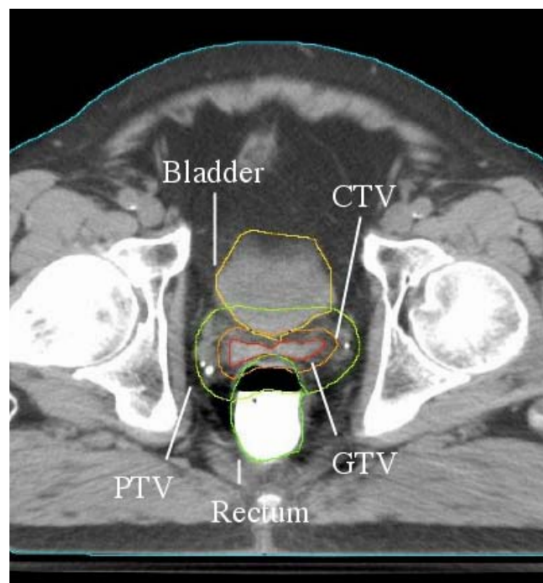


Figure 1.6: Example of the VOIs on a CT for a prostate treatment plan (source: [Podgorsak 2003])

maintain the same position throughout the treatment course and which depends on the tumor location and the degree of accuracy required for the treatment technique. The initial CT scan is often combined with other anatomic and functional images from MRI and PET, with the aim to provide more information on the location and the extent of the tumor. Following the acquisition and registration of the images, the next step, colloquially called organ delineation, contouring or outlining, is the definition of the volumes of the GTV and the OARs on the CT image by the radiation oncologist. Margins are applied between the GTV and the CTV, the CTV and PTV, and possibly the OAR and PRV), respectively.

- **Treatment planning**

This step consists in optimizing the beam arrangement (number of radiation beams, weights, shapes, orientations, energies, use of attenuating wedges,...), to respect the prescription conditions provided by the radiation oncologist (maximum dose in the tumor and minimum damage to healthy tissue). Nowadays treatment planning is fully assisted by computers and can be performed following two different techniques. In forward planning, the optimization process is a manual trial-and-error process which requires the treatment planner (either a medical physicist or a dosimetrist) to modify the beam arrangement until the dose distribution and DVHs calculated by the treatment planning system (TPS) meet the prescription conditions. In inverse planning, the optimization process is automated and an optimization algorithm solves an inverse problem with dose constraints defined by the treatment planner, and finds the treatment plan that best matches all the input criteria. There are different dose prediction models (pencil beam, convolution-superposition, monte-carlo simulation,...) which compute the absorbed dose for a given beam arrangement using the above-mentioned CT scan. The assessment of the adequacy of the predicted dose with respect to the delivered dose is of great importance.

- **Dose delivery**

At each treatment session, the patient is placed in the same position as during the initial CT scan, by aligning the skin marks (or the appropriate immobilization devices) made at the time of the simulation to the room-mounted positioning lasers.

However, the target and the OAR may have moved relative to the skin marks, which justifies the use of in-room imaging techniques to refine the patient's set-up (Section 1.2.3).

The time between the initial CT scan and the beginning of the treatment should be as short as possible in order to reduce tumor growth and anatomical variations as much as possible.

1.2.5 Radiation Fractionation

The amount of radiation dose is measured in gray (Gy). Many factors are considered when a radiation oncologist selects the dose to prescribe: the type and stage of cancer, whether it is for curative, preventive (adjuvant) or palliative purposes, whether chemotherapy is also administered, whether the radiotherapy is administered before or after surgery, the degree of success of surgery, patient comorbidities.

The field of radiation biology has revealed that if the radiation dose delivered to cells is fractionated into small parts with rest periods in between, a smaller amount of cells will die compared to a one-fraction dose. This is because the cells are able to recover between two fractions by means of self-repair mechanisms which repair the damage caused by radiation to DNA. The cell survival rate increases with the number of fractions and the inter-fraction rest time, and decreases with the total dose. Besides, fortunately, normal cells are more efficient in repair than tumor cells. That is why a radiotherapy treatment is spread over several sessions, called fractions, which results in the progressive death of cancer cells while helping normal cells to survive. French radiation oncologist Henri Coutard pioneered fractionated radiotherapy with his still-quoted reference paper [Coutard 1934].

The typical fractionation schedule is 1.8 to 2 Gy per day for adults, five days a week, and 1.5 to 1.8 Gy per day for children. In prostate cancer, 60 to 80 Gy are delivered in fractions of 2 Gy. More rarely, hypofractionated (i.e. with higher dose per fraction) schedules can be used to improve cell killing but such treatments require high accuracy dose delivery and robust patient positioning in order to guarantee healthy tissue sparing [King *et al.* 2013].

1.2.6 Image guidance

1.2.6.1 Image guidance used to reposition the patient (IGRT)

Concomitant advances in computing capabilities, volumetric imagery for simulation, treatment planning algorithms (for beam engineering and dose calculation) and treatment delivery technologies have changed the face of radiotherapy. In this modern context of highly patient-specific, ever more accurate, precise and complex treatment planning and delivery, there is a severe need for accurate and precise patient positioning. That's where IGRT comes in. Daily images acquired prior to treatment serve to guide the patient setup process.

A lot of investigation has been carried out to quantify the geometric uncertainties inherent in the delivery process, with the purpose of defining appropriate treatment CTV-to-PTV margins. When large margins have to be used to account for uncertainties in the target and OAR positions, the benefits of complex treatments such as IMRT or IMAT are limited. As illustrated on Figure 1.7 by the Royal College of Radiologists [Hoskin 2008], image guidance for treatment delivery allows margin reduction. Indeed, applying an on-line, or, to a lesser extent, off-line, imaging protocol for treatment position verification and correction allows to reduce setup errors and therefore justify margin reduction.

IGRT refers to the use of frequent in-room imaging during the treatment course, used to improve the accuracy and precision of the delivery of the planned treatment *. Only rigid

*More broadly, and more rarely too, IGRT refers to the use of a volumetric acquisition of the patient's

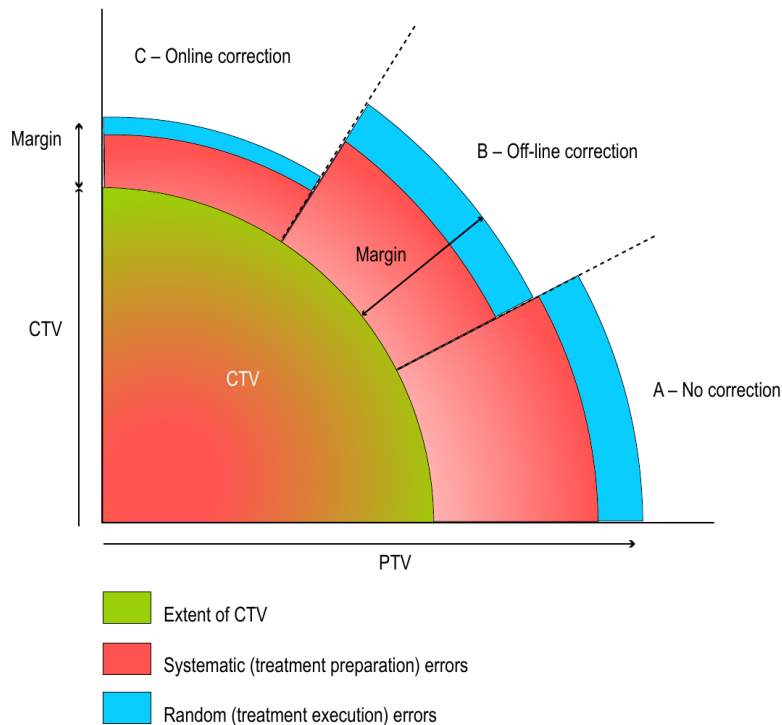


Figure 1.7: Schematic representation of the benefit of applying off-line, and a fortiori on-line, imaging protocols for treatment position verification and correction with respect to systematic and random errors, and hence treatment margin sizes (source: [Hoskin 2008])

displacements of the target, OARs or patient can be corrected by applying the appropriate shifts to the treatment couch. Image guidance does not help correct non-rigid changes.

In-room imaging includes 3D or four-dimensional (4D) conventional CT, CBCT, MV X-ray, optical surface acquisition, and more recently, on a research level, MRI. One of the most widely used imaging techniques for treatment guidance, being also the one under consideration in this thesis, is CBCT. Here is a short description of this imaging modality.

CBCT Historically, in-room MV CT was first proposed by [Swindell *et al.* 1983] for treatment guidance purposes, merely consisting of the addition of a detector array to a linac, and was later extended to MV CBCT by [Mosleh-Shirazi *et al.* 1998].

CBCT has the special feature of using a cone-shaped beam, as opposed to CT where the beam is fan-shaped (Figure 1.8). This cone-beam geometry results in the ability of acquiring tens of tomographic slices for a single CBCT gantry rotation (vs the acquisition of individual consecutive slices with a conventional linac-mounted CT in a helical progression), which offers the potential of radiographic and real-time fluoroscopic imaging valuable when significant intrafraction target motion occurs.

While the mechanical integration of MV CBCT with a linac is elegant and simple (the same MV source is used for both the imaging and the delivery), it faces the problems of:

- poor detection efficiency (and hence poor signal-to-noise ratio) for clinically acceptable doses ($< 10cGy$) due to high radiation transport,
- low spatial resolution of X-ray detectors due to high radiation transport,

anatomy (usually CT) for simulation, which is almost always the case in modern radiotherapy, with the aim of achieving patient-specific planning accuracy.

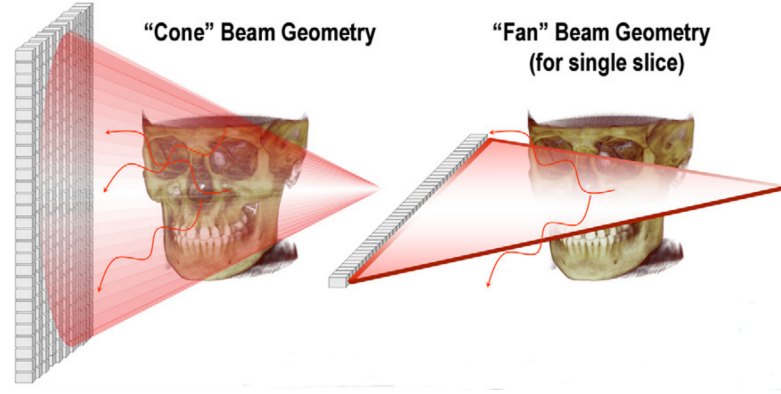


Figure 1.8: Schematic representation of the conventional, fan-beam geometry and the cone-beam geometry (source: [Scarfe & Farman 2008]).

- and poor contrast due to the dominant Compton effect which is nearly independent of the atomic number,

in $\sim 1 - 6$ MV energies [Groh *et al.* 2002]. To address these drawbacks, a kV CBCT system was introduced [Jaffray *et al.* 2002], consisting of a kV source and a flat-panel detector mounted orthogonal to the treatment gantry axis, on the opposite side of the patient relative to the imaging source (Figure 1.9). The rotational axes is parallel to the treatment couch and runs through the target mass center (being also the isocenter of the treatment machine). As the system rotates, planar projections are recorded at different angles. A 3D image of the patient anatomy is reconstructed from all projections.

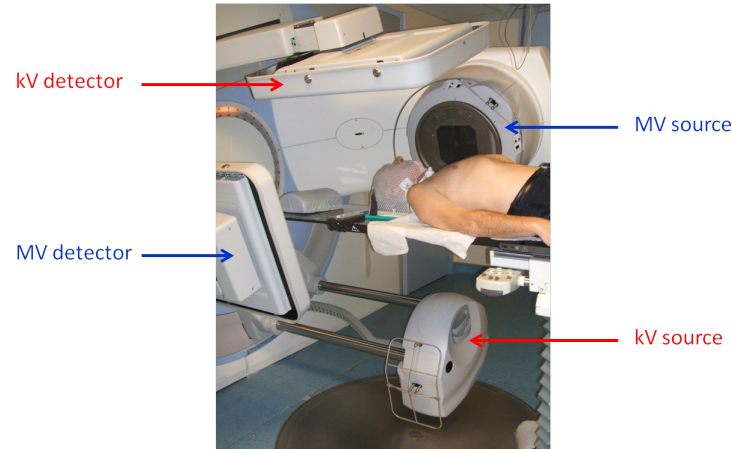


Figure 1.9: Illustration of a linac-mounted kV CBCT system

However, the CBCT image quality remains poor relative to that of CT because of a higher amount of X-ray scatter resulting in contrast reduction and image noise increase [Siewerdsen & Jaffray 2001]. Figure 1.10 illustrates an example of a planning CT scan and a treatment CBCT scan for prostate cancer.

The first commercially available linac-mounted kV CBCT was the Elekta Synergy (Elekta, Crawley, UK). All the CBCT scans used in this work were acquired by this type of imager.

1.2.6.2 Image guidance and adaptive radiotherapy (IGART)

Treatment margins account for geometric uncertainties in the target and OAR positions. Different strategies on margin design have been explored [van Herk 2004]. Except for

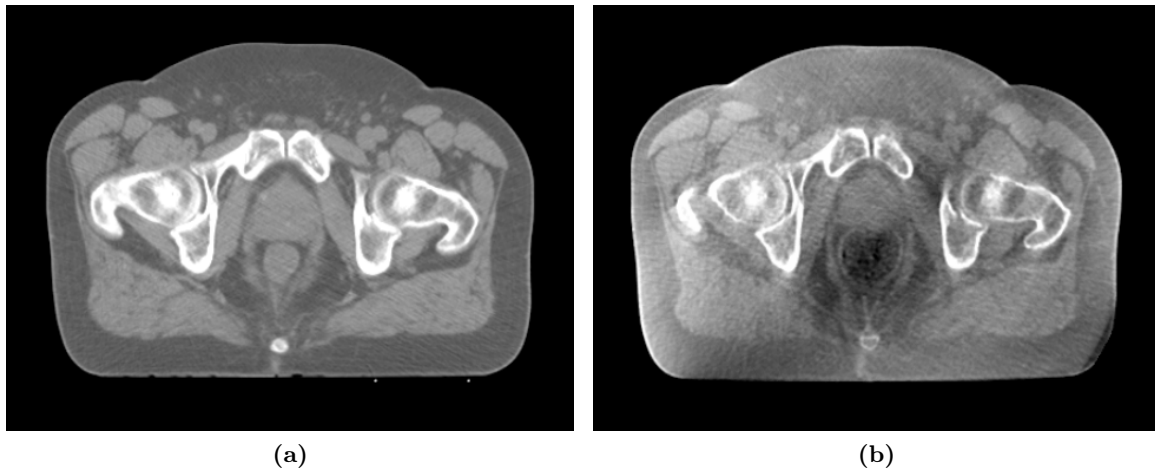


Figure 1.10: Example of (a) a planning CT scan and (b) a treatment CBCT scans for prostate cancer.

breathing motion, these strategies result in predefined uniform or nonuniform margin sizes unique to each radiotherapy center and not customized to the individual patient's variations. This could diminish the benefits of dose escalation, and deteriorate the target coverage and healthy tissue avoidance when large changes in the shape and size of the target and the OAR occur. If so, the initial simulation CT becomes an obsolete, inadequate representation of the patient's anatomy at treatment time, and the initial treatment plan made prior to treatment fails to describe the actual delivered doses, leading to suboptimal treatment. That's where IGART comes in [Ghilezan *et al.* 2010]. A radiation therapy where the treatment plan can be modified/adapted during the treatment course to account for temporal inter-fraction (between treatment fractions) changes in anatomy which cannot be corrected by simple couch shifts (e.g. tumor shrinkage, weight loss, patient's swelling or internal motion) is named IGART. In IGART, image guidance has an essential role not only in correcting rigid changes (by means of couch shifts), but also in pointing out non-rigid inter-fraction changes that can justify replanning. Many investigators have proposed strategies that use the anatomical soft-tissue information from daily imaging to adapt the treatment to the patient's new anatomy. Plan adaptation can be performed at three different timescales:

- Offline between two fractions. The treatment plan is re-optimized when clinically significant variations in the patient's anatomy (tumor shrinkage, weight variation) occur or after few fractions to refine the delivered dose [Qin *et al.* 2015].
- Online immediately prior to a fraction. In this case, the treatment plan is re-optimized just before irradiation using in-room imaging [Wu *et al.* 2004, Court *et al.* 2005, Ahunbay *et al.* 2008]. Another approach consists of selecting the more appropriate treatment plan among pre-optimized ones corresponding to different geometrical scenarios [Qi *et al.* 2014].
- In real time during a fraction by adapting the beam according to the target position (tracking) [Lei *et al.* 2011, Pommer *et al.* 2013] or by interrupting the irradiation when the target moves outside the planned area (gating) [Colvill *et al.* 2014]. Such a strategy enables to compensate for both inter- and intra-fraction motion as opposed to offline and online strategies which only account for inter-fraction motion.

Some refer to dose-guided radiotherapy as an extension of adaptive radiotherapy where the treatment is adapted for future fractions to compensate for dosimetric errors from

past fractions [Chen *et al.* 2006]. Figure 1.11 is a summary of potential adaptive radiation therapy (ART) schemes.

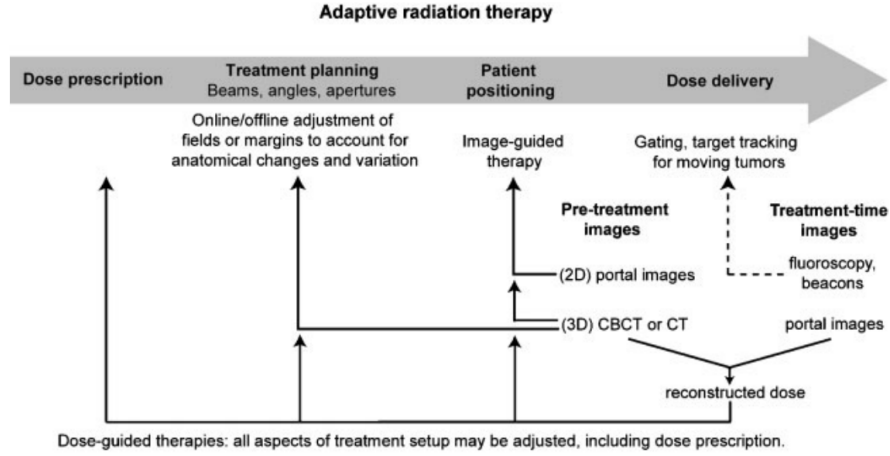


Figure 1.11: A general view of adaptive radiation therapy. The black arrows indicate the possible points of feedback (source: [Chen *et al.* 2006]).

In the case of plan re-optimization, dose calculation can be performed either using directly the CBCT image after some pre-processing [Onozato *et al.* 2014] or a CBCT image acquired from an imaging system calibrated in Hounsfield units [Yang *et al.* 2007, Richter *et al.* 2008]. Another approach to circumvent the limitations relative to CBCT calibration and quality is to deformably register the planning CT image onto the treatment-day CBCT image and perform dose calculation using the mapped CT image. It is to be noted that this method may also be useful when the isocenter is too far from the center of the patient's body (which is not the case in prostate cancer patients) leading to leave some structures out of the CBCT field of view.

1.3 Principles of image registration

Image registration is the process of determining the spatial transform that maps points in one image (defined as the fixed image) to their homologous anatomical points in another image (defined as the moving image). Registration is treated as an optimization problem where the goal is to find, in an iterative way, the spatial transformation that minimizes the differences between the two images to be registered.

The goal of this section is not to provide an exhaustive review on medical image registration methods. For that, the interested reader can refer, among other sources, to [Sotiras *et al.* 2013, Holden 2008, Fischer & Modersitzki 2008, Sarrut 2006, Goshtasby 2005, Crum *et al.* 2004, Zitova & Flusser 2003, Modersitzki 2003, Pluim *et al.* 2003, Dawant 2002, Rueckert 2001, Hill *et al.* 2001, Fitzpatrick *et al.* 2000, Rohr 2000, Lester & Arridge 1999, Maintz & Viergever 1998]. The goal is rather to give the key points of registration, and then an brief overview of the literature on CT-to-CBCT intra-subject registration for prostate cancer applications. For the sake of brevity, only the 3D case is considered in this work.

General registration framework

Basically, two input images, the fixed and the moving, are passed to a registration algorithm which is composed of the following four elements (Figure 1.12):

- the transform is a function that maps point locations of the fixed image to point locations of the moving one;
- the similarity metric provides a measure of how well the transform is mapping the fixed image onto the moving one, i.e. how well the fixed image is matched by the transformed moving image;
- the optimizer seeks to maximize the metric over the search space defined by the parameters of the transform;
- the interpolator is used to evaluate the intensities in the moving image at non-grid positions.

The choice of these elements highly depend on the imaging modalities used and the anatomical region to be registered.

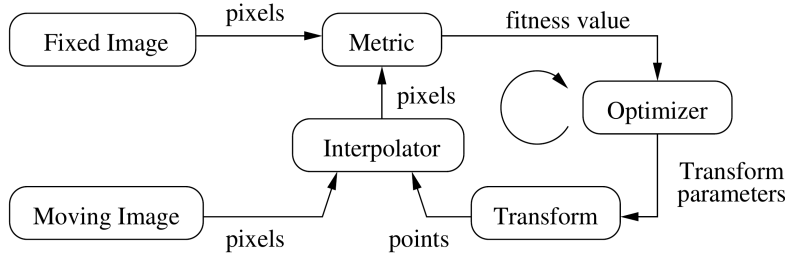


Figure 1.12: The basic components of the registration framework are two input images (fixed and moving), a metric, an optimizer, a transform and an interpolator (source: [Ibanez et al. 2013]).

Notations

Ω_I	Fixed image domain
Ω_J	Moving image domain
$\mathbf{x} = (x, y, z)$	Spatial coordinates of a point in the fixed image
$\mathbf{x}' = (x', y', z')$	Spatial coordinates of a point in the moving image
$I(\mathbf{x})$	Fixed image intensity at point \mathbf{x}
$J(\mathbf{x}')$	Moving image intensity at point \mathbf{x}'
$T(\mathbf{x}) = \mathbf{x}'$	Spatial transform referring to the mapping from the space of the fixed image to the space of the moving image
$\mathbf{u}(\mathbf{x}) = \mathbf{x}' - \mathbf{x}$	Displacement field at point \mathbf{x}
$S(I, J \circ T)$	Similarity function
∇	Gradient of a function: $\nabla f = \frac{\partial f}{\partial x}(x, y, z) \mathbf{e}_1 + \frac{\partial f}{\partial y}(x, y, z) \mathbf{e}_2 + \frac{\partial f}{\partial z}(x, y, z) \mathbf{e}_3$ where the $\{\mathbf{e}_i\}$, $i \in \{1, 2, 3\}$, are the orthogonal unit vectors pointing in the coordinate directions.

It is assumed that the images f and m are smooth and compactly supported functions on rectangular domains $\Omega_I, \Omega_J \in \mathbb{R}^3$. For all mathematical derivations in this work, a continuous formulation is used. The discret aspect of the data is only found at the implementation stage.

Transformation models

The transformation model is represented by a set of parameters (often referred to as degrees of freedom (DOFs)) whose size increases with complexity (from 0 for identity to the number of pixels in the image for a non-parametric transformation model).

The choice of the deformation model is of great importance for the registration outcome as it specifies the search space and limits the range of solution candidates, i.e. the type of transformations that are desirable or acceptable. It depends on the nature of the deformation to recover. Image registration methods can be classified according to the space to which the transformations belong to, that is, depending on the transformation used to model the mapping: rigid and affine registration algorithms optimize only a few parameters (6 and 12, respectively) while DIR algorithms may use a very high dimensional parameter search space. The degree of allowed deformation is always a tradeoff between computational efficiency and richness of description. A low-degree-of-freedom transformation may be unable to describe fully the behavior of organs that move and deform over time, such as the pelvic soft tissue deformation with respect to bones).

Rigid transformation A RR algorithm involves the computation of a rigid transformation which is specified by the combination of a rotation and a translation ([Hill *et al.* 2001, Fitzpatrick *et al.* 2000, Maintz & Viergever 1998]). There are many representations possible for a rotation, including Euler angles, Cayley-Klein parameters, quaternions, axis and angle, and orthogonal matrices. A rigid transformation can be defined as $\mathbf{x}' = \mathbf{R}\mathbf{x} + \mathbf{T}$ where \mathbf{R} is a 3x3 orthogonal matrix, and \mathbf{T} , a vector. Hence, the optimization problem can be formulated as: $\min_{\mathbf{R}, \mathbf{T}} \sum_{x \in I} \|\mathbf{x}' - (\mathbf{R}\mathbf{x} + \mathbf{T})\|$. Distances, straightness of lines and angles are preserved.

Affine transformation Affine transformation can be seen as the extension of rigid transformation. Scaling and shearing are allowed. Straight lines, planes, ratios of distances between points lying on a straight line and parallelism are preserved but not angles or distances. It is defined as $\mathbf{x}' = \mathbf{A}\mathbf{x} + \mathbf{T}$, where there is no orthogonality constraint on matrix \mathbf{A} .

Deformable transformation A DIR algorithm involves the computation of a non-rigid/non-linear, dense transformation, i.e. a spatially varying deformation model. The output is a deformation field (DF), that is, an image of the same size as the fixed image whose elements are vectors that represent the displacement from all fixed image grid positions to their homologous moving image (possibly non-grid) positions.

An extensive review of transformations for image registration can be found in [Holden 2008], which was extended by [Sotiras *et al.* 2013]).

Optimizer

The role of the optimizer is to minimize (or maximize) some energy, E , commonly referred to as the cost function, objective function or functional. Different mathematical frameworks have been considered for the optimization procedure, including variational frameworks, stochastic principles and graph-driven techniques. The goal is to find optimal transformation parameters \mathbf{p} numerically:

$$\hat{\mathbf{p}} = \arg \min_{\mathbf{p}} E(I(\cdot), J(T(\cdot, \mathbf{p})))$$

or

$$\hat{\mathbf{p}} = \arg \max_{\mathbf{p}} E(I(\cdot), J(T(\cdot, \mathbf{p})))$$

To tackle the challenging problem of finding a plausible transformation $T(\mathbf{x}, \mathbf{p})$, desirable properties such as diffeomorphism, topology preservation, inverse consistency or symmetry are often enforced. Also the energy often comprises not only a similarity measure (1.3), but also some regularization terms (1.3) to overcome the ill-posedness of the problem.

Similarity measure

The similarity measure is a global measurement (real value) that indicates how well two images are aligned. It is called by a variety of different names, including similarity criterion, metric, matching criterion, matching term, proximity or distance. There are three approaches which can be combined or not. The distance can be computed between two point sets (feature-based registration), two substructures (surface registration) or volumetric data (dense intensity-based registration). Landmark points, organ contours or other surfaces are defined manually or automatically on the two images. They must represent the same anatomical points or objects. The distance can be a simple Euclidian distance or a more advanced distance when considering lines or surfaces. Intensity-based methods involve statistical calculations between the intensity distributions of the two images. For faster computation, only a few samples of the images can be used without altering results.

The most common intensity-based metrics are presented hereunder.

sum of squared differences (SSD) This is the simplest distance designed for mono-modal registration:

$$SSD = \int_{\Omega_I} (I(\mathbf{x}) - J(T(\mathbf{x})))^2 d\mathbf{x}.$$

The best match between the images is reached for a metric value equal to zero.

sum of absolute differences (SAD)

$$SAD = \int_{\Omega_I} |I(\mathbf{x}) - J(T(\mathbf{x}))| d\mathbf{x}$$

NCC This metric has the special feature of being invariant to multiplicative factors between the two image intensity distributions.

$$NCC = - \frac{\int_{\Omega_I} (I(\mathbf{x}) - \bar{I})(J(T(\mathbf{x})) - \bar{J}) d\mathbf{x}}{\sqrt{\int_{\Omega_I} (I(\mathbf{x}) - \bar{I})^2 d\mathbf{x} \int_{\Omega_I} (J(T(\mathbf{x})) - \bar{J})^2 d\mathbf{x}}}$$

where \bar{I} and \bar{J} denote the average intensity of I and J , respectively. The normalization comes from the division by the square root of the autocorrelation of the images (intensity standard deviations). The -1 factor is simply used to make the metric optimal at its minimum. The optimum is reached for a metric value of -1.

Mutual information This metric originated from information theory, and is well suited for multi-modal registration [Pluim *et al.* 2003]. Mutual information is defined as $I(A, B) = H(A) + H(B) - H(A, B)$ where A, B are two random variables, $H(A)$ and $H(B)$ are the entropies of A ($H(A) = - \int p_A(a) \log p_A(a) da$) and B , respectively, and $H(A, B)$ is the joint entropy of A and B ($H(A, B) = - \int p_{AB}(a, b) \log p_{AB}(a, b) da db$). The two most popular implementations to calculate the marginal and joint probability densities (and therefore entropy values) were proposed by Viola and Wells [Viola & Wells III 1997] and Mattes.

Normalized mutual information $NMI(A, B) = 1 + \frac{I(A, B)}{H(A, B)} = \frac{H(A) + H(B)}{H(A, B)}$

Kullback-Leibler divergence Yet another information-based measure. It is a non-symmetric measure of the difference between two discrete probability distributions A and B : $KL(A, B) = \sum_i p_A(i) \log \frac{p_A(i)}{p_B(i)}$ [Chung *et al.* 2002]. The distributions are obtained from the histograms of the images. It is non-negative and its optimal value is zero (when the two distributions are the same).

Other intensity-based similarity measures include mean reciprocal square differences, mean squares histogram and correlation coefficient histogram.

To calculate the similarity between surfaces embedded in multilabel images, overlap measures such as the target overlap, mean overlap (or Dice coefficient), union overlap (or Jaccard coefficient), volume similarity and false positive/negative errors can be used. A detailed description can be found in [Klein *et al.* 2009].

Regularization

Image registration is an ill-posed problem, which means that it violates at least one of the properties defining a well-posed problem in the sense of Hadamard [Hadamard 1923]:

- a solution exists,
- the solution is unique,
- the solution’s behavior changes continuously with the initial conditions.

This entails ill-conditioning, instability of solution, and a highly non-convex cost function. Usually no closed-form solution exists, and the algorithm can be stuck into a local minimum. To alleviate these issues, additional assumptions or constraints need to be added to the formulation of the problem, such as regularization (smoothness) and penalty terms that discourage undesirable transformations, depending on the anatomical/biomechanical properties of the site. The cost function becomes: $\mathcal{M}(f, m \circ T) + \mathcal{R}(T)$.

1.4 Contributions and organization of the manuscript

The main interest of the thesis was to perform intra-patient image registration between the planning CT image and daily CBCT images in the pelvis with two different but complementary goals:

- (Applicational part) To propose CBCT-based prostate setup correction strategies and (b) to evaluate the impact of rectal distension on them for use in IGRT. In particular, a comparison of different automatic CT-to-CBCT RR methods has been carried out without the use of any external markers or fiducials. Also a novel practical method based on rectal distension has been developed to automatically predict registration failure. This method can easily be applicable in clinical routine to help with the decision of which setup correction strategy to adopt.
- (Methodological part) To tackle the challenging problem of CT-to-CBCT DIR for use in IGART. The ultimate goal of the estimation of a dense deformation field between the planning CT image and the treatment CBCT image is to estimate the dose that would be delivered to the organs on the day of the treatment, and help the radiation oncologist to make a decision on whether adapting the treatment is necessary.

Chapter 2 describes our clinical dataset comprised of 10 gray-value CT images and 115 CBCT images of 10 patients and the corresponding binary images representing the manual contours of the prostate, the rectum and the bladder. In order to harmonize the resolution of the binary images and to automatically estimate the missing contours in slices that were

not delineated (purposely not delineated by the radiation oncologist for sake of time), we implemented an ITK-based algorithm to interpolate the binary images on the basis of the shape-based interpolation method described by Raya and Udupa in [Raya & Udupa 1990] and a couple of additional essential steps in order to be able to apply the latter method. The source code is available at the Insight Journal [Boydev *et al.* 2012] and the dataset is available on request.

Chapter 3 focuses on the development of a CBCT-based prostate setup correction strategy using CT-to-CBCT RR. We established a comparison between different RR algorithms: (a) global RR, (b) bony RR, and (c) bony RR refined by a local RR using the prostate CTV in the CT image expanded with 1-to-20-mm varying margins. A comprehensive statistical analysis of the quantitative and qualitative results was carried out using the whole dataset. We also defined a novel practical method to automatically estimate rectal distension occurred in the vicinity of the prostate between the CT and the CBCT images. Using our measure of rectal distension, we evaluated the impact of rectal distension on the quality of local RR and we provided a way to predict registration failure. On this basis, we devised recommendations for clinical practice for the use of automatic RR for prostate localization on CBCT scans.

Chapter 4 is entirely devoted to the methodological development of a new joint segmentation and deformable registration framework. To deal with the poor contrast in CBCT images likely to misguide registration, we conceived a new metric which included two terms: a global similarity term (the NCC was used, but any other one could be used instead) and a segmentation term based on a localized adaptation of the piecewise-constant region-based model of Chan-Vese using an evolving contour in the CBCT image. Our principal aim was to improve the accuracy of the registration compared with an ordinary NCC metric. Our registration algorithm is fully automatic and takes as inputs (1) the planning CT image, (2) the daily CBCT image and (3) the binary image associated with the CT image and corresponding to the organ of interest that we want to segment in the CBCT image in the course of the registration process. Our source code, that is, a new generic metric component integrated in the registration framework of `elastix`, an ITK-based software for image registration [Klein *et al.* 2010], is available on request in the spirit of reproducible research and open science.

Bibliography

- [Ahunbay *et al.* 2008] Ergun E. Ahunbay, Cheng Peng, Guang-Pei Chen, Sreeram Narayanan, Cedric Yu, Colleen Lawton et X Allen Li. *An on-line replanning scheme for interfractional variations*. Med Phys, vol. 35, no. 8, pages 3607–3615, Aug 2008. (Cité en page 32.)
- [Anastasiadis *et al.* 2006] Aristotelis G. Anastasiadis, Matthias P. Lichy, Udo Nagele, Markus A. Kuczyk, Axel S. Merseburger, Joerg Hennenlotter, Stefan Corvin, Karl-Dietrich Sievert, Claus D. Claussen, Arnulf Stenzl et Heinz-Peter Schlemmer. *MRI-guided biopsy of the prostate increases diagnostic performance in men with elevated or increasing PSA levels after previous negative TRUS biopsies*. Eur Urol, vol. 50, no. 4, pages 738–48; discussion 748–9, Oct 2006. (Cité en page 24.)
- [Bill-Axelson *et al.* 2011] Anna Bill-Axelson, Lars Holmberg, Mirja Ruutu, Hans Garmo, Jennifer R. Stark, Christer Busch, Stig Nordling, Michael Haggman, Swen-Olof Andersson, Stefan Bratell, Anders Spangberg, Juni Palmgren, Gunnar Steineck, Hans-Olov Adami, Jan-Erik Johansson et S. P. C. G-4 Investigators . *Radical prostatectomy versus watchful waiting in early prostate cancer*. N Engl J Med, vol. 364, no. 18, pages 1708–1717, May 2011. (Cité en page 24.)
- [Boydev *et al.* 2012] C. Boydev, D. Pasquier, F. Derraz, L. Peyrodie, A. Taleb-Ahmed et J. Thiran. *Shape-based Interpolation of a Set of 2D Slices*. 10 2012. (Cité en pages 38, 48 et 116.)
- [Breslow *et al.* 1977] N. Breslow, C. W. Chan, G. Dhom, R. A. Drury, L. M. Franks, B. Gellei, Y. S. Lee, S. Lundberg, B. Sparke, N. H. Sternby et H. Tulinius. *Latent carcinoma of prostate at autopsy in seven areas. The International Agency for Research on Cancer, Lyons, France*. Int J Cancer, vol. 20, no. 5, pages 680–688, Nov 1977. (Cité en page 21.)
- [Bucci *et al.* 2005] M Kara Bucci, Alison Bevan et Mack Roach 3rd. *Advances in radiation therapy: conventional to 3D, to IMRT, to 4D, and beyond*. CA Cancer J Clin, vol. 55, no. 2, pages 117–134, 2005. (Cité en page 26.)
- [Chen *et al.* 2006] J. Chen, O. Morin, M. Aubin, M. K. Bucci, C. F. Chuang et J. Pouliot. *Dose-guided radiation therapy with megavoltage cone-beam CT*. Br J Radiol, vol. 79 Spec No 1, pages S87–S98, Sep 2006. (Cité en pages 11 et 33.)
- [Chung *et al.* 2002] Albert CS Chung, William M Wells III, Alexander Norbash et W Eric L Grimson. *Multi-modal image registration by minimising kullback-leibler distance*. In Medical Image Computing and Computer-Assisted Intervention MIC-CAI 2002, pages 525–532. Springer, 2002. (Cité en page 37.)
- [Colvill *et al.* 2014] E. Colvill, P. R. Poulsen, J. T. Booth, R. T. O’Brien, J. A. Ng et P. J. Keall. *DMLC tracking and gating can improve dose coverage for prostate VMAT*. Med Phys, vol. 41, no. 9, page 091705, Sep 2014. (Cité en page 32.)
- [Cordeiro *et al.* 2012] Ernesto R. Cordeiro, Xavier Cathelineau, Stefan Thuroff, Michael Marberger, Sebastien Crouzet et Jean J M C H. de la Rosette. *High-intensity focused ultrasound (HIFU) for definitive treatment of prostate cancer*. BJU Int, vol. 110, no. 9, pages 1228–1242, Nov 2012. (Cité en page 24.)
- [Cormack 1994] Allen M Cormack. *My connection with the Radon transform. 75 Years of Radon Transform*, vol. 4, pages 32–35, 1994. (Cité en page 26.)

- [Court *et al.* 2005] Laurence E. Court, Lei Dong, Andrew K. Lee, Rex Cheung, Mark D. Bonnen, Jennifer O'Daniel, He Wang, Radhe Mohan et Deborah Kuban. *An automatic CT-guided adaptive radiation therapy technique by online modification of multileaf collimator leaf positions for prostate cancer*. Int J Radiat Oncol Biol Phys, vol. 62, no. 1, pages 154–163, May 2005. (Cité en page 32.)
- [Coutard 1934] Henri Coutard. *Principles of x ray therapy of malignant diseases*. The Lancet, vol. 224, no. 5784, pages 1–8, 1934. (Cité en page 29.)
- [Crum *et al.* 2004] W. R. Crum, T. Hartkens et D L G. Hill. *Non-rigid image registration: theory and practice*. Br J Radiol, vol. 77 Spec No 2, pages S140–S153, 2004. (Cité en page 33.)
- [Curie & Joliot 1934] Irène Curie et Frédéric Joliot. *Un nouveau type de radioactivité*. CR Acad Sci Paris, vol. 198, pages 254–256, 1934. (Cité en page 25.)
- [Dawant 2002] B.M. Dawant. *Non-rigid registration of medical images: purpose and methods, a short survey*. In Biomedical Imaging, 2002. Proceedings. 2002 IEEE International Symposium on, pages 465–468, 2002. (Cité en page 33.)
- [de Rooij *et al.* 2015] Maarten de Rooij, Esther H J. Hamoen, J Alfred Witjes, Jelle O. Barentsz et Maroeska M. Rovers. *Accuracy of Magnetic Resonance Imaging for Local Staging of Prostate Cancer: A Diagnostic Meta-analysis*. Eur Urol, Jul 2015. (Cité en page 24.)
- [Despeignes 1896] V Despeignes. *Observation concernant un cas de cancer de l'estomac traité par les rayons Roentgen*. Lyon med, vol. 82, pages 428–430, 1896. (Cité en page 25.)
- [Dutreix 1972] A. Dutreix. *[The computer in radiotherapy]*. Rev Prat, vol. 22, no. 8, pages 1359–60 passim, Mar 1972. (Cité en page 26.)
- [Fischer & Modersitzki 2008] Bernd Fischer et Jan Modersitzki. *Ill-posed medicine and introduction to image registration*. Inverse Problems, vol. 24, no. 3, page 034008, 2008. (Cité en page 33.)
- [Fitzpatrick *et al.* 2000] J Michael Fitzpatrick, Derek LG Hill et Calvin R Maurer Jr. *Image registration*. Handbook of medical imaging, vol. 2, pages 447–513, 2000. (Cité en pages 33 et 35.)
- [Ghilezan *et al.* 2010] Michel Ghilezan, Di Yan et Alvaro Martinez. *Adaptive radiation therapy for prostate cancer*. Semin Radiat Oncol, vol. 20, no. 2, pages 130–137, Apr 2010. (Cité en page 32.)
- [Goshtasby 2005] A Ardeshir Goshtasby. *2-d and 3-d image registration: for medical, remote sensing, and industrial applications*. John Wiley & Sons, 2005. (Cité en page 33.)
- [Groh *et al.* 2002] B. A. Groh, J. H. Siewerdsen, D. G. Drake, J. W. Wong et D. A. Jaffray. *A performance comparison of flat-panel imager-based MV and kV cone-beam CT*. Med Phys, vol. 29, no. 6, pages 967–975, Jun 2002. (Cité en page 31.)
- [Group 2001] Intensity Modulated Radiation Therapy Collaborative Working Group. *Intensity-modulated radiotherapy: current status and issues of interest*. Int J Radiat Oncol Biol Phys, vol. 51, no. 4, pages 880–914, Nov 2001. (Cité en page 26.)

- [Hadamard 1923] Jacques Hadamard. *Lectures on the Cauchy's Problem in Linear Partial Differential Equations*. 1923. (Cit  en page 37.)
- [Hill *et al.* 2001] D. L. Hill, P. G. Batchelor, M. Holden et D. J. Hawkes. *Medical image registration*. Phys Med Biol, vol. 46, no. 3, pages R1–45, Mar 2001. (Cit  en pages 33 et 35.)
- [Holden 2008] M. Holden. *A Review of Geometric Transformations for Nonrigid Body Registration*. vol. 27, no. 1, pages 111–128, 2008. (Cit  en pages 33 et 35.)
- [Hoskin 2008] Peter J Hoskin. On target: ensuring geometric accuracy in radiotherapy. Royal College of Radiologists, 2008. (Cit  en pages 11, 29 et 30.)
- [Hovels *et al.* 2008] A. M. Hovels, R A M. Heesakkers, E. M. Adang, G. J. Jager, S. Strum, Y. L. Hoogeveen, J. L. Severens et J. O. Barentsz. *The diagnostic accuracy of CT and MRI in the staging of pelvic lymph nodes in patients with prostate cancer: a meta-analysis*. Clin Radiol, vol. 63, no. 4, pages 387–395, Apr 2008. (Cit  en page 24.)
- [Hsing & Chokkalingam 2006] Ann W. Hsing et Anand P. Chokkalingam. *Prostate cancer epidemiology*. Front Biosci, vol. 11, pages 1388–1413, 2006. (Cit  en page 21.)
- [Hsing *et al.* 2000] A. W. Hsing, L. Tsao et S. S. Devesa. *International trends and patterns of prostate cancer incidence and mortality*. Int J Cancer, vol. 85, no. 1, pages 60–67, Jan 2000. (Cit  en page 20.)
- [Ibanez *et al.* 2013] Luis Ibanez, Will Schroeder, Lydia Ng, Josh Cates et The Insight Software Consortium. *The ITK Software Guide*. Kitware, Inc. ISBN 1-930934-15-7, third  dition, 2013. (Cit  en pages 11, 34 et 50.)
- [ICRU 1978] ICRU. Dose specification for reporting external beam therapy with photons and electrons. Report 29, International commission on radiation units and measurements, 1978. (Cit  en page 26.)
- [ICRU 1993] ICRU. Prescribing, recording and reporting photon beam therapy. Report 50, International commission on radiation units and measurements, 1993. (Cit  en page 26.)
- [ICRU 1999] ICRU. Prescribing, recording and reporting photon beam therapy (supplement to icru report 50). Report 62, International commission on radiation units and measurements, 1999. (Cit  en page 27.)
- [Jaffray *et al.* 2002] David A. Jaffray, Jeffrey H. Siewerdsen, John W. Wong et Alvaro A. Martinez. *Flat-panel cone-beam computed tomography for image-guided radiation therapy*. Int J Radiat Oncol Biol Phys, vol. 53, no. 5, pages 1337–1349, Aug 2002. (Cit  en pages 31 et 56.)
- [King *et al.* 2013] Christopher R. King, Debra Freeman, Irving Kaplan, Donald Fuller, Giampaolo Bolzicco, Sean Collins, Robert Meier, Jason Wang, Patrick Kupelian, Michael Steinberg et Alan Katz. *Stereotactic body radiotherapy for localized prostate cancer: pooled analysis from a multi-institutional consortium of prospective phase II trials*. Radiother Oncol, vol. 109, no. 2, pages 217–221, Nov 2013. (Cit  en page 29.)
- [Kitajima *et al.* 2013] Kazuhiro Kitajima, Robert C. Murphy et Mark A. Nathan. *Choline PET/CT for imaging prostate cancer: an update*. Ann Nucl Med, vol. 27, no. 7, pages 581–591, Aug 2013. (Cit  en page 24.)

- [Klein *et al.* 2009] Arno Klein, Jesper Andersson, Babak A. Ardekani, John Ashburner, Brian Avants, Ming-Chang Chiang, Gary E. Christensen, D Louis Collins, James Gee, Pierre Hellier, Joo Hyun Song, Mark Jenkinson, Claude Lepage, Daniel Rueckert, Paul Thompson, Tom Vercauteren, Roger P. Woods, J John Mann et Ramin V. Parsey. *Evaluation of 14 nonlinear deformation algorithms applied to human brain MRI registration*. Neuroimage, vol. 46, no. 3, pages 786–802, Jul 2009. (Cité en page 37.)
- [Klein *et al.* 2010] Stefan Klein, Marius Staring, Keelin Murphy, Max A. Viergever et Josien P W. Pluim. *elastix: a toolbox for intensity-based medical image registration*. IEEE Trans Med Imaging, vol. 29, no. 1, pages 196–205, Jan 2010. (Cité en pages 38, 99 et 117.)
- [Klotz & Emberton 2014] Laurence Klotz et Mark Emberton. *Management of low risk prostate cancer-active surveillance and focal therapy*. Nat Rev Clin Oncol, vol. 11, no. 6, pages 324–334, Jun 2014. (Cité en page 20.)
- [Lei *et al.* 2011] Siyuan Lei, Nathaniel Piel, Eric K. Oermann, Viola Chen, Andrew W. Ju, Kedar N. Dahal, Heather N. Hanscom, Joy S. Kim, Xia Yu, Guowei Zhang, Brian T. Collins, Reena Jha, Anatoly Dritschilo, Simeng Suy et Sean P. Collins. *Six-Dimensional Correction of Intra-Fractional Prostate Motion with CyberKnife Stereotactic Body Radiation Therapy*. Front Oncol, vol. 1, page 48, 2011. (Cité en page 32.)
- [Lester & Arridge 1999] Hava Lester et Simon R Arridge. *A survey of hierarchical non-linear medical image registration*. Pattern recognition, vol. 32, no. 1, pages 129–149, 1999. (Cité en page 33.)
- [Ling *et al.* 2006] C Clifton Ling, Ellen Yorke et Zvi Fuks. *From IMRT to IGRT: frontierland or neverland?* Radiother Oncol, vol. 78, no. 2, pages 119–122, Feb 2006. (Cité en page 26.)
- [Loblaw *et al.* 2007] D Andrew Loblaw, Katherine S. Virgo, Robert Nam, Mark R. Somerfield, Edgar Ben-Josef, David S. Mendelson, Richard Middleton, Stewart A. Sharp, Thomas J. Smith, James Talcott, Maryellen Taplin, Nicholas J. Vogelzang, James L Wade 3rd, Charles L. Bennett, Howard I. Scher et American Society of Clinical Oncology. *Initial hormonal management of androgen-sensitive metastatic, recurrent, or progressive prostate cancer: 2006 update of an American Society of Clinical Oncology practice guideline*. J Clin Oncol, vol. 25, no. 12, pages 1596–1605, Apr 2007. (Cité en page 24.)
- [Maintz & Viergever 1998] J. B. Maintz et M. A. Viergever. *A survey of medical image registration*. Med Image Anal, vol. 2, no. 1, pages 1–36, Mar 1998. (Cité en pages 33 et 35.)
- [Modersitzki 2003] Jan Modersitzki. Numerical methods for image registration. Oxford university press, 2003. (Cité en page 33.)
- [Mohan 1995] Mohan. *Field Shaping for Three-Dimensional Conformal Radiation Therapy and Multileaf Collimation*. Semin Radiat Oncol, vol. 5, no. 2, pages 86–99, Apr 1995. (Cité en page 26.)
- [Morash *et al.* 2015] Chris Morash, Roven Tey, Chika Agbassi, Laurence Klotz, Tom McGowan, John Srigley et Andrew Evans. *Active surveillance for the management of localized prostate cancer: Guideline recommendations*. Can Urol Assoc J, vol. 9, no. 5-6, pages 171–178, 2015. (Cité en page 24.)

- [Mosleh-Shirazi *et al.* 1998] M. A. Mosleh-Shirazi, P. M. Evans, W. Swindell, S. Webb et M. Partridge. *A cone-beam megavoltage CT scanner for treatment verification in conformal radiotherapy*. *Radiother Oncol*, vol. 48, no. 3, pages 319–328, Sep 1998. (Cité en page 30.)
- [Onozato *et al.* 2014] Yusuke Onozato, Noriyuki Kadoya, Yukio Fujita, Kazuhiro Arai, Suguru Dobashi, Ken Takeda, Kazuma Kishi, Rei Umezawa, Haruo Matsushita et Keiichi Jingu. *Evaluation of on-board kV cone beam computed tomography-based dose calculation with deformable image registration using Hounsfield unit modifications*. *Int J Radiat Oncol Biol Phys*, vol. 89, no. 2, pages 416–423, Jun 2014. (Cité en page 33.)
- [Pluim *et al.* 2003] Josien P W. Pluim, J B Antoine Maintz et Max A. Viergever. *Mutual-information-based registration of medical images: a survey*. *IEEE Trans Med Imaging*, vol. 22, no. 8, pages 986–1004, Aug 2003. (Cité en pages 33 et 36.)
- [Podgorsak 2003] Ervin B Podgorsak. *Review of radiation oncology physics: a handbook for teachers and students*. Vienna, International Atomic Energy Agency. Educational reports series, 2003. (Cité en pages 11, 27 et 28.)
- [Pommer *et al.* 2013] Tobias Pommer, Marianne Falk, Per R. Poulsen, Paul J. Keall, Ricky T. O’Brien, Peter Meidahl Petersen et Per Munck af Rosenschöld. *Dosimetric benefit of DMLC tracking for conventional and sub-volume boosted prostate intensity-modulated arc radiotherapy*. *Phys Med Biol*, vol. 58, no. 7, pages 2349–2361, Apr 2013. (Cité en page 32.)
- [Qi *et al.* 2014] Peng Qi, Jean Pouliot, Mack Roach 3rd et Ping Xia. *Offline multiple adaptive planning strategy for concurrent irradiation of the prostate and pelvic lymph nodes*. *Med Phys*, vol. 41, no. 2, page 021704, Feb 2014. (Cité en page 32.)
- [Qin *et al.* 2015] An Qin, Ying Sun, Jian Liang et Di Yan. *Evaluation of online/offline image guidance/adaptation approaches for prostate cancer radiation therapy*. *Int J Radiat Oncol Biol Phys*, vol. 91, no. 5, pages 1026–1033, Apr 2015. (Cité en page 32.)
- [Raya & Udupa 1990] S. P. Raya et J. K. Udupa. *Shape-based interpolation of multidimensional objects*. *IEEE Trans Med Imaging*, vol. 9, no. 1, pages 32–42, 1990. (Cité en pages 38, 48, 49 et 116.)
- [Richter *et al.* 2008] Anne Richter, Qiaoqiao Hu, Doreen Steglich, Kurt Baier, Jürgen Wilbert, Matthias Guckenberger et Michael Flentje. *Investigation of the usability of conebeam CT data sets for dose calculation*. *Radiat Oncol*, vol. 3, page 42, 2008. (Cité en page 33.)
- [Rohr 2000] Karl Rohr. *Elastic registration of multimodal medical images: A survey*. *KI*, vol. 14, no. 3, pages 11–17, 2000. (Cité en page 33.)
- [Röntgen 1896] W. C. Röntgen. *ON A NEW KIND OF RAYS*. *Science*, vol. 3, no. 59, pages 227–231, Feb 1896. (Cité en page 25.)
- [Rueckert 2001] D Rueckert. *Non-rigid registration: Techniques and applications*. *Medical Image Registration*, vol. 13, pages 281–302, 2001. (Cité en page 33.)
- [Sarrut 2006] David Sarrut. *Deformable registration for image-guided radiation therapy*. *Z Med Phys*, vol. 16, no. 4, pages 285–297, 2006. (Cité en page 33.)

- [Scarfe & Farman 2008] William C. Scarfe et Allan G. Farman. *What is cone-beam CT and how does it work?* Dent Clin North Am, vol. 52, no. 4, pages 707–30, v, Oct 2008. (Cité en pages 11 et 31.)
- [Shah *et al.* 2014] Taimur Tariq Shah, Hashim Ahmed, Abi Kanthabalan, Benjamin Lau, Maneesh Ghei, Barry Maraj et Mani Arya. *Focal cryotherapy of localized prostate cancer: a systematic review of the literature*. Expert Rev Anticancer Ther, vol. 14, no. 11, pages 1337–1347, Nov 2014. (Cité en page 24.)
- [Siewerdsen & Jaffray 2001] J. H. Siewerdsen et D. A. Jaffray. *Cone-beam computed tomography with a flat-panel imager: magnitude and effects of x-ray scatter*. Med Phys, vol. 28, no. 2, pages 220–231, Feb 2001. (Cité en pages 31 et 56.)
- [Sotiras *et al.* 2013] A. Sotiras, C. Davatzikos et N. Paragios. *Deformable Medical Image Registration: A Survey*. vol. 32, no. 7, pages 1153–1190, 2013. (Cité en pages 33 et 35.)
- [Swindell *et al.* 1983] W. Swindell, R. G. Simpson, J. R. Oleson, C. T. Chen et E. A. Grubbs. *Computed tomography with a linear accelerator with radiotherapy applications*. Med Phys, vol. 10, no. 4, pages 416–420, 1983. (Cité en page 30.)
- [Thariat *et al.* 2013] Juliette Thariat, Jean-Michel Hannoun-Levi, Arthur Sun Myint, Te Vuong et Jean-Pierre Gérard. *Past, present, and future of radiotherapy for the benefit of patients*. Nat Rev Clin Oncol, vol. 10, no. 1, pages 52–60, Jan 2013. (Cité en page 25.)
- [Thompson *et al.* 2013] James Thompson, Nathan Lawrentschuk, Mark Frydenberg, Les Thompson, Phillip Stricker et U. S. A. N. Z. . *The role of magnetic resonance imaging in the diagnosis and management of prostate cancer*. BJU Int, vol. 112 Suppl 2, pages 6–20, Nov 2013. (Cité en page 24.)
- [Vali *et al.* 2015] Reza Vali, Wolfgang Loidl, Christian Pirich, Werner Langesteger et Mohsen Beheshti. *Imaging of prostate cancer with PET/CT using (18)F-Fluorocholine*. Am J Nucl Med Mol Imaging, vol. 5, no. 2, pages 96–108, 2015. (Cité en page 24.)
- [van Herk 2004] Marcel van Herk. *Errors and margins in radiotherapy*. Semin Radiat Oncol, vol. 14, no. 1, pages 52–64, Jan 2004. (Cité en page 31.)
- [Verellen *et al.* 2008] Dirk Verellen, Mark De Ridder et Guy Storme. *A (short) history of image-guided radiotherapy*. Radiother Oncol, vol. 86, no. 1, pages 4–13, Jan 2008. (Cité en page 26.)
- [Viola & Wells III 1997] Paul Viola et William M Wells III. *Alignment by maximization of mutual information*. International journal of computer vision, vol. 24, no. 2, pages 137–154, 1997. (Cité en page 36.)
- [Wu *et al.* 2004] Chuan Wu, Robert Jeraj, Weiguo Lu et Thomas R. Mackie. *Fast treatment plan modification with an over-relaxed Cimmino algorithm*. Med Phys, vol. 31, no. 2, pages 191–200, Feb 2004. (Cité en page 32.)
- [Yan *et al.* 1997] D. Yan, F. Vicini, J. Wong et A. Martinez. *Adaptive radiation therapy*. Phys Med Biol, vol. 42, no. 1, pages 123–132, Jan 1997. (Cité en page 26.)
- [Yang *et al.* 2007] Yong Yang, Eduard Schreibmann, Tianfang Li, Chuang Wang et Lei Xing. *Evaluation of on-board kV cone beam CT (CBCT)-based dose calculation*. Phys Med Biol, vol. 52, no. 3, pages 685–705, Feb 2007. (Cité en pages 33 et 93.)

- [Yu & Tang 2011] Cedric X. Yu et Grace Tang. *Intensity-modulated arc therapy: principles, technologies and clinical implementation*. Phys Med Biol, vol. 56, no. 5, pages R31–R54, Mar 2011. (Cité en page 26.)
- [Zitova & Flusser 2003] Barbara Zitova et Jan Flusser. *Image registration methods: a survey*. Image and vision computing, vol. 21, no. 11, pages 977–1000, 2003. (Cité en page 33.)

Contents

3.1	Background	56
3.2	Methods	57
3.2.1	Data description	57
3.2.2	Registration algorithm	57
3.2.3	Software	59
3.2.4	Validation	59
3.2.4.1	Quantitative validation	60
3.2.4.2	Visual assessment	61
3.2.4.3	Impact of registration errors on DVHs	62
3.2.5	Treatment margin calculations	62
3.3	Results	64
3.3.1	Without applying a replace-gas-by-tissue filter	64
3.3.2	Application of a replace-gas-by-tissue filter to improve registra- tion quality	67
3.4	Discussion	77
3.5	Conclusion	80
	Bibliography	81

2.1 Data description

In total, 115 CBCT scans and 10 CT scans from 10 prostate cancer patients were analyzed. Each one of these patients underwent a single planning CT scan and multiple daily CBCT scans over the course of treatment. All the patients were instructed to follow a dietary protocol in order to have a full bladder and an empty rectum free of air at the time of the planning CT acquisition and during the treatment. The planning CT data were acquired using a General Electrics Light Speed scanner. The treatment system was an ELEKTA Synergy linear accelerator (LINAC) equipped with CBCT imaging (named x-ray volume imaging (XVI)). During the CT (CBCT) acquisition, the peak-voltage, the X-ray tube current and the exposure time were 120 kVp (120 kVp), 300 mA (40 mA or 64 mA) and 1000 ms (40 ms), respectively. Combined with the difference in beam geometry (fan for CT and cone for CBCT), these parameters accounted for the lower image quality obtained with CBCT as compared with CT. The slice thickness was 3 mm and 1 mm for the CT and CBCT scans, respectively. The number of slices ranged from 89 to 132 in each CT scan, and was 168 in each CBCT scan. Each CT (CBCT) slice had 512 x 512 (410 x 410) pixels, with a typical in-plane resolution of 0.98 (1.00) mm.

For clinical requirements, the prostate CTV (without seminal vesicles) and the OAR, i.e., the bladder and the rectum, were manually delineated on each planning CT scan by a radiation oncologist. The CT thickness resolution was 3 mm, and all slices were delineated manually. For the purposes of this thesis, the same radiation oncologist manually delineated the CTV and the OARs on each CBCT scan, following the consensus contouring guidelines provided by the Radiation Therapy Oncology Group at www.rtog.org/LinkClick.aspx?fileticket=054g99vNGps%3d&tabid=354. The bladder was contoured in its entirety. The rectum was contoured from the rectosigmoid junction to the anal verge. This anonymized database (composed of the anonymized gray-value CT and CBCT images with their manual segmentations) is now publicly available. The CBCT thickness resolution was 1 mm, and only one slice in every three was delineated manually. For sake of data harmonization, the manual CT segmentations were upsampled to a final CT thickness resolution of 1 mm and the missing contours were estimated in the 1-mm thick CBCT scans (Table 2.1). To meet this twofold objective needed for any of the processings carried out in this thesis, the shape-based interpolation method described by Raya and Udupa in 1990 for three-dimensional images [Raya & Udupa 1990] was implemented, and two standalone filters using the Insight Toolkit ITK www.itk.org were created. This work is available at the Insight Journal [Boydev *et al.* 2012], and is presented in the following section (Section 2.2).


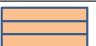





	Manual delineation		After interpolation		Caption
CT	3-mm thickness		1-mm thickness		 Manual contour  Interpolated contour  Missing contour
CBCT	1-mm thickness		1-mm thickness		

Table 2.1: Illustration of the slice thickness and delineation ratio of the CT and CBCT images before and after shape-based interpolation

2.2 Shape-based interpolation of a set of 2D slices

In this thesis, we tackled two issues that often arise after the segmentation of a three-dimensional image:

- Let us first consider that all the slices of the original image are subject to (manual or automatic) segmentation. This results in a set of 2D contiguously delineated slices with the same resolution as that of the original image. Nevertheless, one may want to obtain a segmented image with a higher resolution in the direction orthogonal to the slices, that is, with a thinner slice spacing, as was the case for our manually-delineated 3mm-thick CT data for which a final resolution of 1 mm was intended. Indeed the code that has been implemented allows to interpolate between the delineated slices and obtain new intermediate delineated slices, which originally were nonexistent.
- Suppose instead that to save time the expert that is in charge of the manual segmentation of the 3D image decides to only delineate a few slices, as was the case for our 1mm-thick CBCT data. Our code allows to estimate the contours that have not been drawn.

Using filters from the Insight Toolkit, two standalone filters have been developed based on Raya and Udupa’s shape-based interpolation method for 3D images [Raya & Udupa 1990], where the authors report the superior performance of their method with respect to the classical gray-value interpolation followed by thresholding.

2.2.1 Material and methods

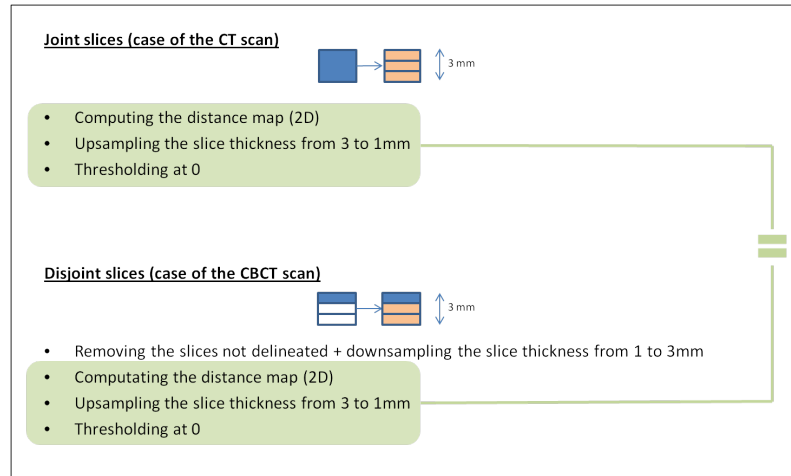


Figure 2.1: The different steps in our shape-based interpolation method.

2.2.1.1 Implementation

The piece of data passed as input is a 3D binary image (e.g. a meta-image with an mhd extension).

In our code, we consider separately the two above-described cases. In the first case (cf. Paragraph A), the input binary image is a set of contiguously delineated slices. The object of interest has been segmented on all possible slices. We aim at interpolating between all slices in the original dataset and coming up with an ensemble of new thinner estimated contours. In the second case (cf. Paragraph B), the input binary image is a set of sparsely

and equally spaced delineated slices (e.g. one slice over two or three delineated). We now aim at ending up with an image wherein the missing contours are estimated.

Let us define n as the ratio of the number of the *delineated* slices in the output image to the number of the *delineated* slices in the input image. The user can specify the value of n using the `SetDelineationRatio()` function.

In both cases, we created a filter which derives from `itk::ImageToImageFilter`. The output image is a 3D binary image, either with a number of slices n times higher (cf. Paragraph A) or of the same size as that of the input (cf. Paragraph B). The input and output image types being always `itk::Image< unsigned char, 3 >`, we considered there was no need for the filters to be templated.

A. Interpolation of a set of contiguously delineated slices There are three steps to be considered. First, a distance transform is applied to the data on a slice-by-slice basis using the `itk::SliceBySliceImageFilter` associated with the internal filter `itk::DanielssonDistanceMapImageFilter`. The `itk::DanielssonDistanceMapImageFilter` is based on the algorithm developed by PE Danielsson [Danielsson 1980]. This results in the creation of a gray-value image wherein the value of each pixel represents the Euclidean distance from that point to the cross-sectional boundary of the object (i.e. within the slice). By convention, points are assigned negative values inside the object, and positive values outside. Secondly, the distance-representing gray-value slices are interpolated using linear or higher-order interpolation to obtain new estimated less spaced gray-value slices (there are n times more slices than in the input). Raya and Udupa report that cubic spline interpolation gives superior results than linear interpolation. In our implementation, we let the user set the kind of interpolation he wants (linear or spline) by means of the `SetInterpolator()` function. Finally, the set of slices is thresholded at zero to produce the interpolated binary dataset.

We call this filter `IntraBinaryShapeBasedInterpolationImageFilter`. As the spacing and the largest possible region of the output are different from that of the input (a change of the meta-information occurs during filtering), it was necessary to override the `ProcessObject::GenerateOutputInformation()` and `ProcessObject::GenerateInputRequestedRegion()`. We refer to [Ibanez *et al.* 2013] for more details on pipeline execution.

B. Interpolation of a set of sparsely and equally spaced delineated slices Here the object of interest is not delineated on every slice. One slice over n is delineated. *The user should be warned that our implementation requires the delineated slices to be regularly spaced.* We first produce an intermediate, subsampled image made of contiguously delineated slices. Indeed only the delineated slices are copied into that intermediate image whose slice spacing is n times bigger than that of the original image. The undelineated slices in the original image are left out. We now can go back to Paragraph A for the methodology. Each slice of that intermediate image is passed to the `DanielssonDistanceMapImageFilter` which calculates the Euclidean distance map with respect to the cross-sectional boundary. The distance map image is then upsampled back to the original sampling rate using linear or higher-order interpolation.

We call this filter `InterBinaryShapeBasedInterpolationImageFilter`. We note that the implementation of this filter differs from the previous one in Paragraph A notably because of the `ProcessObject::GenerateOutputInformation()` and `ProcessObject::GenerateInputRequestedRegion()` that are not overridden here.

2.2.1.2 Usage

The usage of these two filters is similar to other Insight Segmentation and Registration Toolkit (ITK) filters. Their interface is very straightforward. The following snippet of code illustrates the usage of the filter we describe in Paragraph B:

```
typedef unsigned char InputPixelType;
const unsigned int Dimension = 3;

// Declare the input and output types
typedef itk::Image< InputPixelType, Dimension >      InputImageType;
typedef itk::Image< InputPixelType, Dimension >      OutputImageType;

// Declare the filter
typedef itk::InterBinaryShapeBasedInterpolationImageFilter  FilterType;
FilterType::Pointer filter = FilterType::New();

... Read an image and pass it to the filter
filter->SetInput( reader->GetOutput() );

// Setup the default parameters
filter->SetDelineationRatio( 3 );    // n is the ratio of the number of the delineated
                                   // slices in the output to that in the input

... Setup an interpolator
filter->SetInterpolator( interpolator );    // by default, linear interpolator

// Write output
... Setup a writer
writer->SetInput( filter->GetOutput() );
writer->Update();
```

2.2.1.3 Software requirements

This code was developed on a Linux computer with distribution openSUSE 11.4 x86_64. You need to have the following software installed:

- Insight Toolkit 3.20.1
- CMake 2.8.3
- gcc 4.5.1

2.2.2 Results

In this section, we show two use cases of the shape-based interpolation algorithm as described in Paragraph B.

2.2.2.1 Example 1: Interpolation of a cone

We manually drew a right circular cone with aperture 2π using ITK-SNAP (<http://www.itksnap.org>), a free cross-platform open-source software application for manual segmentations [Yushkevich *et al.* 2006]. Given that the image is pixelated, the drawn object is not strictly a cone. The resolution of this image is $1\text{mm} \times 1\text{mm} \times 1\text{mm}$. We then purposely replaced the values of the pixels that belong to every two and three slices by the background value in order to illustrate the case where only one slice over three has been segmented. After that, we run the algorithm of Paragraph B using linear interpolation to estimate the missing contours. Figure 2.2 shows 3D views of each of these images. Figure 2.3 compares the same 2D view of an axis plane in the original cone, the cone before interpolation and the cone after interpolation. Dice's similarity coefficient between the interpolated volume

and the volume initially drawn (original volume) was also calculated. It was found to be 0.94. There were some pixel values that were not the same in the original and interpolated cones, especially on planes outside the axis, but this was due first to the method, and second, to the fact that the cone we tried to manually draw was not perfectly shaped as the image was pixelated.

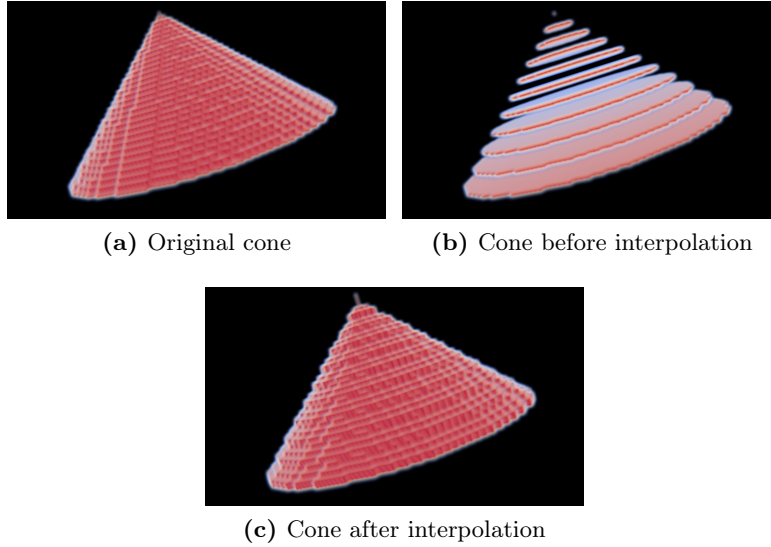


Figure 2.2: 3D views of (a) the cone manually drawn, (b) the same cone but with missing contours, and (c) the interpolated cone. The display software used is ParaView (<http://www.paraview.org/>) [Henderson 2007].

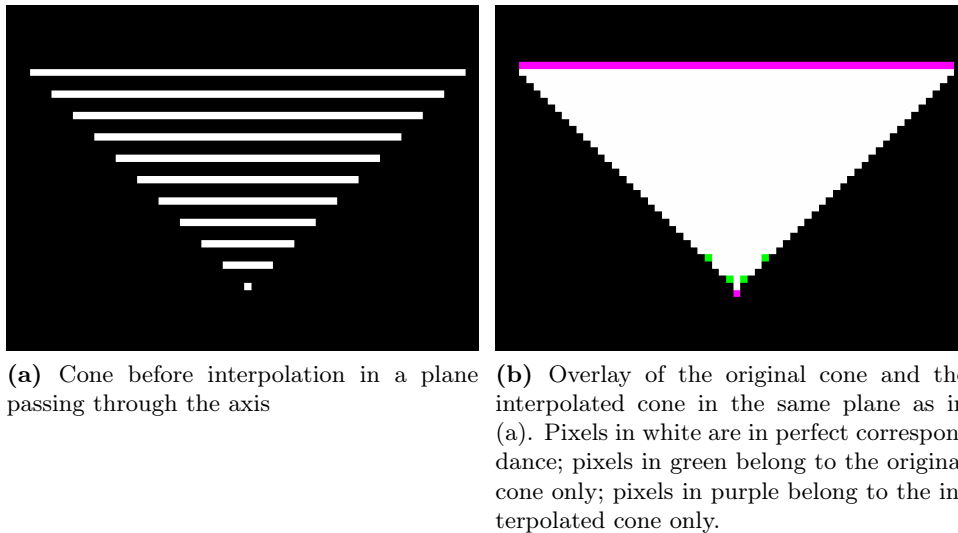


Figure 2.3: (a) 2D central view of the cone before interpolation. (b) Overlay of 2D central views of the original and interpolated cones. The display software used is VV (<http://vv.creatis.insa-lyon.fr/>) [Rit et al. 2011]. The display interpolation is purposely deactivated here.

2.2.2.2 Example 2: Interpolation of a clinical image

Here is a more realistic example, a clinical case. An expert has manually delineated a prostate every slice in a cone-beam computed tomography (CBCT) image. The resolution

of the original dataset is $1\text{mm} \times 1\text{mm} \times 1\text{mm}$. As previously, we purposely replaced the values of the pixels that belong to every two and three slices by the background value in order to illustrate the case where only one slice over three has been delineated. We run the algorithm on the latter binary delineated image using linear interpolation to estimate the missing contours. The result is shown in Figure 2.4. The interpolated contours have been visually validated by the expert after examining the overlay of the binary interpolated image onto the gray-value CBCT image. Dice’s similarity coefficient between the interpolated volume and the volume initially delineated by the expert was also calculated and found to be 0.94.

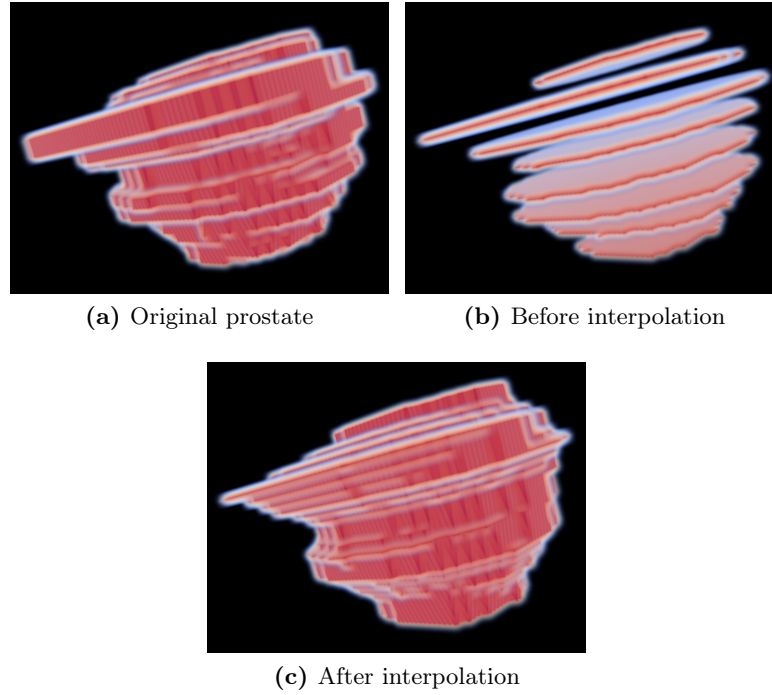


Figure 2.4: Interpolation of a prostate binary image derived from the manual segmentation of a clinical gray-value CBCT image. 3D views of the prostate (a) before interpolation and (b) after interpolation. The display software used is ParaView (<http://www.paraview.org/>) [Henderson 2007].

2.2.3 Conclusion

We implemented two filters that perform a shape-based interpolation of 3D binary images. Two different situations are handled: the image to be interpolated has been delineated on all possible slices and the interpolation process results in an upsampled image with thinner delineated contours, or the image to be interpolated has not been delineated on every slice but the contours are regularly spaced and the missing contours are estimated.

Bibliography

- [Boydev *et al.* 2012] C. Boydev, D. Pasquier, F. Derraz, L. Peyrodie, A. Taleb-Ahmed et J. Thiran. *Shape-based Interpolation of a Set of 2D Slices*. 10 2012. (Cité en pages 38, 48 et 116.)
- [Danielsson 1980] Per-Erik Danielsson. *Euclidean distance mapping*. Computer Graphics and Image Processing, vol. 14, no. 3, pages 227 – 248, 1980. (Cité en page 50.)
- [Henderson 2007] Amy Henderson. *ParaView Guide, A Parallel Visualization Application*. Kitware Inc., 2007. (Cité en pages 11, 12, 52 et 53.)
- [Ibanez *et al.* 2013] Luis Ibanez, Will Schroeder, Lydia Ng, Josh Cates et The Insight Software Consortium. *The ITK Software Guide*. Kitware, Inc. ISBN 1-930934-15-7, third édition, 2013. (Cité en pages 11, 34 et 50.)
- [Raya & Udupa 1990] S. P. Raya et J. K. Udupa. *Shape-based interpolation of multidimensional objects*. IEEE Trans Med Imaging, vol. 9, no. 1, pages 32–42, 1990. (Cité en pages 38, 48, 49 et 116.)
- [Rit *et al.* 2011] S. Rit, R. Pinho, V. Delmon, M. Pech, G Bouilhol, J. Schaerer, B. Navalpakkam, J. Vandemeulebroucke, P. Seroul et D. Sarrut. *VV, a 4D slicer*. In Medical Imaging and Computer-Assisted Intervention MICCAI, Fourth International Workshop on Pulmonary Image Analysis, pages 171–175, 2011. (Cité en pages 12, 52 et 99.)
- [Yushkevich *et al.* 2006] Paul A. Yushkevich, Joseph Piven, Heather Cody Hazlett, Rachel Gimpel Smith, Sean Ho, James C. Gee et Guido Gerig. *User-guided 3D active contour segmentation of anatomical structures: significantly improved efficiency and reliability*. Neuroimage, vol. 31, no. 3, pages 1116–1128, Jul 2006. (Cité en page 51.)

Development of CBCT-based prostate setup correction strategies and impact of rectal distension

Contents

4.1	Background	88
4.2	Methods	92
4.2.1	Description of the proposed model	93
4.2.1.1	Notations and definitions	94
4.2.1.2	Cost function	97
4.2.1.3	Minimization of the cost function	98
4.2.1.4	The transformation model: B-splines	98
4.2.2	Implementation	99
4.2.2.1	Software	99
4.2.2.2	Algorithm	99
4.2.2.3	Parameters	100
4.2.3	Dosimetric considerations	101
4.3	Results	102
4.3.1	Preliminary segmentation study based on local statistics	102
4.3.2	The proposed method	106
4.4	Conclusion	111
	Bibliography	112

3.1 Background

Many studies have demonstrated that dose escalation increases local tumor control with acceptable toxicity [Martin *et al.* 2009, Sveistrup *et al.* 2014]. With intensity-modulated radiotherapy (IMRT), it has become possible to deliver higher doses to the target and reduce the dose to the surrounding normal tissue. However, internal organ motion can occur over the course of radiotherapy and cause an underdosage of the target and an overdosage of the organs at risk (OAR). To compensate for target mobility, population-based margins are added to ensure proper dose coverage of the target [van Herk *et al.* 2000]. This in return may increase toxicity to neighboring normal tissue. Daily image guidance makes it possible to reduce these treatment margins and organ toxicity by helping to provide a precise knowledge of the actual position of the target at treatment [Sveistrup *et al.* 2014, Gill *et al.* 2011]. In the context of prostate cancer radiotherapy, daily image-guidance is particularly useful. Indeed, the prostate gland is known to be a moving and deformable gland, which can be influenced by changes in rectal and bladder volumes [Padhani *et al.* 1999, Roeske *et al.* 1995, de Crevoisier *et al.* 2005]. It should be noted that bladder filling has a substantially smaller influence on prostate motion than rectal distension has [van Herk *et al.* 1995].

There have been many efforts to localize the prostate for accurate delivery before daily treatment, including transabdominal ultrasound imaging [Orton *et al.* 2006], kilovoltage or megavoltage orthogonal port films of implanted gold fiducial markers [Balter *et al.* 1995], portal images of a urethral catheter containing radioopaque markers [Bergström *et al.* 1998] and electromagnetic tracking devices [Langen *et al.* 2008]. More recently, in-room tomography imaging devices have gained attention and have become commonplace in clinical centers. A great number of authors used registration with the planning computed tomography (CT) scan to localize the prostate on the day of the treatment. Most studies were performed using daily in-room CT imaging systems as in [Lattanzi *et al.* 1998, Hua *et al.* 2003, Court & Dong 2003, Paskalev *et al.* 2004, Smitsmans *et al.* 2004]. Cone-beam computed tomography (CBCT) image-guided radiotherapy (IGRT) systems [Jaffray *et al.* 2002] have become widely used tools for prostate positioning in IMRT. However, due to the much poorer image quality of CBCT scans than that of CT scans, prostate localization on CBCT scans is more challenging [Siewerdsen & Jaffray 2001]. Daily in-room CBCT imaging for prostate cancer was used in [Moseley *et al.* 2007, Barney *et al.* 2011, Boda-Heggemann *et al.* 2008, Létourneau *et al.* 2005, Perks *et al.* 2011, Kim *et al.* 2010, Smitsmans *et al.* 2005, Sato *et al.* 2012, Lee *et al.* 2012, Kasibhalta *et al.* 2005, Thilmann *et al.* 2006] but few studies have localized the prostate in a completely automated way.

This chapter aims to evaluate different automatic registration methods for the purpose of prostate position verification and correction using CBCT imaging. It is commonly assumed that the prostate gland behaves as a rigid body [van Herk *et al.* 1995] and that the deformation of the prostate during the course of radiotherapy is small compared to the organ motion [Deurloo *et al.* 2005]. Consequently, during IGRT of prostate cancer, in first order approximation, only set-up error and organ motion need to be corrected, whereas prostate deformation can be considered to be a second-order effect. That is why we focused on rigid registration (RR), which accounts for first-order inter-fraction prostate motion. In this work, we tested different types of CT/CBCT RRs: global, bony, and local soft-tissue RRs.

Unlike previous studies whose quantitative validation consisted of estimating CT/CBCT registration errors at landmark positions (e.g., fiducial markers or calcifications), our study contains a quantitative validation based on Dice calculations which provide a global estimation of the registration accuracy at the location of the target. By definition, the Dice

coefficient quantifies the overlap between regions, and in this work we used it to measure the mismatch between the (manual and automatic CBCT) prostate volumes. We also used an additional measure based on the bidirectional local distance (BLD) to assess the quality of all registration methods. Our quantitative validation is also based on the measurement of the residual setup errors after CBCT-based setup correction using manual contour registration as our golden standard. The measurement of the residual setup errors allowed us to quantify treatment margins.

We also defined a practical method to automatically estimate rectal distension occurred in the vicinity of the prostate between the CT and CBCT scans in order to evaluate the impact of rectal distension on the registration quality and to predict registration failure using only the CT manual contours and the gray-value CT and CBCT images. For this purpose, we based our reasoning on the fact that the variation in the volume of air in the rectum was directly correlated with rectal distension. To the best of our knowledge, no publications to date have presented a simple automatic method to quantify rectal distension occurred between the X-ray CT and CBCT scans using only the manual CT contours and the gray-value CT and CBCT scans. Finally, we devised recommendations for clinical practice for the use of automatic RR for prostate localization on CBCT scans. This chapter, except for the dosimetric evaluation and the treatment margin calculations, has almost completely been presented in [Boydev *et al.* 2015].

In this chapter, we used the terms clinical target volume (CTV) and planning target volume (PTV) as defined by the ICRU [Morgan-Fletcher 2001].

3.2 Methods

3.2.1 Data description

The data used in this chapter is the same data used throughout this thesis. It was described in Chapter 2.

3.2.2 Registration algorithm

To automatically localize the prostate on the 115 daily treatment CBCT scans, each of them was registered to the corresponding planning CT scan using different registration methods described hereunder. The resulting displacements were then applied to the contours drawn manually on the planning CT scans to generate the automatic propagated CBCT contours. The skeleton of our 3D automatic intensity-based registration procedure was previously described in [Boydev *et al.* 2013]. To overcome the problem of the variable amount of fecal gas in the rectum which could mislead registration, we performed an extra pre-processing filtering step which replaced gray values of gas by a tissue-equivalent gray value as recommended in [Smitsmans *et al.* 2004] in addition to our pipeline described in [Boydev *et al.* 2013]. We used a threshold gray value of -150 HU for the CT scans and -500 for the CBCT scans (all gray values below were set to these threshold values). We compared these results with those obtained without filtering. In our study, three types of intensity-based RR methods were tested (Fig. 3.1):

- (a) global RR,
- (b) RR of the pelvic bone structures of the CT and CBCT images (bony RR),
- (c) bony RR followed by a local soft-tissue RR based on target (prostate) information. The latter was conducted using a registration mask that was a region of interest (ROI) defined by the CT CTV expanded with a margin among 1, 3, 5, 8, 10, 12, 15 and 20 mm. The CTV represented the whole prostate gland, which was manually delineated in the (clinical) planning process prior to treatment.

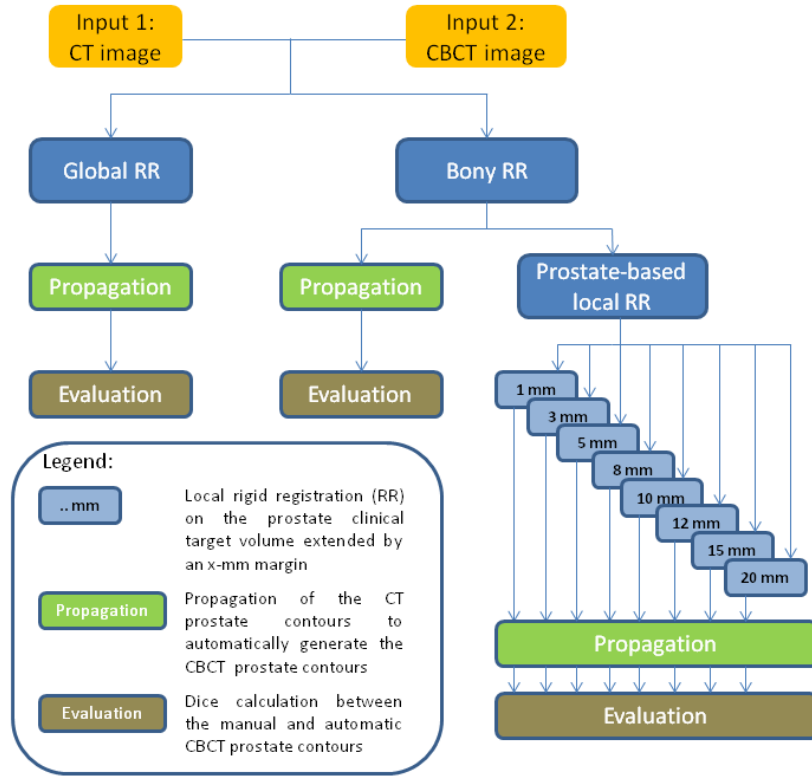


Figure 3.1: Rigid registration pipeline.

In the following, for the sake of simplicity, the combination of a bony RR with a local soft-tissue RR (method (c)) is referred to as a local RR.

A typical image registration framework has four basic components: a similarity metric, an optimizer, a transform and an interpolator. The similarity metric (or metric) measures quantitatively how well a transform is mapping the reference image on top of the target image. We used an intensity-based metric, which allowed the registration to be fully automatic. A simple metric such as mean squared difference could not be used as it required that the images to be registered should have intensity values in the same range, i.e., be monomodal images. In fact, the context was not strictly monomodal image registration since the CBCT system was not calibrated in Hounsfield units. However, the relationship between the intensities on the CT image and those on the CBCT image was given by a linear function. The normalized cross-correlation metric was therefore chosen as a suitable similarity metric (with mean intensities subtracted). This function computed the correlation between the intensity values divided by the square rooted autocorrelation of both the target and reference images. We performed a (deterministic) gradient descent optimization, which was the most straightforward method for incorporating gradient information into the minimization process. The optimizer simply followed the derivative of the metric. At each iteration, the current position was updated according to the gradient of the metric multiplied by a learning factor defined as a step size multiplied by a relaxation factor every time that the gradient changed direction. We used a constant step size of 0.5, a step size relaxation of 0.7, a tolerance on the step size of 0.1, a tolerance on the projected gradient magnitude of $1e-5$ and a maximum number of iterations of 500. Transformations were rigid and hence they had only six degrees of freedom (translations and rotations). Linear interpolation was used in all our experiments. A multi-resolution registration scheme, using three resolution levels, was also utilized. Notice that when masks were associated with the

images to be registered, only pixels that belonged to the intersection of the masks were considered for the computation of the metric.

Prior to CT/CBCT RR, there were some pre-processing steps to carry out (Fig. 3.2):

1. We offset the planning CT image so that its isocenter coincided with the treatment isocenter (i.e., the isocenter of the CBCT system). To do so, the information concerning the planning CT isocenter coordinates was retrieved from the Dicom RTStruct file and compared with the LINAC isocenter coordinates (set to 0,0,0).
2. We created masks that identified the patient's body on both gray-value images. These were the masks associated with the gray-value images by default (if no other masks were used) to allow registration to ignore pixels that were "outside" the patient (e.g., the treatment table or artifacts) and could adversely influence the registration process.
3. (*This step concerned the bony RR only.*) We thresholded the CT and CBCT gray-value images to exclusively show the pelvis bone structure. The threshold level used to extract the bone anatomy was 150 Hounsfield units (HU) for the CT images, and -140 arbitrary units for the CBCT images (in our institution, the CBCT system was not calibrated in HU). These thresholded images were registered, each one associated with its corresponding patient body mask.
4. (*This step concerned the global and the local soft-tissue RRs only.*) We replaced the air in the rectum by a tissue-equivalent gray value in the CT and CBCT images (the registration results were compared with those obtained without this step).
5. (*This step concerned the local soft-tissue RR only.*) We expanded the physician-drawn CT CTV by a margin of 1, 3, 5, 8, 10, 12, 15 or 20 mm. This created the mask to associate with the CT gray-value image in the local soft-tissue RR process, instead of the CT patient body mask created in step 2.

3.2.3 Software

For this study, all the data processing and visualization were performed on a Linux computer with distribution openSUSE 11.4 x86_64, with an Intel Dual Core i5-560M 2.66 GHz processor, 3MB L2 cache, 4 threads, and 8GB RAM. For the implementation of our registration algorithms, the following open-source software, based on C++, was used:

- the Insight Toolkit ITK [Ibanez *et al.* 2005]*,
- the ITK-based Command Line Image Toolkit cltk†.

The software versions used were ITK 4.3.2, CMake 2.8.3 and gcc 4.5.1.

3.2.4 Validation

Software R, version 2.12, was used for all statistical significance testing [Team 2012]. A p-value < 0.05 (< 0.01) was considered (highly) significant. This part is composed of a quantitative section and a qualitative section.

*freely available at www.itk.org

†freely available at www.creatis.insa-lyon.fr/rio/vv

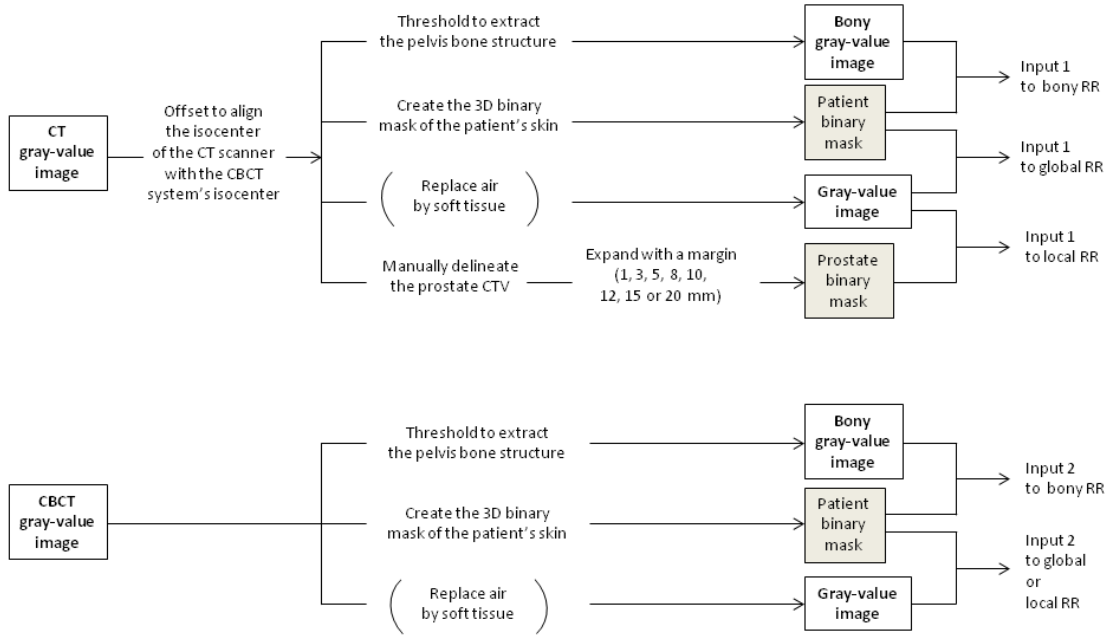


Figure 3.2: Pre-processing pipeline.

3.2.4.1 Quantitative validation

Dice coefficient The Dice similarity coefficient was calculated between the manual (ground-truth) and the automatic (propagated) prostate segmentations on each CBCT scan and for each method. The Dice coefficient between a volume, A, and a volume, B, is defined as follows [Dice 1945]:

$$\text{Dice coefficient} = \frac{2 \cdot (A \cap B)}{A + B} \quad (3.1)$$

Ideally, when two volumes overlap perfectly, the Dice coefficient equals 1. A null Dice coefficient would correspond to two disjoint volumes. Differences in the Dice results across the multiple intensity-based RR methods were tested for significance using the inferential non-parametric Friedman statistical test (with α set to 0.05), a version of the parametric repeated-measures ANOVA. The Wilcoxon-Nemenyi-McDonald-Thompson post-hoc test was conducted to decide which methods were significantly different from each other [Hollander & Wolfe 1999, page 295].

We assumed that the registration was unsuccessful if the Dice coefficient after registration was found to be lower than 95% of the Dice coefficient without registration. Indeed, we decided that below this threshold, the choice of which will be explained in the Results section, performing a registration would deteriorate the initial image alignment (before/without registration). The Dice coefficient without registration was calculated after applying an offset to the planning CT image so that its isocenter coincided with the treatment isocenter (i.e., the isocenter of the CBCT system); this value was calculated between the manual and the automatic prostate segmentations on the CBCT, the automatic one being simply the manual prostate segmentation on the CT scan (no registration was

considered and therefore, no propagation applied).

The Dice coefficient was also calculated between the CT and CBCT manual CTV contours for each CT/CBCT pair after contour RR, i.e., after RR of the binary masks of the manual contours. This Dice value represented an upper bound on the Dice coefficients calculated for the intensity-based RR methods., i.e., the maximum value achievable by any intensity-based RR method.

Bidirectional distance To accurately quantify the difference between the manual (ground-truth/reference) and the automatic (propagated) prostate segmentations on each CBCT scan and for each method, we also used the BLD, a robust point-to-surface distance measure introduced by Kim *et al.* in [Kim *et al.* 2012]. At each point on the reference contour, a BLD was calculated, and then all BLDs over the reference contour were averaged to obtain a global bidirectional distance (BD) between both contours.

Impact of rectal distension on local RR quality In general, the performance of RR deteriorates when the size or the shape of an organ changes. When performing local RR on the prostate ROI (CTV extended with a margin among 1-20mm), the registration mask necessarily includes a portion of the rectum, as the prostate is in contact with the rectum. However, the rectum is highly prone to changes in size and shape due to its ever-changing filling (gaseous and solid contents). The hypothesis we wished to validate was that the unsuccessful local RRs were caused by rectal distension occurred in the vicinity of the prostate. We related the successful and unsuccessful local RRs to the difference in rectum filling between the CT and the CBCT scans in the region of the rectum that was included in the registration mask. For this purpose, for each CT/CBCT pair, we calculated the following variable to quantify rectum filling variation, that is rectal distension:

$$F = |(\bar{I}_{CBCT,r} - \bar{I}_{CBCT,p}) - (\bar{I}_{CT,r} - \bar{I}_{CT,p})| \quad (3.2)$$

Where $\bar{I}_{CT,r}$ is the CT average intensity in the rectum portion, $R_{partial}$, included in the registration mask, $\bar{I}_{CBCT,r}$ is the CBCT average intensity in region $R_{partial}$ after rigidly aligning the bony structures of the CT and CBCT scans, $\bar{I}_{CT,p}$ is the CT average intensity in the prostate, and $\bar{I}_{CBCT,p}$ is the CBCT average intensity in the prostate after rigidly aligning the bony structures of the CT and CBCT scans. We used the manual segmentations to generate region $R_{partial}$, which corresponded to the intersection of the mask and the rectum volume on the CT scan (Fig. 3.3). As the overall range of intensities on a reconstructed CBCT scan could shift across acquisitions, $\bar{I}_{CBCT,p}$ and $\bar{I}_{CT,p}$ were subtracted from $\bar{I}_{CBCT,r}$ and $\bar{I}_{CT,r}$, respectively.

The F number given by Equation 3.2 consistently reflects rectal distension occurred in the vicinity of the prostate. Indeed, in a CT or a CBCT scan, when the rectum is empty (free of air), it is represented by the same range of intensities as the prostate as both the rectum and the prostate are soft tissues. When the same rectum is filled with gas and solid contents, its volume increases and its pixel intensities are shifted to lower values on average.

We plotted the success/failure output from all registrations, arranging the 115 CT/CBCT pairs according to increasing F number.

3.2.4.2 Visual assessment

A blind visual assessment of the quality of the propagated segmentations was conducted to confirm the quantitative results. Each propagated prostate segmentation was displayed onto the corresponding CBCT scan and the radiation oncologist was asked to indicate the number of slices that needed to be corrected, without knowing the registration method

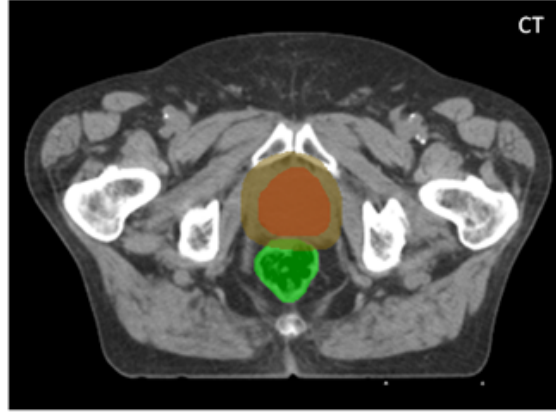


Figure 3.3: Slice of a CT scan. The manual contours of (red) the prostate and (green) the rectum, as well as (brown) the ROI defined as the prostate gland extended with a margin of 8mm. The rectal distension occurred between the CT and the CBCT scans was estimated by calculating the value of F as defined in Equation 3.2. $\bar{I}_{CT,p}$ ($\bar{I}_{CBCT,p}$) was calculated within the red region on the CT (CBCT after bony rigid alignment) scan. $\bar{I}_{CT,r}$ ($\bar{I}_{CBCT,r}$) was calculated within the intersection of the green and the brown regions on the CT (CBCT after bony rigid alignment) scan.

used. A quality score between 0 and 3 was given to each automatic segmentation as follows: 0 if the quality was poor, 1 if a major deviation could be edited (more than 3 slices needed to be corrected), 2 if a minor deviation could be edited (3 slices or less needed to be corrected), 3 if the quality was perfect (no need to edit any slice). Thus, for our set of 115 CBCT scans, the maximum possible cumulative quality score was 345, whereas a score of 230 would indicate a fair mean performance. The non-parametric Wilcoxon signed-rank statistical test was conducted to evaluate the difference between the bony and the local RR methods. The radiation oncologist also assessed whether the propagated segmentations could be used as such for clinical practice, without further correction.

3.2.4.3 Impact of registration errors on DVHs

In this section, we wish to illustrate and compare the dosimetric impact of the studied CBCT-based prostate setup correction strategies by analyzing the DVHs. A DVH is a histogram relating radiation dose to tissue volume. It represents the percentage of volume of an organ (y axis) that receives more than a certain dose (x axis). We computed the DVHs associated with each setup correction strategy following the procedure illustrated by Figure 3.4. The procedure consists of mapping the manual CBCT contours of the prostate, rectum and bladder (“ground truth”) onto the planned dose map by using a given correction strategy. Since in this procedure, we use the manual contours of the prostate, bladder and rectum from the treatment-day CBCT scan, the DVHs we calculate correspond to the dose actually delivered to the organs at the treatment day, not estimated.

3.2.5 Treatment margin calculations

From a clinical perspective, it was of great interest to figure out whether treatment margins for prostate cancer could be reduced using local RR rather than bony RR (Section 1.2.3). For that purpose, the residual setup errors obtained with a daily CBCT-based setup correction strategy using one of our RR methods needed to be measured. For each CT/CBCT pair, we calculated the differences in shifts (translations p_1 , p_2 and p_3 along the LR, SI and AP axes, respectively) and angles (rotations p_4 , p_5 and p_6 around the LR, SI and AP axes, respectively) between gray-value RR and contour RR. We then derived the means $\mu_{p_i,j}$ and standard deviations $\sigma_{p_i,j}$ of these differences for each patient j ($j \in [1, \dots, n]$),

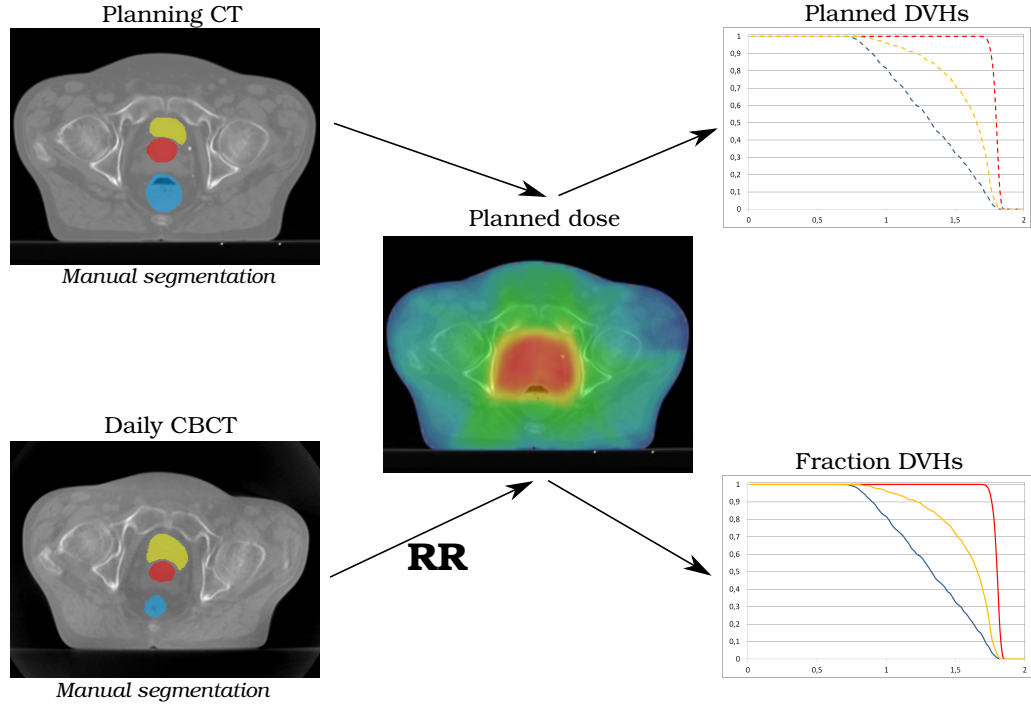


Figure 3.4: The procedure followed to compare the different CBCT-based prostate setup correction strategies and evaluate their dosimetric impact. The DVHs for a given fraction (i.e. using a given treatment-day CBCT) obtained with the different strategies are compared.

$n = 10$ in this chapter) and each translation and rotation parameter p_i (for $i \in [1, \dots, 6]$), allowing to calculate afterwards the systematic $\Sigma_{p_i}^{setup}$ and random $\sigma_{p_i}^{setup}$ setup errors as follows:

$$\Sigma_{p_i}^{setup} = \sqrt{\frac{\sum_{j=1}^n (\mu_{p_i,j} - \mu_{p_i})^2}{n-1}} \quad (3.3)$$

where $\mu_{p_i} = \frac{\sum_{j=1}^n \mu_{p_i,j}}{n}$

$$\sigma_{p_i}^{setup} = \sqrt{\frac{\sum_{j=1}^n (\sigma_{p_i,j})^2}{n}} \quad (3.4)$$

We used Van Herk's treatment margin recipe [van Herk *et al.* 2002] to calculate the required CTV-to-PTV treatment margin on the basis of the residual setup errors obtained if a daily CBCT-based setup correction strategy was applied using one of our RR methods:

$$Margin(CTV \rightarrow PTV) = 2.5\Sigma_{p_i} + 0.7\sigma_{p_i} \quad (3.5)$$

where Σ_{p_i} is the square root of the quadratic sum of SDs of all preparation (systematic) errors, and σ_{p_i} is the square root of the quadratic sum of SDs of all execution (random) errors. The estimation of the other (systematic and random) errors, i.e. those accounting for intra-fraction organ motion and target volume delineation, is beyond the scope of this chapter. We used the numerical values reported in [Rasch *et al.* 1999] for target volume delineation uncertainties on CT scans and [van Herk *et al.* 1995] for intra-fraction organ motion uncertainties to calculate Σ_{p_i} and σ_{p_i} .

3.3 Results

3.3.1 Without applying a replace-gas-by-tissue filter

Dice coefficient We assessed the quality of a registration by comparing the automatic and manual CBCT prostate contours. All manual contours were delineated by the same radiation oncologist. Thus, in the calculation of the Dice coefficient, there was an uncertainty due to the intra-observer and inter-modality variability in manual organ delineation, which we needed to account for in the way we assessed unsuccessful registration. For this purpose, we registered the binary masks of the manual contours of the CT and CBCT images (referred to as contour RR). We found that our set of CT-to-CBCT manual-contour RRs had a Dice mean of $\overline{DSC} = 0.858$ and a SD of 0.035. Approximately 99% of those Dice values lied in interval $[\overline{DSC} - 2.58 * SD, \overline{DSC} + 2.58 * SD]$, being $[0.77, 0.95]$. **In other words, in 99% of cases, the Dice values were smaller than 0.95.** That is why we chose to assess bony, global and local RRs as unsuccessful if the Dice coefficients were lower than 0.95 or 95% of the Dice coefficients obtained without registration.

All intensity-based RR methods, except for the 1-mm local RR ($p = 6.6 \cdot 10^{-2}$), yielded Dice results significantly different from those obtained without registration. In addition, there was a highly significant difference between the following registration methods: 8-mm local RR vs global RR, 8-mm local RR vs bony RR, 8-mm local RR vs 1-mm local RR, 5-mm local RR vs global RR, 5-mm local RR vs bony RR, 5-mm local RR vs 1-mm local RR. Table 3.1 shows the Dice medians, the standard deviations (SD) and the number of failed registrations for each RR method. We obtained the best accuracy with the 5-mm and 8-mm local RRs. The two highest Dice medians, which were obtained with the local RRs with 5-mm and 8-mm margins, were close and equal to 0.816 and 0.815, respectively. The 8-mm local RR appeared to be more robust than the other intensity-based RR methods as it counted the lowest number of failed registrations (6 cases out of 115 failed, i.e., 95 % of success, versus e.g., 90% of success for 5-mm local RR). When the local RR with small margins failed, it could be caused by lack of contrast and/or the frequently observed presence of (moving or not) gas pockets situated in the rectum in the vicinity of the prostate. In the following analysis, we chose to focus on the 8-mm local RR as it produced a median very close to the best one obtained with the 5-mm local RR, the lowest SD and the lowest number of failed registrations. We observed that when failing, the Dice coefficients obtained with the 8-mm local RR or the bony RR were in the same range (between 84% and 95% of the Dice coefficients without registration).

Table 3.1: Dice results after CBCT-based setup correction using RR for 115 CT/CBCT pairs of 10 patients.

	Without RR	Manual-contour RR (reference)	Global RR	Bony RR	Local RR							
					1 mm	3 mm	5 mm	8 mm	10 mm	12 mm	15 mm	20 mm
Dice median	0.731	0.864	0.784	0.785	0.785	0.803	0.816	0.815	0.801	0.801	0.800	0.799
Dice SD	0.105	0.035	0.069	0.070	0.123	0.099	0.061	0.048	0.064	0.067	0.058	0.072
Failed registrations	-	-	7	8	28	21	12	6	11	12	8	9

Figure 3.5 illustrates an example of manual and automatic prostate contours produced by the bony and 8-mm local RRs displayed on top of the corresponding CBCT image. In this particular case, we obtained a Dice coefficient of 0.70 and 0.80 for the bony RR and the 8-mm local RR, respectively.

Bidirectional distance We conducted the statistical analysis for the bidirectional distance in a way similar to that for the Dice coefficients. All intensity-based RR methods yielded results significantly different from those obtained without registration. We observed that the BD-based results confirmed the Dice-based results. Similarly there was a highly significant difference between the following registration methods: 8-mm local RR

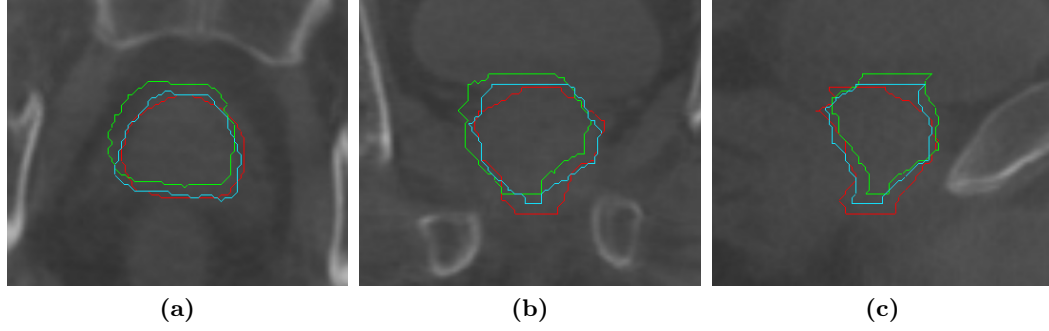


Figure 3.5: Example of manual and automatic prostate contours produced by bony and 8-mm local RRs displayed on top of the corresponding CBCT image in the (a) axial, (b) coronal and (c) sagittal planes.

vs global RR, 8-mm local RR vs bony RR, 8-mm local RR vs 1-mm local RR, 5-mm local RR vs global RR, 5-mm local RR vs bony RR, and 5-mm local RR vs 1-mm local RR. Table 3.2 shows the BD medians and the standard deviations (SD) for each RR method. Overall we obtained the best results with the 5-mm and 8-mm local RRs in terms of BD medians (lowest, equal BD medians). However, the 8-mm local RR had the smallest SD. Thus, these results reinforced the idea that the 8-mm local RR was the most accurate method.

Table 3.2: BD results after CBCT-based setup correction using RR for 115 CT/CBCT pairs of 10 patients.

	Without RR	Manual-contour RR (reference)	Global RR	Bony RR	Local RR							
					1 mm	3 mm	5 mm	8 mm	10 mm	12 mm	15 mm	20 mm
BD* median (mm)	2.86	1.48	2.18	2.17	2.20	1.95	1.84	1.84	2.01	2.01	2.04	2.10
BD* SD (mm)	1.18	0.32	0.70	0.71	1.89	1.28	0.87	0.58	0.75	0.81	0.72	0.84

*BD stands for Bidirectional Distance. It was calculated for each contour comparison by averaging the BLD values over the reference contour.

Impact of rectal distension on local RR quality We investigated in which cases the 8-mm local RR failed. Figure 3.6 illustrates the impact of the variation of rectal filling between the registered images on the 8-mm local RR quality. With our database, the F values obtained ranged from 0.1 to 410.7. We observed that if the F factor as defined in Equation 3.2 was lower than or equal to $F1 = 61.2$, registrations were all successful (93 cases out of 115). All failed registrations (6 in total, representing almost one-third of the 22 remaining cases) appeared to have F values higher than $F2 = 147.6$. We evaluated the performance of the 8-mm local RR with an F cut-off of $(F1 + F2)/2 = 104.4$ (median between $F1$ and $F2$). We found a sensitivity of 1 and a specificity of 0.85 with our dataset.

Figure 3.7 gathers the results for all the RR methods studied, including those of Figure 3.6. Other than the image quality, there are two reasons that can cause the registration to fail regarding the prostate Dice coefficient, both related to rectal distension. The first factor, which we call Factor 1, is the difference in the voxel intensities of the rectum between the CT and the CBCT images. The more different between both images the rectum is, the larger the amount of voxels that do not find any matching. These voxels would misguide the registration. Only bony RR cannot be misguided by Factor 1 as only voxels corresponding to bones are considered in the calculation of the metric. Local RR methods with smaller margins are less influenced by Factor 1 than those with larger margins. The second factor, which we call Factor 2 and which equally influences the quality of all RR methods, is the difference in the size of the rectum between the CT and the CBCT images. In fact, a changing rectum volume will result in deforming the prostate and the registration would fail in case of large deformations. In Figure 3.7, we can actually see that the bony RR is less correlated to rectal distension than any local RR with a margin larger than 3 mm as bony RR is only influenced by Factor 2 while local RR, by both Factors 1 and 2

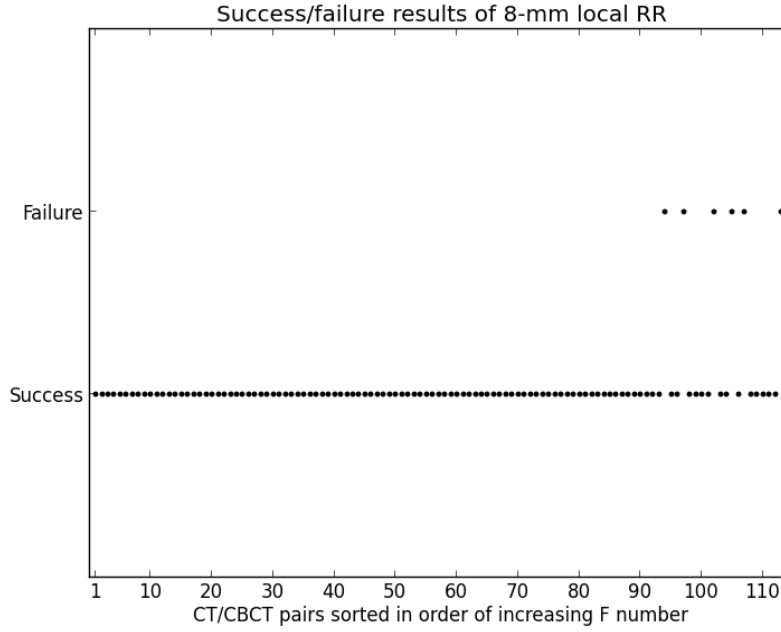


Figure 3.6: Success/failure results. Outcome (success or failure) of 8-mm local RR w.r.t. the CT/CBCT pairs sorted in order of increasing F number (as defined in Equation 3.2).

(without applying a replace-gas-by-tissue filter).

Visual assessment Regardless of the rectum influence, the visual assessment of the segmentation quality confirmed the superiority of the 8-mm local RR over the bony RR. In total, the bony RR achieved a total cumulative score (sum of scores over all registrations) of 258 versus 291 for the 8-mm local RR. This difference was highly significant ($p = 7.2 \cdot 10^{-6}$). For both methods, no segmentations achieved a zero score (poor quality). The 8-mm local RR method always achieved a score better than or equal to that of the bony RR method, except for four cases (out of 115). However, in these four cases, both methods yielded segmentations acceptable for clinical use, without further correction. Table 3.3 indicates the numbers of segmentations that were produced by the bony and 8-mm local RRs for each score and that were considered acceptable for clinical use.

Table 3.3: Qualitative results after CBCT-based setup correction using RR for 115 CT/CBCT pairs of 10 patients.

Score (per segmentation)	0	1	2	3	Acceptable for clinical use
# bony RRs	0	15	57	43	107
# local 8-mm RRs	0	4	46	65	115

Impact of registration errors on DVHs In this section, we wish to illustrate and compare the dosimetric impact of each CBCT-based prostate setup correction strategy. For sake of simplicity, we propose to show the DVHs of the CTV (prostate) and the OARs (rectum and bladder) for only two patients (out of 10), who we call Patient A and Patient B, as the results were similar for all patients. The two patients underwent a 2-course IMAT treatment. Table 3.4 shows the number of fractions and the dose delivered in each course of the IMAT. The first course treated the prostate, the lymph nodes and the seminal vesicles, and the second one treated the prostate only (see Figure 3.8 for Patient A).

Table 3.4: Number of fractions and dose delivered in each course of the IMAT undergone by Patients A and B. The treatment is split into two courses. The first one treats the prostate, the lymph nodes and the seminal vesicles. The second one treats the prostate only.

	1st course		2nd course	
	# fractions	Delivered dose	# fractions	Delivered dose
Patient A	25	45 Gy	15	25.5 Gy
Patient B	23	46 Gy	14	28 Gy

For each patient, we computed the DVHs for two fractions, the first and the last ones of the treatment. Since only rigid registration is considered in this chapter, no cumulative DVHs are computed. In fact, in order to cumulate the dose, over fractions, in deformable organs such as the bladder and the rectum, deformation registration is necessary. Figures 3.9 and 3.10 illustrate the DVHs regarding the first and second IMAT courses of Patient A, respectively, and Figure 3.11 illustrates the DVHs for the first IMAT course of Patient B.

Let us first analyze the DVHs of the CTV. On Figure 3.9, we observe that all setup correction strategies seem acceptable except for the 20-mm local RR. Besides, the bony RR and the other local strategies with margins smaller than or equal to 8 mm seem to produce similar and acceptable prostate dose coverage. Regarding the 2nd course of Patient A (Figure 3.10), all strategies produce equivalent results on the CTV. This may be linked to the fact that the Dice coefficients between the manual and automatic CBCT contours obtained with the different strategies are very close to each other, and hence the automatic contours are similar to each other. For Patient B (Figure 3.11), we observe that local strategies with margins smaller than or equal to 8 mm produce sharp, similar DVHs and a prostate dose coverage better than that obtained with bony RR.

Regarding the OARs, no single strategy outperforms the others. For example, for the first IMAT course of Patient A (Figure 3.9), the bony RR is the worst strategy to spare the rectum but the best one to spare the bladder. For the second IMAT course of Patient A (Figure 3.10), the 8-mm local RR spares the bladder in the best way but not the rectum. For the first IMAT course of Patient B (Figure 3.11), the bony RR, as well as the 8-mm local RR, seem to be the best compromise between sparing the rectum and sparing the bladder. No clear conclusion can be drawn regarding the avoidance of the OARs using one strategy or another. **Indeed, let us recall that all our strategies are based on rigid registration, and hence**

Treatment margin calculations Table 3.5 lists the geometrical uncertainties occurring during both the preparation and execution stages of treatment. These values allowed us to calculate the required CTV-to-PTV treatment margins for prostate cancer using our proposed daily CBCT-based setup correction strategies. We only show translational errors as we assume that rotational errors can be neglected given the round shape of the prostate. We observed that (systematic and random) errors in each translation direction were smaller with 8-mm local RR compared to bony RR. Hence the treatment margin associated to each translation direction can be reduced if 8-mm local RR is used to correct for patient and target inter-fraction (rigid) motion.

3.3.2 Application of a replace-gas-by-tissue filter to improve registration quality

To deal with registration failures, we applied a filter to the CT and CBCT scans prior to registration to replace the intensities of the gas voxels with an intensity of tissue.

	Treatment execution (random) errors (mm)			Treatment execution (systematic) errors (mm)		
	LR	SI	AP	LR	SI	AP
Target volume delineation [38]				1.7	2- 3.5*	2.0
Organ motion [6]	0.9	1.7	2.7	0.9	1.7	2.7
Setup error using bony RR	0.9	1.8	2.1	1.7	2.3	2.4
Setup error using 8-mm local RR	0.5	1.5	1.3	0.5	2.2	1.2
Total SD using bony RR	1.3	2.5	3.4	2.6	3.5- 4.5	4.1
Total SD using 8-mm local RR	1.0	2.3	3.0	2.0	3.4- 4.5	3.6

*These values are due to the larger uncertainty in target volume delineation near the apex and the seminal vesicles.

Table 3.5: Geometrical uncertainties (standard deviations of translations only) involved in prostate cancer treatment using CBCT daily image guidance.

Dice coefficient Table 3.6 shows that applying a replace-gas-by-tissue filter improved the success rate for the global RR and the local RR with a margin higher than or equal to 8 mm. For the 8-mm local RR, the success rate improved from 95% (6 failures out of 115 scan pairs) without filtering to 97% (3 failures remaining out of 115 scan pairs) when a replace-gas-by-tissue filter was applied. Out of the three pairs of scans that failed to be registered with the 8-mm local RR when a replace-gas-by-tissue filter was applied, two were successfully registered using the bony RR, and one was not successfully registered using the bony RR. For margins higher than or equal to 12 mm, the success rate improved from 90%-93% without filtering to 99% (only one failure occurred and corresponded to a pair of scans that were successfully registered with the bony RR) when filtering. In terms of success rate, when filtering, the most robust RRs were the local ones with margins higher than or equal to 12 mm. The 8-mm local RR had the highest Dice median and the lowest SD (best accuracy). Statistically, the local RRs with margins higher than 5 mm did not produce results significantly different from each other; they statistically differed from the bony RR, the global RR, and the 1-mm and 3-mm local RRs (except for the 20-mm local RR vs the global RR).

Table 3.6: Dice results after CBCT-based setup correction using RR for 115 CT/CBCT pairs of 10 patients. Before registration, air was replaced by soft tissue in images.

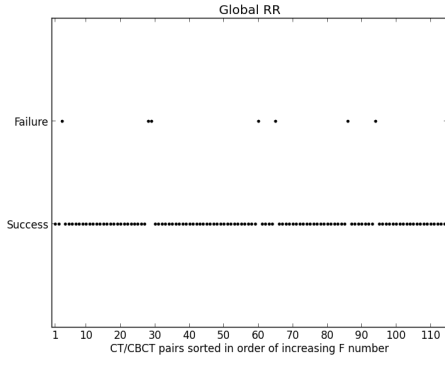
	Without RR	Manual-contour RR (reference)	Global RR	Bony RR	Local RR							
					1 mm	3 mm	5 mm	8 mm	10 mm	12 mm	15 mm	20 mm
Dice median	0.731	0.864	0.797	0.785	0.776	0.794	0.810	0.814	0.813	0.811	0.806	0.811
Dice SD	0.105	0.035	0.062	0.070	0.113	0.123	0.074	0.045	0.052	0.046	0.052	0.055
Failed registrations	-	-	6	8	28	26	20	3	3	1	1	1

Bidirectional distance Table 3.7 shows that for the global RR and the local RRs with margins higher than or equal to 10 mm, applying a replace-gas-by-tissue filter reduced the discrepancy between the manual and automatic contours overall (BD values lower than those obtained without filtering). Among all intensity-based RR methods, the lowest BD medians were obtained with the 5-mm, 8-mm and 10-mm local RRs. The SD of the 8-mm local RR was more than twice as low as that of the 5-mm local RR, and smaller than that of the 10-mm local RR. Therefore, in terms of BD values, the 8-mm local RR yielded more accurate results than did the other intensity-based methods.

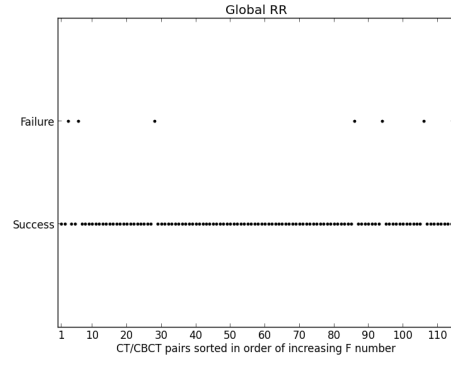
Table 3.7: *BD results after CBCT-based setup correction using RR for 115 CT/CBCT pairs of 10 patients. Before registration, air was replaced by soft tissue in images.*

	Without RR	Manual-contour RR (reference)	Global RR	Bony RR	Local RR							
					1 mm	3 mm	5 mm	8 mm	10 mm	12 mm	15 mm	20 mm
BD* median (mm)	2.86	1.48	2.09	2.17	2.23	2.24	1.89	1.91	1.89	1.97	2.00	1.95
BD* SD (mm)	1.18	0.32	0.64	0.71	1.90	1.69	1.08	0.49	0.59	0.55	0.61	0.66

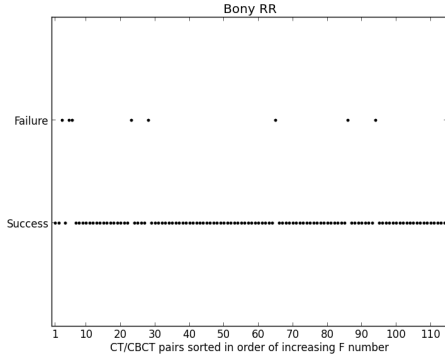
*BD stands for Bidirectional Distance. It was calculated for each contour comparison by averaging the BLD values over the reference contour.



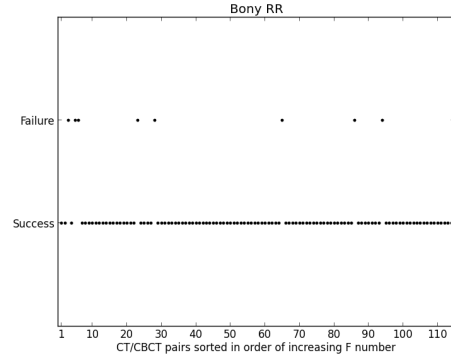
(a) Without filtering the air



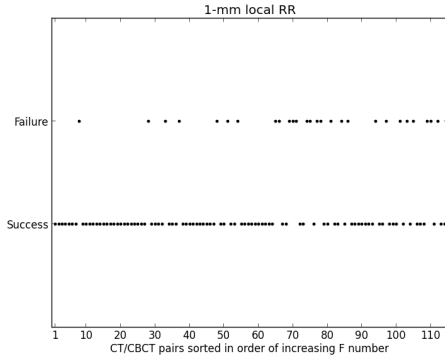
(b) By filtering the air



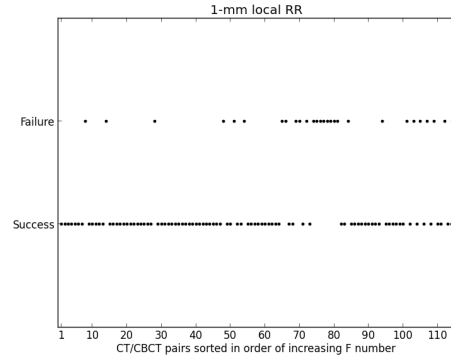
(c) Without filtering the air



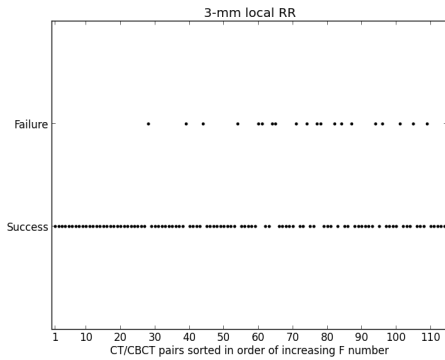
(d) By filtering the air



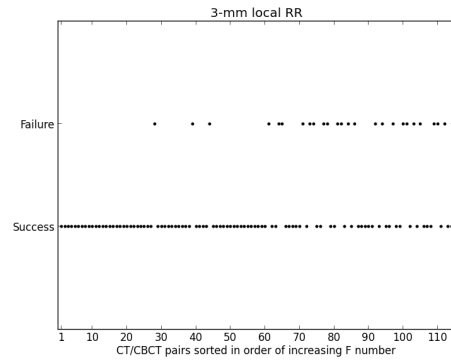
(e) Without filtering the air



(f) By filtering the air



(g) Without filtering the air



(h) By filtering the air

Figure 3.7: Success/failure results for all the RR methods w.r.t. the CT/CBCT pairs sorted in order of increasing F number (as defined in Equation 3.2) with or without the application of a replace-gas-by-tissue filter.

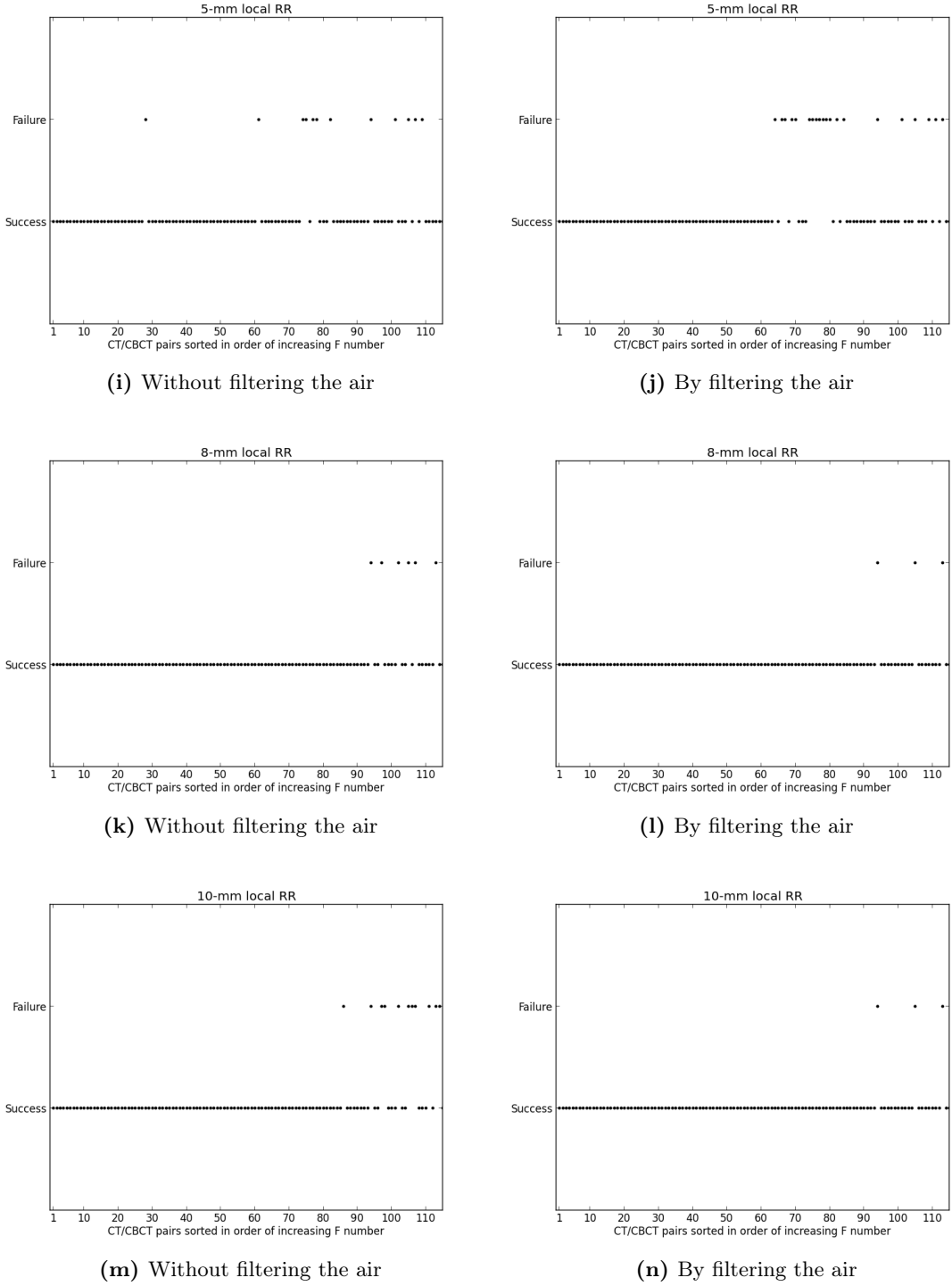
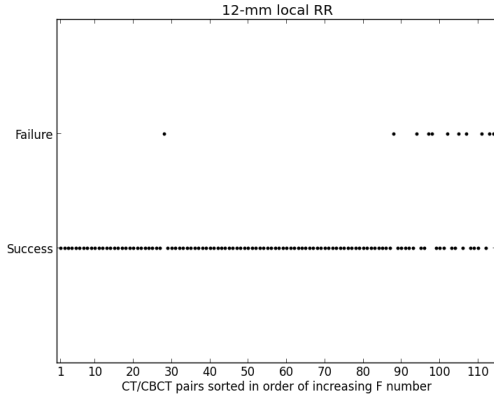
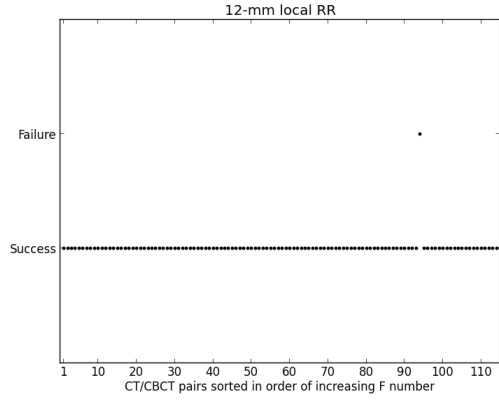


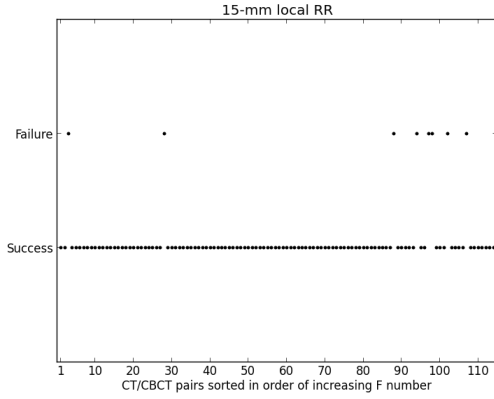
Figure 3.7: Success/failure results for all the RR methods w.r.t. the CT/CBCT pairs sorted in order of increasing F number (as defined in Equation 3.2) with or without the application of a replace-gas-by-tissue filter.



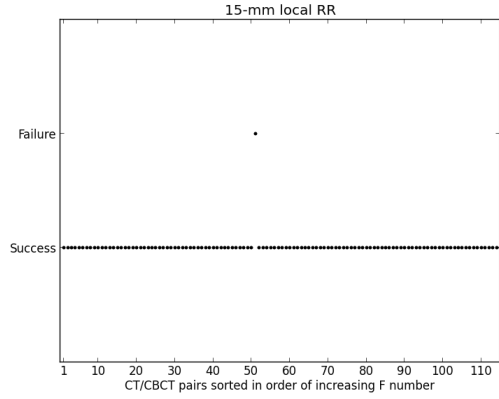
(o) Without filtering the air



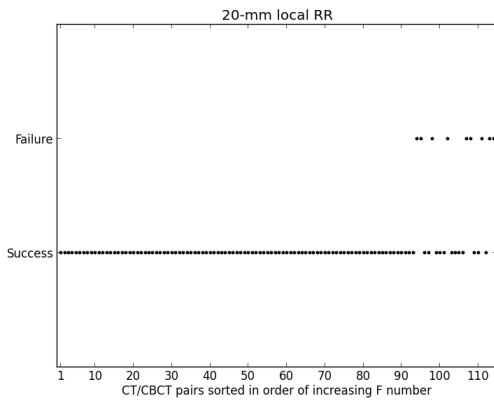
(p) By filtering the air



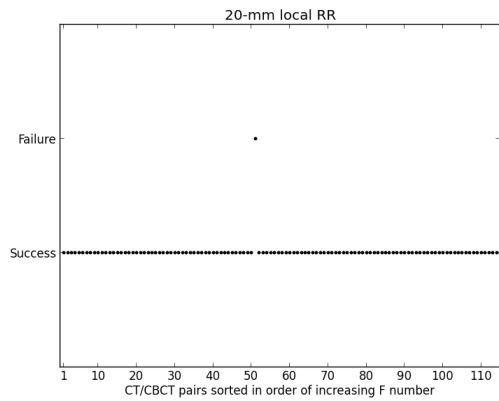
(q) Without filtering the air



(r) By filtering the air



(s) Without filtering the air



(t) By filtering the air

Figure 3.7: Success/failure results for all the RR methods w.r.t. the CT/CBCT pairs sorted in order of increasing F number (as defined in Equation 3.2) with or without the application of a replace-gas-by-tissue filter.

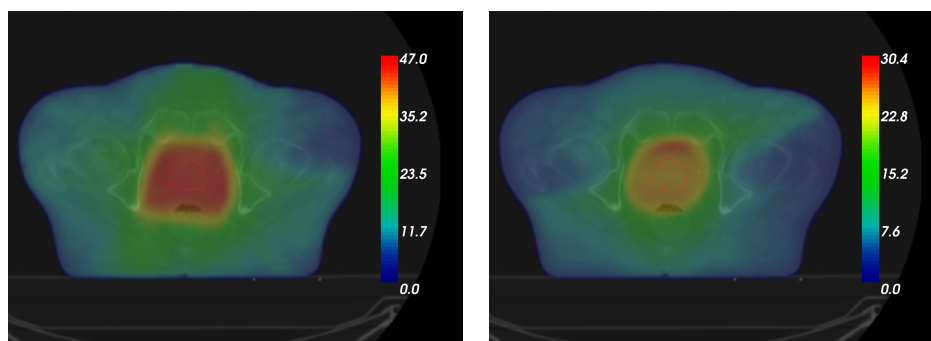


Figure 3.8: Slice of the planned dose distribution for Patient A for (a) the first IMAT course and (b) the second IMAT course.

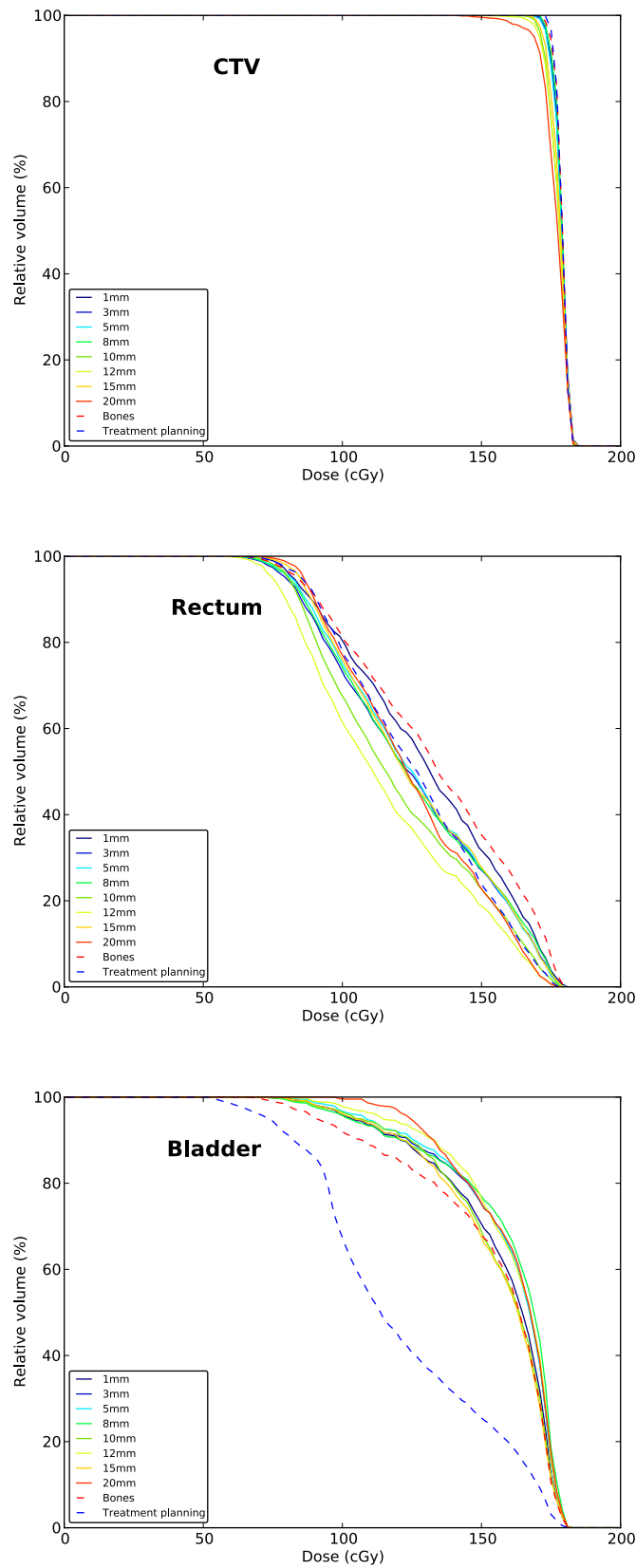


Figure 3.9: Patient A - 1st course: Comparison of the DVH obtained by bony RR and all local RR methods. To compute the DVHs, the manual CBCT contours are mapped onto the planned dose map using the different setup correction strategies (see Figure 3.4). The planned DVHs are also shown.

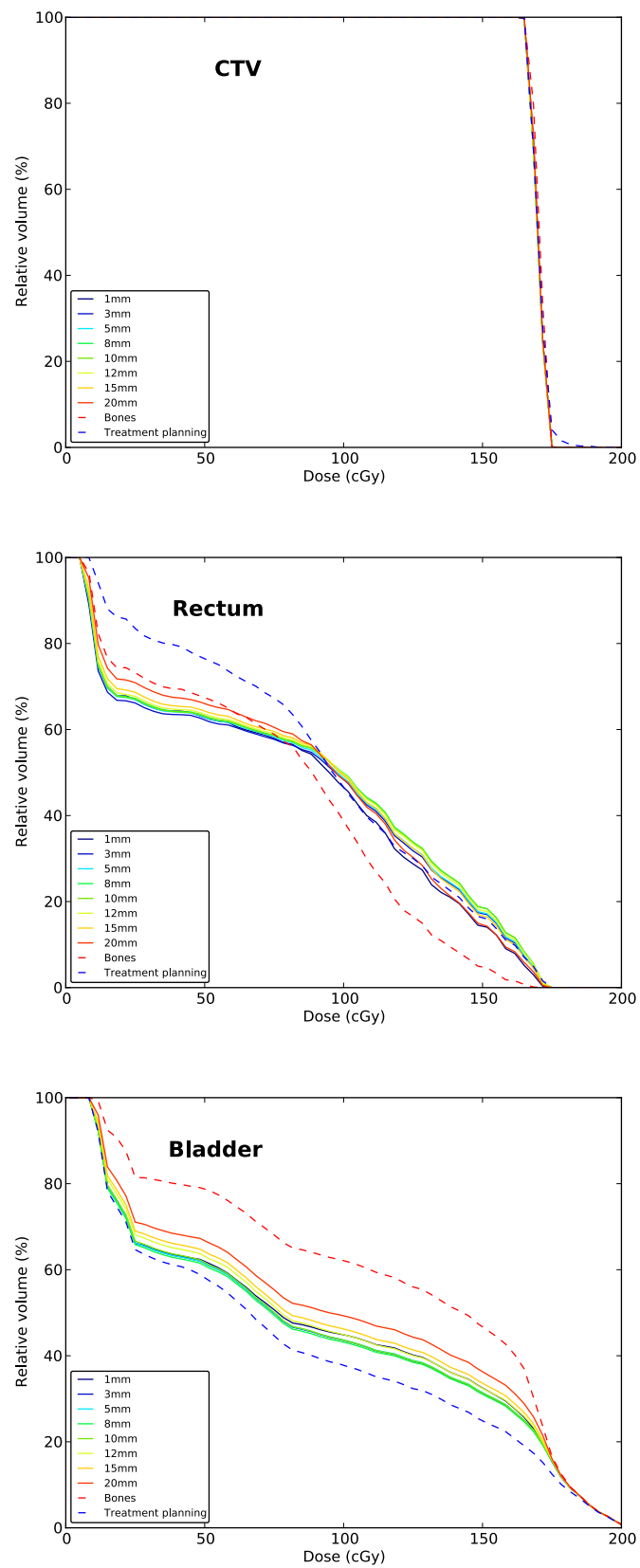
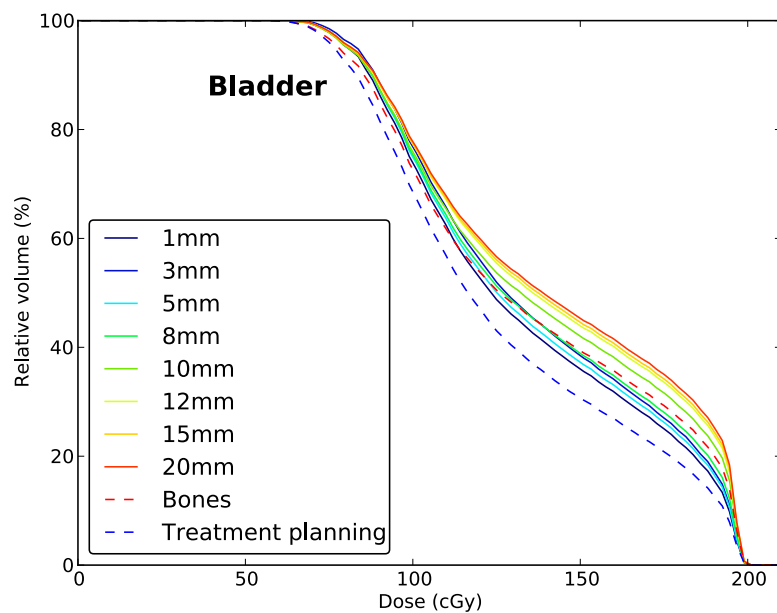
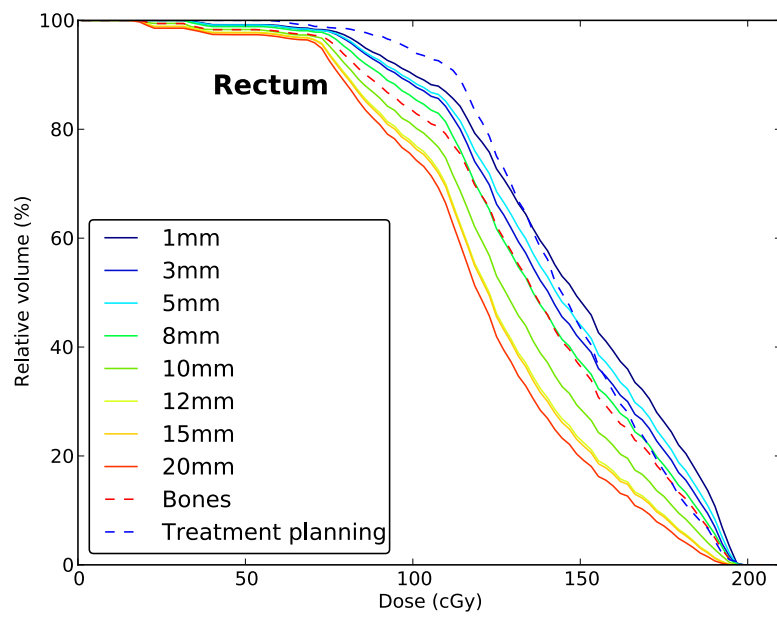
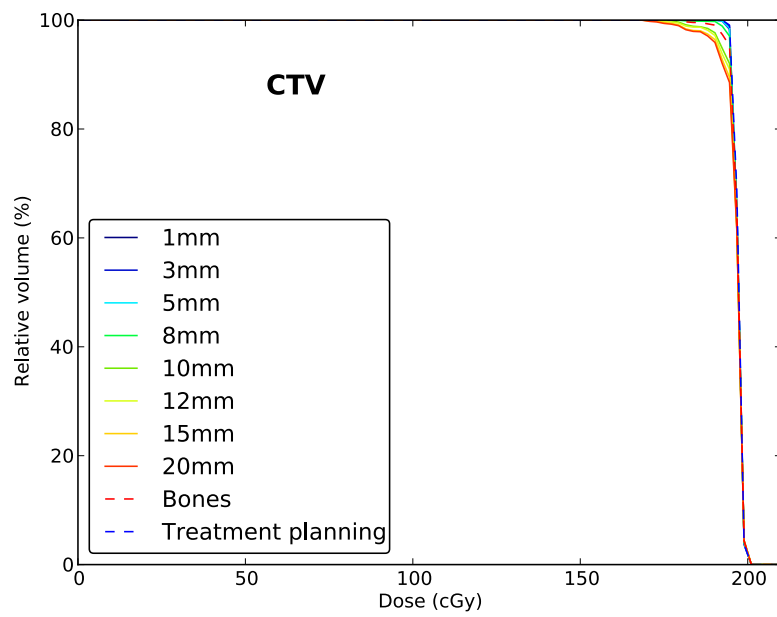


Figure 3.10: Patient A - 2nd course: Comparison of the DVH obtained by bony RR and all local RR methods. To compute the DVHs, the manual CBCT contours are mapped onto the planned dose map using the different setup correction strategies (see Figure 3.4). The planned DVHs are also shown..



3.4 Discussion

In this work, we evaluated different automatic methods for prostate localization based on intensity-based CT/CBCT RR. For the sake of simplicity, the term “local RR” was used in place of the combination of bony RR with local soft-tissue RR. On average, the execution times required by the global RR, the bony RR and the local RR were 54 s, 48 s and 1 min 10 s, respectively. Our statistical analysis showed that the most successful methods were the 5-mm and 8-mm local RRs. The success rate of the 8-mm local RR (95% of success when the air was not filtered in the rectum, and 97% of success when a replace-gas-by-tissue filter was applied) was higher than that of the 5-mm local RR and it is soundly acceptable for further implementation for clinical practice. Moreover, all automatic segmentations generated using the 8-mm local RR method (even in the unsuccessful cases) were visually considered acceptable for clinical use. In addition, we related the 8-mm local RR failures to rectal distension occurred in the vicinity of the prostate, which we estimated using an automatic method that could be easily applicable in clinical practice. We drew the conclusion that with a limited difference in rectum anatomy, an 8-mm local RR would improve the registration quality, i.e., the alignment of the registered images, and otherwise it would deteriorate the registration quality and should not be applied.

Many studies aiming to localize the prostate have been performed using daily in-room CT imaging as in [Lattanzi *et al.* 1998, Hua *et al.* 2003, Court & Dong 2003, Paskalev *et al.* 2004, Smitsmans *et al.* 2004]. In particular, Court *et al.* developed an automatic planning-CT/in-room-CT monomodal RR of the prostate for IGRT using a mask around the prostate. They studied the effect of the size of the registration mask using CTV expansions of 0, 3, 6 and 9 mm, and showed that the optimum expansion was 3 mm [Court & Dong 2003]. However, they quantitatively analyzed only 28 image sets from 2 patients and considered only translations. They also showed that in the presence of air in the rectum, filtering the air out of the registration mask produced better results. Later on, Smitsmans *et al.* conducted a study similar to ours with monomodal CT/CT RR with 19 patients and 8-13 repeat CT scans per patient, and they found the optimum margin was 5 mm [Smitsmans *et al.* 2004]. They also showed that applying a filter before registration that removed gas from the registration mask or that replaced rectal gas by soft tissue improved the results. To evaluate the results, they compared the results of intensity-based registration to that of contour registration (in terms of volume overlap, and mean and SD of the differences for each rotation and translation axis for successful registrations), the latter being used as a reference (contours were drawn manually on each planning and repeat CT scan).

Daily in-room CBCT imaging for prostate cancer was used in [Moseley *et al.* 2007, Barney *et al.* 2011, Boda-Heggemann *et al.* 2008, Létourneau *et al.* 2005, Perks *et al.* 2011, Smitsmans *et al.* 2005, Kim *et al.* 2010, Sato *et al.* 2012, Lee *et al.* 2012, Kasibhalta *et al.* 2005] but very few studies localized the prostate in a completely automatic way. In [Moseley *et al.* 2007, Barney *et al.* 2011], manual CT/CBCT soft-tissue RR and alignments of implanted fiducials using orthogonal kV or MV portal images and CBCT scans were compared to target the prostate. In [Boda-Heggemann *et al.* 2008], commercial software using an automatic intensity-based RR algorithm was used to align implanted I^{125} seeds. Without proposing a strategy to automatically localize the prostate on the CBCT scan, authors in [Létourneau *et al.* 2005] measured the residual setup error for prostate cancer patients after online CBCT-based setup correction using three radiopaque markers made of high-winding coils in the prostate and prostate contours drawn manually on the CT and CBCT scans. In [Perks *et al.* 2011], commercial software was used to perform an automatic intensity-based soft-tissue RR.

Kim *et al.* tested the effect of different similarity metrics and expansions (ranging

from 0 to 10 mm) for the prostate registration mask on automatic CT/CBCT registration quality [Kim *et al.* 2010]. They removed the gas and the pelvic bone from the registration mask. They found that expansion margins of 4-10 mm were equally successful. The registration accuracy was assessed using one natural prostate calcification in images (not a global measure) as well as qualitative visual evaluation. A minutely detailed inspection of their results showed us that among all the margins they had tested (from 0 mm to 10 mm), they had obtained the most accurate results with the 8-mm margin (mean \pm SD = 1.5 ± 0.7 mm, but more particularly the lowest maximum calcification mismatch error (3.6 mm)), which is in agreement with our results.

Smitsmans *et al.* automatically localized the prostate on CBCT scans using their above-mentioned algorithm with a 5-mm margin (assuming that the optimal margin found for CT/CT registration will be optimal for CT/CBCT registration as well) and a "replace-gas-by-tissue" filter [Smitsmans *et al.* 2005]. They also removed the pelvic bone and the prostate calcifications close to the border (subject to movement) from the registration mask. To evaluate the results, a visual inspection was performed (a registration was assessed as successful if the prostate could fit within the manual CT contours expanded by 3.6 mm and overlaid on the registered CBCT scan). Registration errors of calcification mismatch were determined for patients with calcifications within the prostate, and only for successful registrations. In our study, we showed that when we filtered the air in the rectum as done in [Smitsmans *et al.* 2004], we obtained an optimum margin of 8 mm (best accuracy in terms of Dice and BD values among all methods and a success rate of 97% better than the 83% success rate we obtained with the 5-mm margin). That said, margins between 8 mm and 15 mm yielded close results in terms of Dice median, SD, success rate and from a statistical point of view (as for the 20-mm local RR, it was not found to be significantly different from the global RR). The fact that we do not find the same optimum margin can stem from the nature of the images being registered (monomodal CT-to-CT registration versus multimodal CT-to-CBCT registration) and the nature of the validation (e.g., different definitions of registration success). In [Smitsmans *et al.* 2005], authors also reported that the CT/CBCT local RR with a 5-mm margin mainly failed because of streaks in the CBCT scans caused by moving gas pockets in the rectum but they did not propose an automatic and quantitative way to predict failures. In our study, we proposed an automatic method to estimate rectal distension to predict registration failures, using only the manual CT contours with the gray-value CT and CBCT images. The manual CBCT contours were not needed.

Treatment margin calculations Currently, CBCT-based daily verification and correction are widely performed using bony or soft-tissue (automatic or manual) RR in order to reduce setup error and inter-fraction organ motion. We proved that defining a daily verification and correction protocol of the patient setup before each prostate cancer treatment session using bony RR refined by a local RR with an 8-mm margin around the CTV as described in this chapter will reduce any further inter-fraction organ motion, allowing to reduce treatment margins. We calculated the new treatment margins that can be used after evaluating on clinical data the SD of random and systematic variations due to residual setup errors after setup correction (variations due to target volume delineation and organ motion were borrowed from [Rasch *et al.* 1999] and [van Herk *et al.* 1995]). We compared the treatment margins we obtained for bony RR and 8-mm local RR using Equation 3.5: 5.7 mm vs 7.4 mm along the LR axis, 10.1-12.9 mm vs 10.5-13 mm along the SI axis, 11.1 mm vs 12.6 mm along the AP axis, respectively. In [Smitsmans *et al.* 2004], Smitsmans *et al.* obtained the following treatment margins for the prostate between CTV and PTV after CT-based setup correction: 0.5 mm, 0.9 mm and 0.8 mm in LR, SI and AP directions,

respectively. However they did not include in their calculations motion errors and organ delineation errors. Also they assumed that systematic errors were negligible without giving numerical evidence for that, and hence they ignored the systematic term in Equation 3.5. In our work, we found that systematic errors were in the same order of magnitude as random errors. Elsewhere ([Meijer *et al.* 2008]), authors found that an anisotropic CTV-to-PTV treatment margin of 8 mm (9 mm at the apex) was **necessary** for a CT-based setup correction strategy using bony RR (alignment of the patient to the bony anatomy). Higher image quality for in-room CT scans with respect to in-room CBCT scans accounts for the fact that the margins we found are larger.

We note that for organ motion uncertainties, we used the data published in [van Herk *et al.* 1995]. These data represent the inter-fraction uncertainty about the mobility of the prostate relative to the bony anatomy. While this uncertainty is included in our setup uncertainties (when we use local prostate RR), we still need to consider the intra-fraction uncertainty about the mobility of the prostate relative to the bony anatomy. Intra-fraction organ motion should be smaller than inter-fraction organ motion and so when using inter-fraction organ motion errors, we tend to overestimate intra-fraction organ motion errors, and hence treatment margins with respect to organ motion errors.

Other types of errors should probably be considered as well in Van Herk’s treatment margin recipe, e.g. uncertainties due to (inter- and intra-observer) target volume delineation on CBCT scans or uncertainties due to differences in target volume delineation between CT and CBCT modalities. Authors determined the inter-observer variability of defining the prostate gland on CBCT in [White *et al.* 2009]. This will have the effect of increasing treatment margins but further reflection about how to integrate these errors in Van Herk’s treatment margin recipe is needed. If the CBCT-based setup correction protocol that is applied is not daily-based, that is to say if the verification and the correction of the target position is not performed at every treatment day, treatment margins must be increased consequently. Our last comment concerns a common practice for image-based setup correction protocols. Very often, only table shifts that exceed 3 mm in at least one direction (LR, SI or AP) are actually applied. If such practice is used, then in the calculation of the setup errors, all table shifts that are ignored (i.e. those that are lower than 3 mm in the three space directions) must be set to (0,0,0), causing an increase in treatment margins.

Future perspectives In this work, we did not study the inter/intra-observer variability in manual delineation, hence nor the amount of Dice uncertainty due to this variability. This can be investigated in a future study. White *et al.* have previously determined the inter-observer variability of defining the prostate on CBCT images in terms of variations in volume, center of mass, prostate boundary and consequent isocenter placement [White *et al.* 2009]. Weiss *et al.* have also analyzed inter/intra-observer contouring variations using standard deviation and average volume calculations [Weiss *et al.* 2010]. However, none of these studies calculated Dice coefficients of volumes delineated by different observers.

The method we proposed in this chapter to assess rectal distension could be applied in an adaptive radiotherapy approach. A future study could aim at assessing the impact of rectal distension on dose target coverage and organ-at-risk exposure. This could allow one to determine a cut-off value for rectal distension beyond which treatment replanning would become necessary.

3.5 Conclusion

With this study, we aimed to provide guidance for good practices in the use of CT-to-CBCT RR for prostate position verification and correction. We recommend to start with a bony RR. The next step is to determine whether a local RR with an 8-mm margin can be performed on top of the bony RR to improve upon registration quality. To do so, the user should estimate rectal distension occurred in the vicinity of the prostate between the planning CT scan and the treatment CBCT scan. In this chapter, we propose, a method to conduct such an evaluation that is easily applicable in clinical practice and automatic using only the manual CT contours and requiring calculations of mean intensities in the prostate and in the portion of the rectum included in the registration mask in both images after bony RR. If the difference in rectum anatomy is limited, the 8-mm local RR will improve registration quality and prostate targeting. If not, the 8-mm local RR may deteriorate registration quality and hence it should not be applied. We highly recommend that the user should always visually assess the final registration quality, particularly when a local RR is applied.

Bibliography

- [Balter *et al.* 1995] J. M. Balter, K. L. Lam, H. M. Sandler, J. F. Littles, R. L. Bree et R. K. Ten Haken. *Automated localization of the prostate at the time of treatment using implanted radiopaque markers: technical feasibility*. Int J Radiat Oncol Biol Phys, vol. 33, no. 5, pages 1281–1286, Dec 1995. (Cité en page 56.)
- [Barney *et al.* 2011] Brandon M. Barney, R Jeffrey Lee, Diana Handrahan, Keith T. Welsh, J Taylor Cook et William T. Sause. *Image-guided radiotherapy (IGRT) for prostate cancer comparing kV imaging of fiducial markers with cone beam computed tomography (CBCT)*. Int J Radiat Oncol Biol Phys, vol. 80, no. 1, pages 301–305, May 2011. (Cité en pages 56 et 77.)
- [Bergström *et al.* 1998] P. Bergström, P. O. Löfroth et A. Widmark. *High-precision conformal radiotherapy (HPCRT) of prostate cancer—a new technique for exact positioning of the prostate at the time of treatment*. Int J Radiat Oncol Biol Phys, vol. 42, no. 2, pages 305–311, Sep 1998. (Cité en page 56.)
- [Boda-Heggemann *et al.* 2008] Judit Boda-Heggemann, Frederick Marc Köhler, Hansjörg Wertz, Michael Ehmann, Brigitte Hermann, Nadja Riesenacker, Beate Küpper, Frank Lohr et Frederik Wenz. *Intrafraction motion of the prostate during an IMRT session: a fiducial-based 3D measurement with Cone-beam CT*. Radiat Oncol, vol. 3, page 37, 2008. (Cité en pages 56 et 77.)
- [Boydev *et al.* 2013] Christine Boydev, David Pasquier, Foued Derraz, Laurent Peyrodie, Abdelmalik Taleb-Ahmed et Jean-Philippe Thiran. *Automatic prostate segmentation in cone-beam computed tomography images using rigid registration*. Conf Proc IEEE Eng Med Biol Soc, vol. 2013, pages 3993–3997, 2013. (Cité en page 57.)
- [Boydev *et al.* 2015] Christine Boydev, Abdelmalik Taleb-Ahmed, Foued Derraz, Laurent Peyrodie, Jean-Philippe Thiran et David Pasquier. *Development of CBCT-based prostate setup correction strategies and impact of rectal distension*. Radiat Oncol, vol. 10, page 83, 2015. (Cité en page 57.)
- [Court & Dong 2003] Laurence E. Court et Lei Dong. *Automatic registration of the prostate for computed-tomography-guided radiotherapy*. Med Phys, vol. 30, no. 10, pages 2750–2757, Oct 2003. (Cité en pages 56 et 77.)
- [de Crevoisier *et al.* 2005] Renaud de Crevoisier, Susan L. Tucker, Lei Dong, Radhe Mohan, Rex Cheung, James D. Cox et Deborah A. Kuban. *Increased risk of biochemical and local failure in patients with distended rectum on the planning CT for prostate cancer radiotherapy*. Int J Radiat Oncol Biol Phys, vol. 62, no. 4, pages 965–973, Jul 2005. (Cité en page 56.)
- [Deurloo *et al.* 2005] Kirsten E I. Deurloo, Roel J H M. Steenbakkers, Lambert J. Zijp, Josien A. de Bois, Peter J C M. Nowak, Coen R N. Rasch et Marcel van Herk. *Quantification of shape variation of prostate and seminal vesicles during external beam radiotherapy*. Int J Radiat Oncol Biol Phys, vol. 61, no. 1, pages 228–238, Jan 2005. (Cité en pages 56 et 116.)
- [Dice 1945] Lee Raymond Dice. *Measures of the Amount of Ecologic Association Between Species*. Ecology, vol. 26, no. 3, pages 297–302, July 1945. (Cité en page 60.)
- [Gill *et al.* 2011] Suki Gill, Jessica Thomas, Chris Fox, Tomas Kron, Aldo Rolfo, Mary Leahy, Sarat Chander, Scott Williams, Keen Hun Tai, Gillian M. Duchesne et

- Farshad Foroudi. *Acute toxicity in prostate cancer patients treated with and without image-guided radiotherapy*. Radiat Oncol, vol. 6, page 145, 2011. (Cité en page 56.)
- [Hollander & Wolfe 1999] Myles Hollander et Douglas A. Wolfe. *Nonparametric statistical methods*, 1999. Wiley-Interscience. (Cité en page 60.)
- [Hua *et al.* 2003] Chiaho Hua, D Michael Lovelock, Gikas S. Mageras, Matthew S. Katz, James Mechalakos, Eugene P. Lief, Timothy Hollister, Wendell R. Lutz, Michael J. Zelefsky et Clifton C. Ling. *Development of a semi-automatic alignment tool for accelerated localization of the prostate*. Int J Radiat Oncol Biol Phys, vol. 55, no. 3, pages 811–824, Mar 2003. (Cité en pages 56 et 77.)
- [Ibanez *et al.* 2005] Luis Ibanez, Will Schroeder, Lydia Ng, Josh Cates et The Insight Software Consortium. *The ITK Software Guide*. Kitware, Inc.; 2005, second édition, 2005. (Cité en pages 13, 59, 99 et 100.)
- [Jaffray *et al.* 2002] David A. Jaffray, Jeffrey H. Siewerdsen, John W. Wong et Alvaro A. Martinez. *Flat-panel cone-beam computed tomography for image-guided radiation therapy*. Int J Radiat Oncol Biol Phys, vol. 53, no. 5, pages 1337–1349, Aug 2002. (Cité en pages 31 et 56.)
- [Kasibhalta *et al.* 2005] M. Kasibhalta, S. Yoo, F. Yin, D. Godfrey, M. Oldham et S.K. Das. *Assessment of setup accuracy for prostate radiotherapy using on-board imaging and cone beam computed tomography [abstract]*. Int J of Radiat Oncol Biol Phys, vol. 63, page S535, 2005. (Cité en pages 56 et 77.)
- [Kim *et al.* 2010] Jinkoo Kim, Rabih Hammoud, Deepak Pradhan, Hualiang Zhong, Ryan Y. Jin, Benjamin Movsas et Indrin J. Chetty. *Prostate localization on daily cone-beam computed tomography images: accuracy assessment of similarity metrics*. Int J Radiat Oncol Biol Phys, vol. 77, no. 4, pages 1257–1265, Jul 2010. (Cité en pages 56, 77 et 78.)
- [Kim *et al.* 2012] Hak Soo Kim, Samuel B. Park, Simon S. Lo, James I. Monroe et Jason W. Sohn. *Bidirectional local distance measure for comparing segmentations*. Med Phys, vol. 39, no. 11, pages 6779–6790, Nov 2012. (Cité en page 61.)
- [Langen *et al.* 2008] Katja M. Langen, Twyla R. Willoughby, Sanford L. Meeks, Anand Santhanam, Alexis Cunningham, Lisa Levine et Patrick A. Kupelian. *Observations on real-time prostate gland motion using electromagnetic tracking*. Int J Radiat Oncol Biol Phys, vol. 71, no. 4, pages 1084–1090, Jul 2008. (Cité en page 56.)
- [Lattanzi *et al.* 1998] J. Lattanzi, S. McNeely, A. Hanlon, I. Das, T. E. Schultheiss et G. E. Hanks. *Daily CT localization for correcting portal errors in the treatment of prostate cancer*. Int J Radiat Oncol Biol Phys, vol. 41, no. 5, pages 1079–1086, Jul 1998. (Cité en pages 56 et 77.)
- [Lee *et al.* 2012] Y. Lee, J.R. Perks, S.K. Yi, R.L. Stern et R.K. Valicenti. *Daily localization comparison between kilovoltage cone beam computed tomography and electromagnetic tracking system for intensity modulated radiation therapy-treated prostate patients [abstract]*. Int J of Radiat Oncol Biol Phys, vol. 84, page S744, 2012. (Cité en pages 56 et 77.)
- [Létourneau *et al.* 2005] Daniel Létourneau, Alvaro A. Martinez, David Lockman, Di Yan, Carlos Vargas, Giovanni Ivaldi et John Wong. *Assessment of residual error for online cone-beam CT-guided treatment of prostate cancer patients*. Int J Radiat

- Oncol Biol Phys, vol. 62, no. 4, pages 1239–1246, Jul 2005. (Cité en pages 56 et 77.)
- [Martin *et al.* 2009] Jarad M. Martin, Andrew Bayley, Robert Bristow, Peter Chung, Mary Gospodarowicz, Cynthia Menard, Michael Milosevic, Tara Rosewall, Pdraig R. Warde et Charles N. Catton. *Image guided dose escalated prostate radiotherapy: still room to improve*. Radiat Oncol, vol. 4, page 50, 2009. (Cité en page 56.)
- [Meijer *et al.* 2008] Gert J. Meijer, Jeroen de Klerk, Karl Bzdusek, Hetty A. van den Berg, Rogier Janssen, Michael R. Kaus, Patrick Rodrigus et Peter-Paul van der Toorn. *What CTV-to-PTV margins should be applied for prostate irradiation? Four-dimensional quantitative assessment using model-based deformable image registration techniques*. Int J Radiat Oncol Biol Phys, vol. 72, no. 5, pages 1416–1425, Dec 2008. (Cité en page 79.)
- [Morgan-Fletcher 2001] S L Morgan-Fletcher. *Prescribing, Recording and Reporting Photon Beam Therapy (Supplement to ICRU Report 50), ICRU Report 62. ICRU, pp. ix+52, 1999 (ICRU Bethesda, MD)*. The British Journal of Radiology, vol. 74, no. 879, pages 294–294, 2001. (Cité en page 57.)
- [Moseley *et al.* 2007] Douglas J. Moseley, Elizabeth A. White, Kirsty L. Wiltshire, Tara Rosewall, Michael B. Sharpe, Jeffrey H. Siewerdsen, Jean-Pierre Bissonnette, Mary Gospodarowicz, Pdraig Warde, Charles N. Catton et David A. Jaffray. *Comparison of localization performance with implanted fiducial markers and cone-beam computed tomography for on-line image-guided radiotherapy of the prostate*. Int J Radiat Oncol Biol Phys, vol. 67, no. 3, pages 942–953, Mar 2007. (Cité en pages 56 et 77.)
- [Orton *et al.* 2006] Nigel P. Orton, Hazim A. Jaradat et Wolfgang A. Tomé. *Clinical assessment of three-dimensional ultrasound prostate localization for external beam radiotherapy*. Med Phys, vol. 33, no. 12, pages 4710–4717, Dec 2006. (Cité en page 56.)
- [Padhani *et al.* 1999] A. R. Padhani, V. S. Khoo, J. Suckling, J. E. Husband, M. O. Leach et D. P. Dearnaley. *Evaluating the effect of rectal distension and rectal movement on prostate gland position using cine MRI*. Int J Radiat Oncol Biol Phys, vol. 44, no. 3, pages 525–533, Jun 1999. (Cité en page 56.)
- [Paskalev *et al.* 2004] K. Paskalev, C. M. Ma, R. Jacob, R. Price, S. McNeeley, L. Wang, B. Movsas et A. Pollack. *Daily target localization for prostate patients based on 3D image correlation*. Phys Med Biol, vol. 49, no. 6, pages 931–939, Mar 2004. (Cité en pages 56 et 77.)
- [Perks *et al.* 2011] Julian Perks, Helen Turnbull, Tianxiao Liu, James Purdy et Richard Valicenti. *Vector analysis of prostate patient setup with image-guided radiation therapy via kV cone beam computed tomography*. Int J Radiat Oncol Biol Phys, vol. 79, no. 3, pages 915–919, Mar 2011. (Cité en pages 56 et 77.)
- [Rasch *et al.* 1999] C. Rasch, I. Barillot, P. Remeijer, A. Touw, M. van Herk et J. V. Lebesque. *Definition of the prostate in CT and MRI: a multi-observer study*. Int J Radiat Oncol Biol Phys, vol. 43, no. 1, pages 57–66, Jan 1999. (Cité en pages 63 et 78.)
- [Roeske *et al.* 1995] J. C. Roeske, J. D. Forman, C. F. Mesina, T. He, C. A. Pelizzari, E. Fontenla, S. Vijayakumar et G.T. Chen. *Evaluation of changes in the size and location of the prostate, seminal vesicles, bladder, and rectum during a course of external beam radiation therapy*. Int J Radiat Oncol Biol Phys, vol. 33, no. 5, pages 1321–1329, Dec 1995. (Cité en page 56.)

- [Sato *et al.* 2012] H. Sato, E. Abe et H. Aoyama. *Comparison of soft-tissue matching on daily cone beam computed tomography and fluoroscopy-based bony-structure matching in the target localization for the IMRT of prostate cancer [abstract]*. Int J of Radiat Oncol Biol Phys, vol. 84, page S363, 2012. (Cité en pages 56 et 77.)
- [Siewerdsen & Jaffray 2001] J. H. Siewerdsen et D. A. Jaffray. *Cone-beam computed tomography with a flat-panel imager: magnitude and effects of x-ray scatter*. Med Phys, vol. 28, no. 2, pages 220–231, Feb 2001. (Cité en pages 31 et 56.)
- [Smitsmans *et al.* 2004] Monique H P. Smitsmans, Jochem W H. Wolthaus, Xavier Artignan, Josien de Bois, David A. Jaffray, Joos V. Lebesque et Marcel van Herk. *Automatic localization of the prostate for on-line or off-line image-guided radiotherapy*. Int J Radiat Oncol Biol Phys, vol. 60, no. 2, pages 623–635, Oct 2004. (Cité en pages 56, 57, 77 et 78.)
- [Smitsmans *et al.* 2005] Monique H P. Smitsmans, Josien de Bois, Jan-Jakob Sonke, Anja Betgen, Lambert J. Zijp, David A. Jaffray, Joos V. Lebesque et Marcel van Herk. *Automatic prostate localization on cone-beam CT scans for high precision image-guided radiotherapy*. Int J Radiat Oncol Biol Phys, vol. 63, no. 4, pages 975–984, Nov 2005. (Cité en pages 56, 77 et 78.)
- [Sveistrup *et al.* 2014] Joen Sveistrup, Per Munck af Rosenschöld, Joseph O. Deasy, Jung Hun Oh, Tobias Pommer, Peter Meidahl Petersen et Svend Aage Engelholm. *Improvement in toxicity in high risk prostate cancer patients treated with image-guided intensity-modulated radiotherapy compared to 3D conformal radiotherapy without daily image guidance*. Radiat Oncol, vol. 9, page 44, 2014. (Cité en page 56.)
- [Team 2012] R Core Team. *R: A language and environment for statistical computing*. R Foundation for Statistical Computing. Vienna, Austria, 2012. (Cité en page 59.)
- [Thilmann *et al.* 2006] Christoph Thilmann, Simeon Nill, Thomas Tücking, Angelika Höss, Bernd Hesse, Lars Dietrich, Rolf Bendl, Bernhard Rhein, Peter Häring, Christian Thieke, Uwe Oelfke, Juergen Debus et Peter Huber. *Correction of patient positioning errors based on in-line cone beam CTs: clinical implementation and first experiences*. Radiat Oncol, vol. 1, page 16, 2006. (Cité en page 56.)
- [van Herk *et al.* 1995] M. van Herk, A. Bruce, A. P. Kroes, T. Shouman, A. Touw et J. V. Lebesque. *Quantification of organ motion during conformal radiotherapy of the prostate by three dimensional image registration*. Int J Radiat Oncol Biol Phys, vol. 33, no. 5, pages 1311–1320, Dec 1995. (Cité en pages 56, 63, 78, 79 et 116.)
- [van Herk *et al.* 2000] M. van Herk, P. Remeijer, C. Rasch et J. V. Lebesque. *The probability of correct target dosage: dose-population histograms for deriving treatment margins in radiotherapy*. Int J Radiat Oncol Biol Phys, vol. 47, no. 4, pages 1121–1135, Jul 2000. (Cité en page 56.)
- [van Herk *et al.* 2002] Marcel van Herk, Peter Remeijer et Joos V. Lebesque. *Inclusion of geometric uncertainties in treatment plan evaluation*. Int J Radiat Oncol Biol Phys, vol. 52, no. 5, pages 1407–1422, Apr 2002. (Cité en page 63.)
- [Weiss *et al.* 2010] Elisabeth Weiss, Jian Wu, William Sleeman, Joshua Bryant, Priya Mitra, Michael Myers, Tatjana Ivanova, Nitai Mukhopadhyay, Viswanathan Ramakrishnan, Martin Murphy et Jeffrey Williamson. *Clinical evaluation of soft tissue organ boundary visualization on cone-beam computed tomographic imaging*. Int J Radiat Oncol Biol Phys, vol. 78, no. 3, pages 929–936, Nov 2010. (Cité en page 79.)

- [White *et al.* 2009] E. A. White, K. K. Brock, D. A. Jaffray et C. N. Catton. *Inter-observer variability of prostate delineation on cone beam computerised tomography images*. Clin Oncol (R Coll Radiol), vol. 21, no. 1, pages 32–38, Feb 2009. (Cité en page 79.)

A new energy for joint segmentation and deformable registration

Contents

5.1	Contributions	115
5.2	Perspectives	117
	Bibliography	119

4.1 Background

Deformable image registration (DIR) is an important integral part of ART (Section 1.2.6.2). As already stated in Chapter 1, registering a daily CBCT image with a planning CT image is extremely challenging in the pelvis. In addition to poor CBCT image quality due to low contrast and streak artifacts (caused by moving gas during CBCT acquisition), significant daily variations in rectal and bladder fillings make DIR difficult, in particular in the rectum where sometimes there may be no intensity-based correspondence. Figure 4.1, extracted from [Smitsmans *et al.* 2008], illustrates the change in the appearance of the rectum which highly depends on the quantity of feces, gas and moving gas.

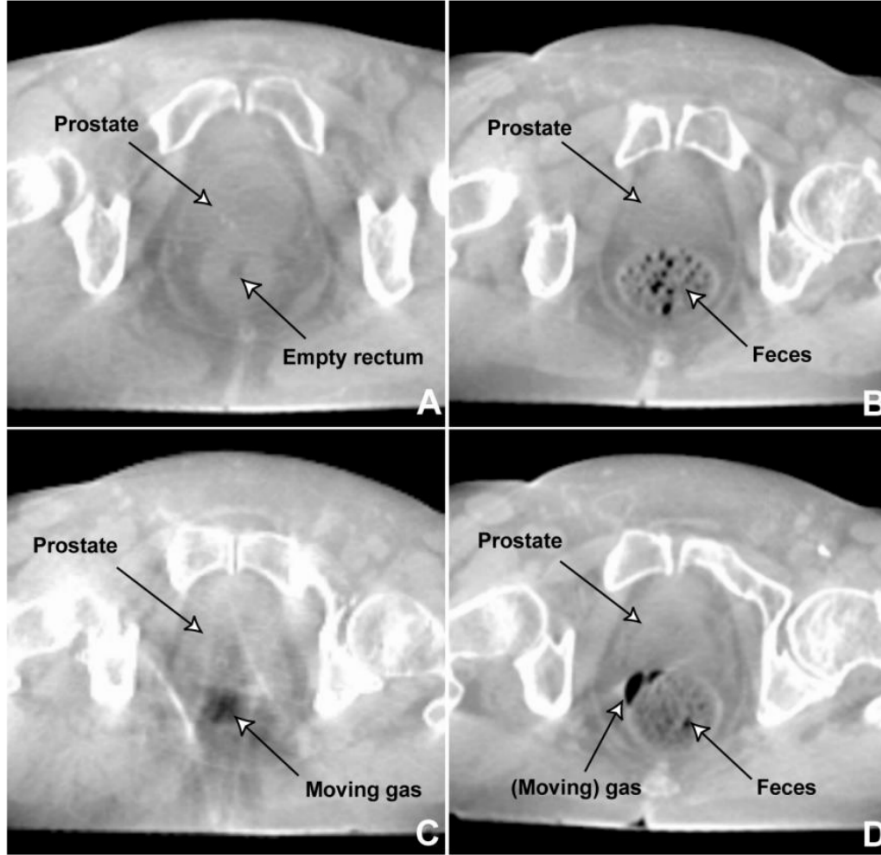


Figure 4.1: Transverse slices of CBCT scans with (A) empty rectum (visible prostate), (B) rectum containing feces and small gas pockets (visible prostate), (C) rectum with moving gas pocket (streak artifacts; hardly visible prostate), and (D) rectum with feces and a slightly moving gas pocket (white streak artifacts at gas pocket edges; large part of prostate is visible). (figure extracted from [Smitsmans *et al.* 2008])

There have been a small number of works that tackle the problem of CT-to-CBCT DIR in the pelvis. Besides, very often the approach is not fully automatic and makes use of manually-identified features or segmentations to constraint registration.

In [Thor *et al.* 2011], the authors tested an automatic commercial software based on the “Demons” algorithm (MIRS, Varian Medical System, Palo Alto, CA) on five prostate cancer patients, and showed high disparities in the Dice coefficients between the automatic and manual segmentations of the prostate ($\overline{DSC} = 0.80$, range [0.65 – 0.87]), the rectum ($\overline{DSC} = 0.77$, range [0.63 – 0.87]) and the bladder ($\overline{DSC} = 0.73$, range [0.34 – 0.91]). More importantly, their visual slice-by-slice evaluation concluded that the automatic segmentations of the prostate, rectum and bladder were considered unacceptable on 56%, 81% and 67% of the scans, respectively, making the algorithm unsuitable for dose accumulation and treatment adaptation purposes.

In [Kim *et al.* 2013], the authors perform a CT-to-CBCT DIR using three kinds of constraints: manual segmentations of the rectum, the bladder and the prostate on both images, a number of distinctive points manually identified on both images and a rigidity penalty imposed on the femurs and pelvic bones. And hence the method is not fully automatic in the sense that they use manually-identified points and surfaces.

In [Paquin *et al.* 2009], the authors performed a landmark-based RR based on manually-selected landmarks followed by a multiscale free-form deformation (FFD) DIR based on B-splines. However, the evaluation of the registrations of their clinical images is only based on the calculation of the mutual information similarity between the CT and the CBCT images, before and after registration. However, the image similarity used by the optimizer should not be used alone to evaluate the registration results. For instance, not realistic/clinically-acceptable deformations can yield fair similarity measures. In particular, in [Rohlfing 2012], the author demonstrates that image similarity does not provide valid evidence for accurate registrations (as well as tissue overlaps).

In [Greene *et al.* 2009, Lu *et al.* 2010], the authors used pre-defined manual segmentations of the organs of interest (prostate, bladder, rectum and bones) to softly and hardly constrain a deformable registration (by using the method of Lagrange multipliers for the hardly constrained registration), respectively. Lu *et al.* also proposed an integrated automatic segmentation and softly constrained non-rigid registration algorithm using a Bayesian framework for application in prostate, without relying on manual segmentation (CBCT-based or MR-based) IGRT [Lu *et al.* 2011]. Segmentation and registration alternatively constrain each other in the loop, at each new step of the optimization process. The treatment-day image segmentation part consists of evolving level-set deformable models using the intensity-based region segmentation model of Chan-Vese (active contours without edges model [Chan & Vese 2001]) under the constraint of a statistical shape prior retrieved from a training database of images, and the constraint of the structures mapped from the planning image using the current iterative mapping estimate. The registration part is a hierarchical multi-resolution FFD transformation model based on cubic B-splines and constrained by the matching between the manual planning-day segmentations and the treatment-day segmentations estimated at the current iteration. Images were downsampled to a spatial resolution of 4 mm x 4 mm x 4 mm. The images were acquired from patients who underwent a protocol that eliminated the bowel gas from the rectum prior to imaging. This had the effect of circumventing the challenging problem of dealing with variations in the intensity appearance of the rectum, which commonly causes registration failures, or heterogeneous rectums, which makes segmentation difficult.

It is worth mentioning the interesting work of Chen *et al.* on the automatic segmentation of the prostate, bladder and rectum on CBCT images [Chen *et al.* 2009]. They use a segmentation framework. Their three-stage approach first consists of evolving deformable models to segment automatically and simultaneously the organs on the CT image using the level set formulation. Secondly, they find a displacement field (driven by Demons forces) between the CT and the CBCT only at points belonging to the surfaces of the organs in the CT image, which allows them to estimate automatic CBCT segmentations. Finally, they use the latter to initialize a segmentation process on the CBCT image using again deformable models. However, their approach does not retrieve a dense deformation field and hence cannot be used for IGART (Section 1.2.6.2).

In this chapter, our approach is to use a joint segmentation and registration variational framework to localize the prostate, the bladder and the rectum on in-room CBCT scans for use in IGART. We simultaneously solve for segmentation and registration. A crucial motivation for our approach was the desire to use the (known) contours of the organs of interest delineated on the initial planning CT scan by the radiation oncologist

for treatment planning in order to guide the algorithm through the process of finding the corresponding boundaries on the CBCT scan. For sake of simplicity, without loss of generality, we consider only one organ of interest. The statement of the problem is as follows. We wish to register two images under the assumption that the segmentation of an object of interest is known/available in one of the images. The method naturally combines the registration of a fixed image, that is, the initial planning CT scan, to a moving image, that is, the daily CBCT scan, with the evolution of an active contour on the moving image. The active contour merely corresponds to the known segmentation of the given object in the fixed image after propagation using the estimate of the transformation at the current iteration of the registration process. The integration of segmentation and registration is embedded in the formulation of the energy as a weighted sum of both contributions. The segmentation term of the proposed method is an adaptation of the localized version of the global region segmentation model of Chan and Vese [Lankton & Tannenbaum 2008], for use in a registration framework. As a reminder, the segmentation energy functional of Chan and Vese describes a curve evolution problem and assumes that the intensities of the foreground and the background of the image are uniform (piecewise constant intensities) [Chan & Vese 2001]. The energy, developed solely for the purpose of segmentation is expressed as a weighted sum of two fidelity terms and two regularization terms (the length of the active contour and its inner area) in the following way:

$$\begin{aligned}
 E(c_1, c_2, \Phi) = & \lambda_1 \int_{\Omega} H(\Phi(\mathbf{x})) (I(\mathbf{x}) - c_1)^2 d\mathbf{x} + \lambda_2 \int_{\Omega} [1 - H(\Phi(\mathbf{x}))] (I(\mathbf{x}) - c_2)^2 d\mathbf{x} \\
 & + \mu \int_{\Omega} \delta(\Phi(\mathbf{x})) |\nabla \Phi(\mathbf{x})| d\mathbf{x} + \nu \int_{\Omega} H(\Phi(\mathbf{x})) d\mathbf{x}
 \end{aligned} \tag{4.1}$$

where I is the image to segment, Φ is the level set function representing the active contour which seeks to detect the object of interest, H is the Heaviside function, and c_1 and c_2 are the intensity means of the inner and the outer regions of the contour, respectively. An implicit representation of the active contour based on level sets is used, which has several advantages including contour topology preservation (no contour splitting or merging possible). In a level set formulation, a curve C is represented implicitly by the zero-level of a Lipschitz function Φ as follows: $C = \{\mathbf{x} / \Phi(\mathbf{x}) = 0\}$. This is a pure segmentation problem in that the energy to minimize is a function of a function, here a function of Φ . The calculus of variations (Euler-Lagrange equation) and the gradient descent method are used to find an optimal solution for Φ . Later on, Lankton *et al.* proposed a natural framework that allowed any region-based segmentation energy, including that of Chan-Vese, to be re-formulated in a local way [Lankton & Tannenbaum 2008]. Local image statistics in the neighborhood of each point along the evolving contour are calculated rather than global image statistics, which is beneficial for the segmentation of objects with heterogeneous feature profiles, as depicted in Figure 4.2. The energy functional that is minimized is:

$$E(\Phi) = \int_{\Omega} \delta \Phi(\mathbf{x}) \int_{\Omega} \mathcal{B}(\mathbf{x}, \mathbf{y}) F(I(\mathbf{y}), \phi(\mathbf{y})) d\mathbf{y} d\mathbf{x} + \lambda \int_{\Omega} \delta \Phi(\mathbf{x}) \|\nabla \Phi(\mathbf{x})\| d\mathbf{x} \tag{4.2}$$

where $\mathcal{B}(\mathbf{x}, \mathbf{y})$ is used to mask local regions, and selects all points y belonging to a ball of a given radius centered on point x , and u_x and v_x denote the intensity means in the local interior and the local exterior of the contour at point x , localized by $\mathcal{B}(\mathbf{x}, \mathbf{y})$, respectively. In particular,

$$F(I(\mathbf{y}), \phi(\mathbf{y})) = H(\Phi(\mathbf{y})) (I(\mathbf{y}) - u_x)^2 + [1 - H(\Phi(\mathbf{y}))] (I(\mathbf{y}) - v_x)^2$$

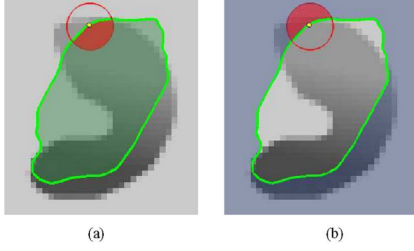


Figure 4.2: Lankton *et al.* propose a localized version of region-based segmentation energies where image statistics are calculated in the neighborhood of each point along the evolving contour, divided into (a) a local interior shaded in red and (b) an a local exterior shaded in red. (figure extracted from [Lankton & Tannenbaum 2008])

for the piecewise-constant region-based segmentation functional of Chan-Vese.

In the hereafter, a selected number of previous studies that look similar to ours in the methodology - in trying to combine segmentation and registration - are presented.

In [Yezzi *et al.* 2003], the authors tackle a similar problem, the main differences being that they aim at segmenting both images (so no known segmentation is available on any of the images) by evolving two separate active contours and they use a rigid transformation to map one segmentation to the other. Hence, two contours, C and \hat{C} , are jointly deformed. They exploit the global region segmentation model of Chan and Vese [Chan & Vese 2001]. On the basis of Equation 4.1, albeit with an explicit curve representation (no level sets used), Yezzi *et al.* formulate an energy as the sum of the energies of both curves, C and \hat{C} , while enforcing the relationship $\hat{C} = g(C)$, as follows:

$$E(g, C) = E_1(C) + E_2(g(C)) \quad (4.3)$$

$$\begin{aligned} &= \int_{C_{in}} |I(\mathbf{x}) - c_1|^2 d\mathbf{x} + \int_{C_{out}} |I(\mathbf{x}) - c_2|^2 d\mathbf{x} \\ &\quad + \int_{\hat{C}_{in}} |\hat{I}(\mathbf{x}) - \hat{c}_1|^2 d\mathbf{x} + \int_{\hat{C}_{out}} |\hat{I}(\mathbf{x}) - \hat{c}_2|^2 d\mathbf{x} \end{aligned} \quad (4.4)$$

where C_{in} and C_{out} are the regions inside and outside C , respectively, and \hat{C}_{in} and \hat{C}_{out} are the regions inside and outside \hat{C} , respectively. They use segmentation techniques (calculus of variations) to minimize their energy functional comprised of two unknowns, one of the two evolving curves and the rigid mapping, g .

Another valuable piece of work is that of Unal *et al.* who generalize the above-mentioned work of Yezzi *et al.* in the presence of non-rigid transformations. However, they solve for a deformation field only over the surface of the organ to segment in the two images [Unal & Slabaugh 2005] through coupled partial differential equations (PDEs), whereas we solve for a dense deformation field. One curve, denoted by C , deforms on the first image and one curve, denoted by \hat{C} , deforms on the second image. They use segmentation techniques to estimate two unknowns, the deformation field, $\mathbf{u}(\mathbf{x}, \mathbf{y})$, that maps one curve to the other and one of the two evolving segmenting curves (the other is obtained using the deformation field). Both contours, represented by level sets, move according to a generic global region-based energy functional defined over both image domains, Ω and $\hat{\Omega}$, as follows:

$$E(\Phi, \mathbf{u}) = E_1(C) + E_2(T(C)) \quad (4.5)$$

$$\begin{aligned} &= \int_{\Omega} H(\Phi(\mathbf{x})) F_{in}(\mathbf{x}) d\mathbf{x} + \int_{\Omega} [1 - H(\Phi(\mathbf{x}))] F_{out}(\mathbf{x}) d\mathbf{x} \\ &\quad + \int_{\hat{\Omega}} H(\hat{\Phi}(\hat{\mathbf{x}})) \hat{F}_{in}(\hat{\mathbf{x}}) d\hat{\mathbf{x}} + \int_{\hat{\Omega}} [1 - H(\hat{\Phi}(\hat{\mathbf{x}}))] \hat{F}_{out}(\hat{\mathbf{x}}) d\hat{\mathbf{x}} \\ &\quad + \int_{\Omega} \delta(\Phi) |\nabla \Phi|^2 d\mathbf{x} + \int_{\Omega} |\nabla \mathbf{u}(\mathbf{x})|^2 d\mathbf{x} \end{aligned} \quad (4.6)$$

where T is the non-rigid mapping such that $T(C) = \hat{C}$, $\hat{\mathbf{x}} = T(\mathbf{x}) = \mathbf{x} + \mathbf{u}(\mathbf{x})$, F_{in} and F_{out} the region descriptors inside and outside contour C (same for \hat{F}_{in} , \hat{F}_{out} and \hat{C}). Other major differences between this model and ours are: we use local, rather than global, image statistics to calculate the segmentation term, we do not optimize Φ and u alternatively but only u , and u is calculated over the whole image domain. We wish to make a critical remark regarding the following assumption formulated in [Unal & Slabaugh 2005]: $\hat{\Phi}(\mathbf{x} + \mathbf{u}) = \Phi(\mathbf{x})$. In fact, this is true only in the case of rigid transformations (e.g. this is safely used in [Yezzi *et al.* 2003]) and no evidence has been provided by the authors that the difference can be considered negligible.

The latter assumption is also used in [Carole Le Guyader 2009] where an unusual combined segmentation and registration framework is proposed. It can be considered as a topology-preserving level-set-based surrogate for the popular Chan-Vese segmentation framework. An image is segmented based on the active contour without edges proposed by Chan and Vese [Chan & Vese 2001] and the displacement vector field between the curve served for initialization (represented by a binary image) and the evolving segmenting curve (also represented by a binary image) is regularized by a non-linear elasticity-based smoother. The energy functional, expressed as a weighted sum of the segmentation term and the regularization term in terms of the displacement field, is minimized using the calculus of variations (Euler-Lagrange equation). In our work, we do not make this assumption. The unknown is the displacement field between a gray-value fixed image and a gray-value moving image. The level-set function representing the evolving segmenting curve in the moving image is not an unknown as the evolving curve is simply the estimate of the object contour in the moving image obtained from the propagation of the known object contour in the fixed image using the current estimate of the deformation field.

In our work, we propose a natural joint segmentation and registration problem formulation where the above-mentioned localized version of the segmentation model of Chan-Vese [Lankton & Tannenbaum 2008] is integrated in the registration framework. There has not been any other work accomplishing the combination of a segmentation energy term based on local image statistics and a registration energy term. We recall that our main goal is to obtain a dense deformation field for use in IGART. Our decision to guide the registration process by a region-based segmentation term is driven by the desire to overcome the problem of low contrast in the CBCT image using the more or less reliable saliency of the boundaries of the organs in the pelvis. Furthermore, our decision to use local, rather than global, image statistics for the segmentation term was motivated by the intensity inhomogeneity within the prostate and, more importantly, within the rectum, as well as within the soft tissue between the organs. In fact, the use of a global region-based segmentation models is inappropriate for our application per se as it would assume that the inner and outer regions of the object to segment are homogeneous. Even the use of a narrow band around the evolving contour would result in involving pixels of very different intensities in the calculation of the inner and outer image statistics, respectively, causing the evolving curve to fail in converging towards the organ boundary.

4.2 Methods

In this section, the mathematical framework for the proposed joint registration and segmentation method is described thoroughly. The notations and the formulation of the introduced method are first presented, and after that, the derivations that lead to the resolution of the problem.

4.2.1 Description of the proposed model

The combination of segmentation and registration takes place in the formulation of the energy to minimize, designed as a weighted sum of two complementary components:

The similarity term The first component is a registration fidelity term, a global intensity-based image similarity that drives the registration and estimates a dense deformation field that maps the fixed image to the moving image in their entirety. For consistency with Chapter 3, the NCC similarity measure was used (Section 1.3). We recall that the NCC can be used for inter-modality registration providing that there is a linear relation between the intensity histograms of both images, as is the case for CT and CBCT. In particular, the NCC was used by Yang *et al.* to register the planning CT to the daily CBCT with cubic B-spline FFD transformations in their study on CBCT-based dose calculation (they evaluated the accuracy in using kV CBCT for dose calculation using phantom Catphan-600, as well as prostate and lung cases) [Yang *et al.* 2007]. It was also used by Greene *et al.* and Lu *et al.* for their softly and hardly constrained non-rigid registration algorithms, respectively (Section 4.1) [Greene *et al.* 2009, Lu *et al.* 2010, Lu *et al.* 2011]. That said, a more complex information-based similarity measure such as mutual information could be used instead but at the cost of longer computation times.

The segmentation term The second component comprises two (inner/outer) segmentation fidelity terms corresponding to a localized version of the piecewise-constant region-based segmentation model of Chan-Vese [Chan & Vese 2001]. An implicit level set-based representation of the active contour is used, which has several advantages including contour topology preservation (no contour splitting or merging possible). In a level set formulation, a curve C is represented implicitly as the zero-level of a Lipschitz function Φ as follows: $C = \{\mathbf{x} / \Phi(\mathbf{x}) = 0\}$. The registration method proposed in this chapter makes use of the localized version of the region segmentation model of Chan-Vese as follows. Local, rather than global, image statistics are calculated in the moving image, in the inner and outer regions of the neighborhood of all (or, to decrease computation times, a subset of) points along the curve that results from the propagation of the known segmentation in the fixed image using the current estimate of the transformation. In the course of the registration process, the evolving contour is supposed to converge towards the object boundary, and by doing so, the contribution of this segmentation term to the energy is expected to help guide the optimization of the transformation parameters.

Contrary to a segmentation problem where the energy is a function of an unknown function which is the evolving contour (e.g., represented by a level set function), a registration problem seeks to minimize a energy that is a function of the transformation parameters which are variables. It seeks to find an optimal solution for the set of parameters (variables, not functions) that define the transformation. Therefore, the use of the calculus of variations - basically used to optimize a function of a function - is no more required but rather multi-variable calculus as we treat the cost energy as a multi-variable function and not a function of a function. In appearance, in our problem there are two unknowns which are the transformation parameters (variables) on one hand, and the level set function embedding the evolving contour in the moving image on the other one, but in fact, the level set function represents the evolving contour in the moving image which is related to the known object segmentation in the fixed image by the transformation parameters. Therefore, the only unknowns that remain are the transformation parameters. In other words, the partial derivatives of the energy function are derived by performing simple derivatives with respect to the transformation parameters. The energy functional is solved using a registration - not segmentation - framework. In particular, the partial derivatives of the energy functional are not obtained using the calculus of variations as is the case for

pure segmentation problems but rather calculating simple derivatives with respect to the transformation parameters (Section 4.2.1.3).

4.2.1.1 Notations and definitions

Let $I : \Omega \subset \mathbb{R}^3 \rightarrow \mathbb{R}$ and $\hat{I} : \hat{\Omega} \subset \mathbb{R}^3 \rightarrow \mathbb{R}$ denote the fixed image and the moving image, respectively, and let $T : \mathbb{R}^3 \rightarrow \mathbb{R}^3$ be a free-form deformation that maps from the space of the fixed image to the space of the moving image. In this thesis, B-splines are used to model transformation T . We denote by $\hat{\mathbf{x}} := T(\mathbf{x}) \in \hat{\Omega}$ the image of a point $\mathbf{x} \in \Omega$ under T . We denote by $C \subset \Omega$ the boundary of a region of interest (ROI), be it the prostate, the rectum or the bladder, in image I . We wish to find a closed curve $\hat{C} \subset \hat{\Omega}$ that represents the boundary of the corresponding ROI in image \hat{I} . \hat{C} is related to C by $\hat{C} := T(C)$. Our task boils down to simultaneously find the mapping T and the desirable contour \hat{C} in a simultaneous way as T and \hat{C} are used in the expression of the energy, E , to minimize. Yet, T is the only unknown of the problem as \hat{C} is obtained by $\hat{C} = T(C)$. Let $\Phi : \Omega \rightarrow \mathbb{R}$ denote a Lipschitz level set function. Let $C_{in} \subset \Omega$ and $C_{out} \subset \Omega$ be the inner and the outer regions of contour C . Using a level set-based formulation, C , C_{in} and C_{out} are such that:

$$C = \{\mathbf{x} \in \Omega / \Phi(\mathbf{x}) = 0\} \quad (4.7)$$

$$C_{in} = \{\mathbf{x} \in \Omega / \Phi(\mathbf{x}) \leq 0\} \quad (4.8)$$

$$C_{out} = \Omega \setminus C_{in} = \{\mathbf{x} \in \Omega / \Phi(\mathbf{x}) > 0\} \quad (4.9)$$

Similarly, we define \hat{C} , \hat{C}_{in} and \hat{C}_{out} with respect to $\hat{\Phi}$.

The optimization of the cost function, E , is performed using the gradient descent and hence requires the computation of the gradient of E , i.e. the partial derivatives of E with respect to the transform parameters, $\mathbf{P} = (p_1, \dots, p_m)$. For such needs, the knowledge of the transformation Jacobian, J , with respect to the transformation parameters (not to the position coordinates) for all mapped points is necessary. J is a matrix whose elements are the partial derivatives of a mapped point, $\hat{\mathbf{x}} = (\hat{x}, \hat{y}, \hat{z}) \in \hat{I}$, with respect to the transform parameters as follows:

$$J = \frac{\partial \hat{\mathbf{x}}}{\partial \mathbf{P}} \quad (4.10)$$

$$= \begin{pmatrix} \frac{\partial \hat{x}}{\partial p_1} & \dots & \frac{\partial \hat{x}}{\partial p_m} \\ \frac{\partial \hat{y}}{\partial p_1} & \dots & \frac{\partial \hat{y}}{\partial p_m} \\ \frac{\partial \hat{z}}{\partial p_1} & \dots & \frac{\partial \hat{z}}{\partial p_m} \end{pmatrix} \quad (4.11)$$

$$= \begin{pmatrix} \frac{\partial T_x(\mathbf{x})}{\partial p_1} & \dots & \frac{\partial T_x(\mathbf{x})}{\partial p_m} \\ \frac{\partial T_y(\mathbf{x})}{\partial p_1} & \dots & \frac{\partial T_y(\mathbf{x})}{\partial p_m} \\ \frac{\partial T_z(\mathbf{x})}{\partial p_1} & \dots & \frac{\partial T_z(\mathbf{x})}{\partial p_m} \end{pmatrix} \quad (4.12)$$

$$(4.13)$$

It is assumed that the images I and \hat{I} are smooth and compactly supported functions on rectangular domains $\Omega, \hat{\Omega} \subset \mathbb{R}^3$. For all mathematical derivations in Section 4.2.1, a continuous formulation is used. The discret aspect of the data is only found at the implementation stage (Section 4.2.2).

Basic notations

Ω	Fixed image domain
$\hat{\Omega}$	Moving image domain
I	Fixed image
\hat{I}	Moving image
$\mathbf{x} = (x, y, z)$	Spatial coordinates of a point in the fixed image
$\hat{\mathbf{x}} = (\hat{x}, \hat{y}, \hat{z})$	Spatial coordinates of a point in the moving image
$I(\mathbf{x})$	Fixed image intensity at point \mathbf{x}
$\hat{I}(\hat{\mathbf{x}})$	Moving image intensity at point $\hat{\mathbf{x}}$
$T(\mathbf{x}) = \hat{\mathbf{x}}$	Spatial transform referring to the mapping from the space of the fixed image to the space of the moving image
$\mathbf{u} = \hat{\mathbf{x}} - \mathbf{x}$	Displacement field at point \mathbf{x}
C, C_{in}, C_{out}	Boundary, inner and outer regions of an object in I , respectively
N, N_{in}, N_{out}	Numbers of pixels in I, C_{in} and C_{out} , respectively
\hat{C}	Evolving contour in \hat{I}
$\hat{C}_{in}, \hat{C}_{out}$	Inner and outer regions of \hat{C}
$\hat{N}_{in}, \hat{N}_{out}$	Numbers of pixels in \hat{C}_{in} and \hat{C}_{out} , respectively
$\left. \frac{\partial \hat{I}}{\partial \mathbf{x}} \right _{\mathbf{x}+\mathbf{u}}$	Gradient of \hat{I} at mapped point $\mathbf{x} + \mathbf{u}$ (noted as $\text{grad} \hat{I}(\mathbf{x} + \mathbf{u})$)
$\frac{\partial(\mathbf{x}+\mathbf{u})}{\partial p} = \frac{\partial T}{\partial p}$	Jacobian of the transformation at point \mathbf{x} (noted as $j(\mathbf{x})$ in the following)
∇	Gradient of a function f : $\nabla f = \frac{\partial f}{\partial x}(x, y, z) \mathbf{e}_1 + \frac{\partial f}{\partial y}(x, y, z) \mathbf{e}_2 + \frac{\partial f}{\partial z}(x, y, z) \mathbf{e}_3$ where the $\{\mathbf{e}_i\}$, $i \in \{1, 2, 3\}$, are the orthogonal unit vectors pointing in the coordinate directions.
$\mathcal{B}(\mathbf{x} + \mathbf{u}, \mathbf{y} + \mathbf{u})$	Intensity evaluated at point $\mathbf{y} + \mathbf{u}$ ($\mathbf{y} \in \Omega$) in the binary image of a ball ($\mathcal{B} : \hat{\Omega} \rightarrow \mathbb{R}$) of a given radius centered on point $\mathbf{x} + \mathbf{u}$ ($\mathbf{x} \in \Omega$) (intensity values are 1's and 0's in the foreground and background of the ball, respectively)

$\hat{N}_{in_local}(\hat{\mathbf{x}}), \hat{N}_{out_local}(\hat{\mathbf{x}})$ Numbers of pixels in the inner and outer regions of the neighborhood \mathcal{B} of point $\hat{\mathbf{x}}$ along \hat{C} , respectively

Some definitions

Global statistics:

For image I

$$SI = \int_{\Omega} I(\mathbf{x}) \, d\mathbf{x}$$

$$SII = \int_{\Omega} I^2(\mathbf{x}) \, d\mathbf{x}$$

$$N_{in} = \int_{\Omega} H(\Phi(\mathbf{x})) \, d\mathbf{x}$$

$$N_{out} = \int_{\Omega} [1 - H(\Phi(\mathbf{x}))] \, d\mathbf{x}$$

$$N = N_{in} + N_{out}$$

For image \hat{I}

$$S\hat{I} = \int_{\Omega} \hat{I}(\mathbf{x} + \mathbf{u}) \, d\mathbf{x}$$

$$S\hat{I}\hat{I} = \int_{\Omega} \hat{I}^2(\mathbf{x} + \mathbf{u}) \, d\mathbf{x}$$

$$S\hat{I}_{in} = \int_{\Omega} H(\hat{\Phi}(\mathbf{x} + \mathbf{u})) \hat{I}(\mathbf{x} + \mathbf{u}) \, d\mathbf{x}$$

$$S\hat{I}_{out} = \int_{\Omega} [1 - H(\hat{\Phi}(\mathbf{x} + \mathbf{u}))] \hat{I}(\mathbf{x} + \mathbf{u}) \, d\mathbf{x}$$

$$S\hat{I}\hat{I}_{in} = \int_{\Omega} H(\hat{\Phi}(\mathbf{x} + \mathbf{u})) \hat{I}^2(\mathbf{x} + \mathbf{u}) \, d\mathbf{x}$$

$$S\hat{I}\hat{I}_{out} = \int_{\Omega} [1 - H(\hat{\Phi}(\mathbf{x} + \mathbf{u}))] \hat{I}^2(\mathbf{x} + \mathbf{u}) \, d\mathbf{x}$$

$$\hat{N}_{in} = \int_{\Omega} H(\hat{\Phi}(\mathbf{x} + \mathbf{u})) \, d\mathbf{x}$$

$$\hat{N}_{out} = \int_{\Omega} [1 - H(\hat{\Phi}(\mathbf{x} + \mathbf{u}))] \, d\mathbf{x}$$

$$\bar{\hat{I}}_{in} = \frac{S\hat{I}_{in}}{\hat{N}_{in}}$$

$$\bar{\hat{I}}_{out} = \frac{S\hat{I}_{out}}{\hat{N}_{out}}$$

Mixed formula

$$SI\hat{I} = \int_{\Omega} I(\mathbf{x}) \hat{I}(\mathbf{x} + \mathbf{u}) \, d\mathbf{x}$$

Local statistics, for image \hat{I} :

$$S\hat{I}_{in_local}(\mathbf{x} + \mathbf{u}) = \int_{\Omega} \mathcal{B}(\mathbf{x} + \mathbf{u}, \mathbf{y} + \mathbf{u}) H(\hat{\Phi}(\mathbf{y} + \mathbf{u})) \hat{I}(\mathbf{y} + \mathbf{u}) \, d\mathbf{y}$$

$$S\hat{I}_{out_local}(\mathbf{x} + \mathbf{u}) = \int_{\Omega} \mathcal{B}(\mathbf{x} + \mathbf{u}, \mathbf{y} + \mathbf{u}) [1 - H(\hat{\Phi}(\mathbf{y} + \mathbf{u}))] \hat{I}(\mathbf{y} + \mathbf{u}) \, d\mathbf{y}$$

$$S\hat{I}\hat{I}_{in_local}(\mathbf{x} + \mathbf{u}) = \int_{\Omega} \mathcal{B}(\mathbf{x} + \mathbf{u}, \mathbf{y} + \mathbf{u}) H(\hat{\Phi}(\mathbf{y} + \mathbf{u})) \hat{I}^2(\mathbf{y} + \mathbf{u}) \, d\mathbf{y}$$

$$S\hat{I}\hat{I}_{out_local}(\mathbf{x} + \mathbf{u}) = \int_{\Omega} \mathcal{B}(\mathbf{x} + \mathbf{u}, \mathbf{y} + \mathbf{u}) [1 - H(\hat{\Phi}(\mathbf{y} + \mathbf{u}))] \hat{I}^2(\mathbf{y} + \mathbf{u}) \, d\mathbf{y}$$

$$\hat{N}_{in_local}(\mathbf{x} + \mathbf{u}) = \int_{\Omega} \mathcal{B}(\mathbf{x} + \mathbf{u}, \mathbf{y} + \mathbf{u}) H(\hat{\Phi}(\mathbf{y} + \mathbf{u})) \, d\mathbf{y}$$

$$\hat{N}_{out_local}(\mathbf{x} + \mathbf{u}) = \int_{\Omega} \mathcal{B}(\mathbf{x} + \mathbf{u}, \mathbf{y} + \mathbf{u}) [1 - H(\hat{\Phi}(\mathbf{y} + \mathbf{u}))] \, d\mathbf{y}$$

4.2.1.2 Cost function

The total energy E considered in this work is given by a weighted sum of the similarity term, E_{reg} , and the segmentation term, E_{seg} as follows:

$$E(I, \hat{I} \circ T, C) = \lambda E_{reg}(I, \hat{I} \circ T) + \mu E_{seg}(C, T) \quad (4.14)$$

The similarity term is simply the NCC, defined as:

$$E_{reg} = - \frac{\int_{\Omega} (I(\mathbf{x}) - \bar{I}) (\hat{I}(T(\mathbf{x})) - \bar{\hat{I}}) d\mathbf{x}}{\sqrt{\int_{\Omega} (I(\mathbf{x}) - \bar{I})^2 d\mathbf{x} \int_{\Omega} (\hat{I}(T(\mathbf{x})) - \bar{\hat{I}})^2 d\mathbf{x}}} \quad (4.15)$$

Regarding the segmentation term, for sake of simplicity, we will write all the calculations using global statistics, and adapt the final formulas for local statistics. Let E_{seg_global} be the segmentation term using global statistics. Naturally,

$$E_{seg_global} = \int_{\Omega} H(\hat{\Phi}(T(\mathbf{x}))) \hat{F}_{in}(T(\mathbf{x})) d\mathbf{x} + \int_{\Omega} [1 - H(\hat{\Phi}(T(\mathbf{x})))] \hat{F}_{out}(T(\mathbf{x})) d\mathbf{x} \quad (4.16)$$

where \hat{F}_{in} and \hat{F}_{out} are the (global) region descriptors inside and outside contour \hat{C} , respectively. We use the piecewise-constant region-based segmentation model of Chan-Vese, which means:

$$\begin{cases} \hat{F}_{in}(T(\mathbf{x})) &= (\hat{I}(T(\mathbf{x})) - \bar{\hat{I}}_{in})^2 \\ \hat{F}_{out}(T(\mathbf{x})) &= (\hat{I}(T(\mathbf{x})) - \bar{\hat{I}}_{out})^2 \end{cases} \quad (4.17)$$

Given I , \hat{I} and a known contour C of a ROI in I , the total energy can be formulated as a function of only the transformation parameters. For $p \in \{p_1, \dots, p_m\}$, we have:

$$E(p) = - \underbrace{\frac{\int_{\Omega} (I(\mathbf{x}) - \bar{I}) (\hat{I}(\mathbf{x} + \mathbf{u}(\mathbf{x}, p)) - \bar{\hat{I}}) d\mathbf{x}}{\sqrt{\int_{\Omega} (I(\mathbf{x}) - \bar{I})^2 d\mathbf{x} \int_{\Omega} (\hat{I}(\mathbf{x} + \mathbf{u}(\mathbf{x}, p)) - \bar{\hat{I}})^2 d\mathbf{x}}}}_{E_{reg}} \quad (4.18)$$

$$+ \underbrace{\int_{\Omega} H(\hat{\Phi}(\mathbf{x} + \mathbf{u}(\mathbf{x}, p))) \hat{F}_{in}(\mathbf{x} + \mathbf{u}(\mathbf{x}, p)) d\mathbf{x}}_{E_{seg_global_in}} \quad (4.19)$$

$$+ \underbrace{\int_{\Omega} [1 - H(\hat{\Phi}(\mathbf{x} + \mathbf{u}(\mathbf{x}, p)))] \hat{F}_{out}(\mathbf{x} + \mathbf{u}(\mathbf{x}, p)) d\mathbf{x}}_{E_{seg_global_out}} \quad (4.20)$$

In the following, for sake of simplicity, $\mathbf{u}(\mathbf{x}, p)$ will be noted as \mathbf{u} .

$$E_{seg_global_in} = \int_{\Omega} H(\hat{\Phi}(\mathbf{x} + \mathbf{u})) (\hat{I}^2(\mathbf{x} + \mathbf{u}) - 2\bar{\hat{I}}_{in}\hat{I}(\mathbf{x} + \mathbf{u}) + \bar{\hat{I}}_{in}^2) d\mathbf{x} \quad (4.21)$$

$$\begin{aligned} &= \int_{\Omega} H(\hat{\Phi}(\mathbf{x} + \mathbf{u})) \hat{I}^2(\mathbf{x} + \mathbf{u}) d\mathbf{x} - 2\bar{\hat{I}}_{in} \int_{\Omega} H(\hat{\Phi}(\mathbf{x} + \mathbf{u})) \hat{I}(\mathbf{x} + \mathbf{u}) d\mathbf{x} \\ &\quad + \bar{\hat{I}}_{in}^2 \int_{\Omega} H(\hat{\Phi}(\mathbf{x} + \mathbf{u})) d\mathbf{x} \end{aligned} \quad (4.22)$$

Using the notations defined in Section 4.2.1.1, we have:

$$E_{seg_global_in} = S\hat{I}\hat{I}_{in} - \frac{S\hat{I}_{in}^2}{\hat{N}_{in}} \quad (4.23)$$

Similarly,

$$E_{seg_global_out} = S\hat{I}\hat{I}_{out} - \frac{S\hat{I}_{out}^2}{\hat{N}_{out}} \quad (4.24)$$

Taking inspiration from Equation 4.2, we obtain the localized versions of Equations 4.23 and 4.24, respectively:

$$E_{seg_local_in} = \int_{\Omega} \delta\Phi(\mathbf{x} + \mathbf{u}) \left(S\hat{I}\hat{I}_{in_local}(\mathbf{x} + \mathbf{u}) - \frac{S\hat{I}_{in_local}(\mathbf{x} + \mathbf{u})^2}{\hat{N}_{in_local}(\mathbf{x} + \mathbf{u})} \right) d\mathbf{x} \quad (4.25)$$

and

$$E_{seg_local_out} = \int_{\Omega} \delta\Phi(\mathbf{x} + \mathbf{u}) \left(S\hat{I}\hat{I}_{out_local}(\mathbf{x} + \mathbf{u}) - \frac{S\hat{I}_{out_local}(\mathbf{x} + \mathbf{u})^2}{\hat{N}_{out_local}(\mathbf{x} + \mathbf{u})} \right) d\mathbf{x} \quad (4.26)$$

Besides,

$$E_{reg} = - \frac{S\hat{I}\hat{I} - \frac{S\hat{I} \cdot S\hat{I}}{N}}{\sqrt{\left(S\hat{I}\hat{I} - \frac{S\hat{I}^2}{N}\right) \left(S\hat{I}\hat{I} - \frac{S\hat{I}^2}{N}\right)}} \quad (4.27)$$

Details on the calculation of E_{reg} and its derivatives can be found in [Staring 2006].

4.2.1.3 Minimization of the cost function

The minimization of the total energy E is performed using the gradient descent which requires the computation of the gradient of E , i.e. the partial derivatives of E with respect to the transform parameters, p_1, \dots, p_m . For $p \in \{p_1, \dots, p_m\}$,

$$\frac{\partial E}{\partial p} = \lambda \frac{\partial E_{reg}}{\partial p} + \mu \frac{\partial E_{seg}}{\partial p} \quad (4.28)$$

For sake of clarity, all the derivations necessary to obtain the gradient of E are presented in detail in Appendix 5.2.

4.2.1.4 The transformation model: B-splines

The cubic B-spline approximation function is used to represent the FFD. A lattice (also commonly called grid or mesh) of user-defined nodes is overlaid on domain Ω . Each node contains a deformation vector, whose components are determined by optimizing the metric. The node deformations are determined using the gradient descent algorithm. The deformation at any point of the fixed image is calculated by spline interpolation using the closest nodes. B-splines are piecewise defined by polynomial functions, and have the properties of being \mathcal{C}^2 continuous, highly smooth at the places where the polynomial pieces connect (knots), and locally controlled (in other words, they have limited support). The latter means that perturbing the position of one control point only affects the positions of neighboring control points, making the B-spline model particularly useful for describing local deformations and computationally efficient. The degree of freedom of the model depends on the resolution of the control point grid, that is, the spacing between the control points.

We use a uniform control lattice, Φ , defined as an $(l + 3) \times (m + 3) \times (n + 3)$ grid of control points spanning the integer grid in Ω . Let $\phi_{i,j,k}$ be the value of the control point at position i, j, k on grid Φ , for $i \in \{-1, 0, \dots, l + 1\}$, $j \in \{-1, 0, \dots, m + 1\}$ and $k \in \{-1, 0, \dots, n + 1\}$. The parameter domain of the fixed image is defined as

$$\Theta = \{(u, v, w) / 0 \leq u \leq l, 0 \leq v \leq m, 0 \leq w \leq n\}.$$

The B-spline function, f , is defined as:

$$f(x, y, z) = \sum_{k=0}^3 \sum_{l=0}^3 \sum_{m=0}^3 B_k(s) B_l(t) \phi_{(i+k)(j+l)}(z)$$

where i, j, s and t . $0 \leq t < 1$. B_k and B_l are uniform cubic B-spline basis functions defined as: A cubic B-spline is composed of .. polynomial segments

$$\begin{cases} B_0(t) &= \frac{1-t^3}{6} \\ B_1(t) &= \frac{3t^3-6t^2+4}{6} \\ B_2(t) &= \frac{(-3t^3+3t^2+3t+1)}{6} \\ B_3(t) &= \frac{t^3}{6} \end{cases}$$

Their role is to weigh the contribution of each control point to $f(x, y)$ based on its distance to (x, y) .

4.2.2 Implementation

4.2.2.1 Software

In this chapter, contrary to Chapter 3, all the data processing and visualization were performed on a Linux computer with distribution openSUSE 12.3 x86_64, with an Intel Core i7-3930K, 3.20-3.80GHz processor, 12MB cache, 6 cores/12 threads, and 32GB RAM. These specifications enabled us to run more than ten registrations at a time. For the implementation of our DIR algorithm, the following open-source software, based on C++, was used:

- the Insight Toolkit ITK [Ibanez *et al.* 2005] *,
- `elastix` based on the ITK library [Klein *et al.* 2010] †,
- the ITK-based Command Line Image Toolkit `clitk` for the pre-processing of the images, and the integrated image-visualization tool VV [Rit *et al.* 2011] ‡.

The software versions used were ITK 4.5.0, elastix 4.7, CMake 2.8.10.2 and gcc 4.7.2. We developed a new generic metric component based on the above-mentioned energy and integrated it in the registration framework of `elastix`. For the implementation of the metric, we used the existing ITK image classes and followed the ITK coding style. The source code we have implemented and the data we have used are freely available on request in the spirit of reproducible research and open science. The parameter file used to run `elastix` is presented in Appendix 5.2.

4.2.2.2 Algorithm

The algorithm is fully automatic and takes as inputs (1) the planning CT image, (2) the daily CBCT image and (3) the binary image associated with the CT image and corresponding to the organ of interest that we want to segment in the CBCT image in the course of the registration process. Let us remember the direction of the transformation mapping: in ITK, the transformation being optimized is the one mapping from the physical space of

*freely available at www.itk.org

†freely available at <http://elastix.isi.uu.nl/>

‡freely available at www.creatis.insa-lyon.fr/rio/vv

the fixed image into the physical space of the moving image, as illustrated in Figure 4.3 extracted from [Ibanez *et al.* 2005]. At each iteration, the registration algorithm iterates over the pixels of the fixed image and seeks the corresponding pixels in the moving image. Not all the pixels in the moving image find a correspondence with a pixel in the fixed image (“holes” in the moving image) and some pixels in the moving image will have more than one corresponding pixels in the fixed image (“overlaps” in the moving image). In our DIR algorithm, we make use of a known organ segmentation in the CT image, we map it into the physical space of the CBCT image and we calculate local statistics in the neighborhood of each mapped point along the mapped contour. Then to exploit the maximum information from the known segmentation, the CT image is used as the fixed image.

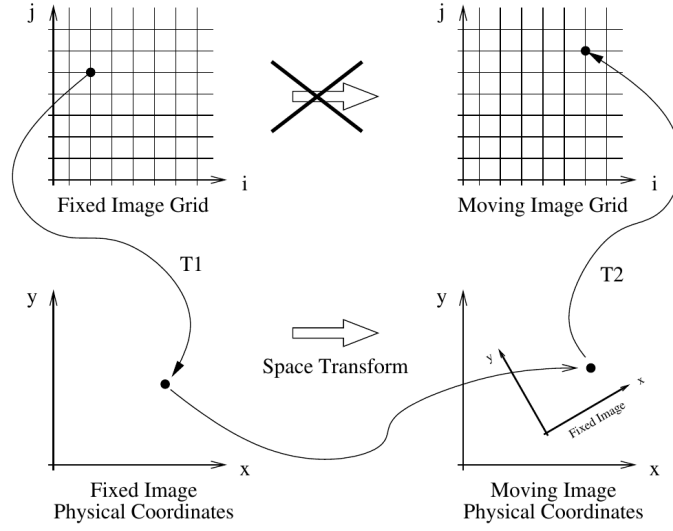


Figure 4.3: Different coordinate systems (the index grid and the physical coordinate system) are involved in the registration process. In the ITK registration framework, the transformation being optimized is the one mapping from the physical space of the fixed image into the physical space of the moving image. (figure extracted from [Ibanez *et al.* 2005])

Our iterative DIR process is as follows.

Loop 1: for each voxel \mathbf{x} in the fixed image I (or in a subset of pixels in I),

1. find the corresponding mapped voxel, $\hat{\mathbf{x}}$, in the moving image \hat{I} by applying the current transformation,
2. update the NCC similarity metric value and derivatives w.r.t. the transformation parameters,
3. if $\hat{\mathbf{x}}$ belongs to the evolving contour \hat{C} ,
 - (a) loop 2: iterate over the neighborhood of $\hat{\mathbf{x}}$ to calculate the local statistics (and their derivatives w.r.t. the transformation parameters) in the inner and outer regions of the neighborhood,
 - (b) update the total segmentation term, that is, the sum of the local inner and outer statistics over all pixels along \hat{C} (and its derivatives w.r.t. the transformation parameters).

4.2.2.3 Parameters

In the experiments, the images were cropped around the organs of interest (prostate, rectum and bladder) before registration in order to reduce computational time. The resolution

of the CT and CBCT images to register were 1 mm x 1 mm x 1 mm. However, to further reduce the algorithm run time, they could be downsampled, e.g., to 4 mm x 4 mm x 4 mm as previously performed in [Greene *et al.* 2009, Lu *et al.* 2010, Lu *et al.* 2011]. The spatial resolution of the B-spline control point grid was 1.0 cm. As a point of comparison, the spacing between control points at the final resolution level was 2.0 cm, 0.8 cm, and 1.0 cm in [Greene *et al.* 2009], [Lu *et al.* 2010] and [Kim *et al.* 2013], respectively.

To speed up our algorithm at run time, we chose to use a subset of pixels in the images to compute the metric (and its derivative) in each iteration instead of all pixels. In fact, based on their experimental results in [Klein *et al.* 2007], the developers of `elastix` advocate the use of a very low number of spatial samples (around 2000), even with large images and transformations with a large number of parameters, for global similarity metrics such as the mutual information or the cross-correlation. Given the non-exclusively global nature of our metric (a combination of a global term, that is, the NCC, and a local statistics-based term), and the lack of time to further investigate the impact of the number of spatial samples on the exactitude of the metric, we wanted to be cautious and keep a high number of spatial samples. We used a ratio of 1 voxel per 100, which amounts, for example, to 104,134 pixels out of 10,413,480 for a $253 \times 245 \times 168$ image. However, we believe that this ratio could be adjusted downwards with further investigation, which would drastically and safely reduce computational time.

To calculate the local statistics at the pixels along the evolving contour, we did not use a ball-shaped neighborhood as in [Lankton & Tannenbaum 2008], but rather a cubic neighborhood.

4.2.3 Dosimetric considerations

The ultimate goal of the estimation of a dense deformation field between the planning CT image and the treatment CBCT image is to estimate the dose that would be delivered to the organs on the day of the treatment, and help the radiation oncologist to make a decision on whether adapting the treatment is necessary. To do so, there are two methodological alternatives/approaches:

- The segmentations of the organs of interest on the treatment CBCT image are needed. Because of time limitations, no manual segmentation on CBCT is scheduled in daily clinical workflow. To obtain an automatic segmentation of the organs on the CBCT image, the dense deformation field is used to propagate the manual segmentations of the organs of interest from the planning CT image to the treatment CBCT image. After applying a setup correction strategy as performed in clinical routine (using RR), the DVHs of the organs of interest from the CBCT image are calculated using the planned dose distribution. According to the shape and parameters of these DVHs, the radiation oncologist can make a reasonably informed decision on adapting or not the treatment plan to account for organ deformation. This procedure is illustrated on Figure 4.4. The corresponding procedure that makes use of manual CBCT segmentations of the organs of interest was presented in Chapter 3, Figure 3.4, with the objective of comparing the DVHs obtained with different setup correction strategies.
- The dense deformation field is used to map the planning CT image and the planned dose distribution onto the treatment CBCT image. Then there are three possibilities. The first one consists of computing the DVHs of the propagated segmentations from the CT to the CBCT using the deformed planned dose distribution. The second one consists of re-calculating the dose distribution on the basis of the deformed CT

image and the planned beam arrangement, and compute the DVHs. And the third one consists of re-optimizing the treatment plan on the basis of the deformed CT image, calculate the new dose distribution and compute the DVHs.

In the Results section (Section 4.3), we will present some dosimetric results for one single fraction following the first approach, depicted in Figure 4.4. However, it must be borne in mind that to make a decision on the need of adapting the treatment, cumulative DVHs must be considered rather than DVHs for one single fraction.

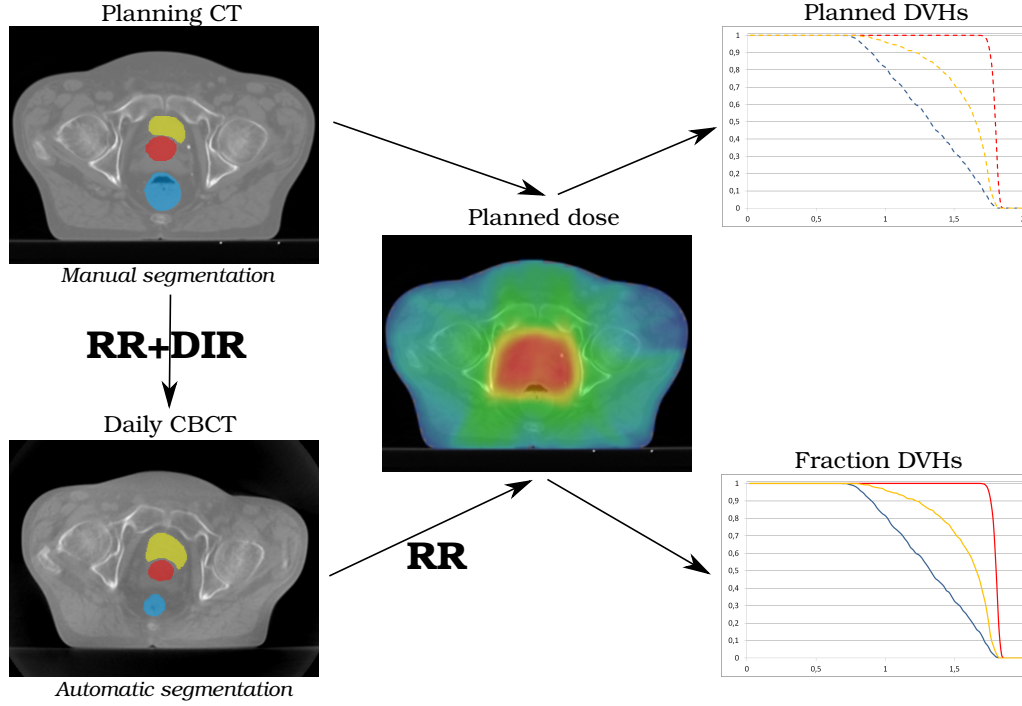


Figure 4.4: The procedure followed to estimate the dose that would be delivered to the organs on the day of the treatment. The deformation field resulting from the “RR+DIR” (which stands for rigid registration + deformable image registration) enables the automatic segmentation of the CBCT image. After rigidly aligning the CBCT image with the planning CT using a setup correction strategy, the DVHs of the segmentations of the organs from the CBCT image are calculated using the planned dose distribution. The DVHs for a given fraction (i.e. using a given treatment-day CBCT) can be compared to the planned DVHs, obtained using the planned dose distribution and the manual CT segmentations, in order to help make a decision on whether adapting the treatment is necessary.

4.3 Results

4.3.1 Preliminary segmentation study based on local statistics

In order to give meaning to the incorporation of the localized version of the region segmentation model of Chan and Vese into our registration framework, we first tested to segment one slice of a selected CBCT image using the code of Lankton *et al.* freely available at <http://www.shawnlankton.com/2008/04/active-contour-matlab-code-demo/> and implemented for 2D images. The prostate, the bladder and the rectum were segmented independently. Several experiments were carried out where the radius of the ball-shaped neighborhood used to calculate the local statistics, as depicted in Figure 4.2, was varied. For all experiments, the number of iterations used was 1500, although in the vast majority of cases, convergence had been reached well in advance. The computation times were about a few minutes for a 289×230 image. It is to be noted that since local region statistics

must be computed for each of the points along the evolving contour, the complexity of the algorithm is higher than methods based on global region statistics. Figures 4.5, 4.6 and 4.7 show the resulting segmentations of the prostate, rectum and bladder, respectively. Each figure is composed of (a) the manual contour drawn manually by the radiation oncologist, (b) the curve that initializes the segmentation process, here a square close to the object to segment, and from (c) on, a series of resulting segmentations obtained with different radii.

We observed that the accuracy of the resulting segmentation highly depended on the radius. The segmentation of the prostate seemed to be less accurate compared to that of the rectum or the bladder. For the prostate, radii ranging from 1 mm to 15 mm appeared to produce similar results, with perhaps a slightly higher accuracy with a 1-mm radius (it was the only case where the evolving contour did not end up adhering completely to the pelvic bones). For radii larger than 20 mm, the resulting contour not only included the prostate, but also captured additional surrounding soft tissue that obviously did not pertain to the prostate. For the rectum, relatively accurate segmentations were obtained for radii ranging from 8 mm to 15 mm. The evolving curve fairly captured the inner wall of the rectum as it successfully separated the highly heterogeneous content of the rectum from the homogeneous intensity rectal wall. The shape was similar to that of the manual contour which was defined in the middle of the rectal wall. For the bladder, for an initialization inside the bladder, the most accurate segmentation was obtained with a 4-mm radius. With smaller radii, the segmenting curve was stuck in local minima and unable to reach the boundary of the bladder, and for larger radii, it spread out of the bladder in order to detect farther, more salient structures. The curve failed in reaching the anterior and posterior ends of the boundary of the bladder. In terms of the speed of convergence, the larger the radius, the faster the curve was evolving with respect to iterations, but also the longer the computational time.

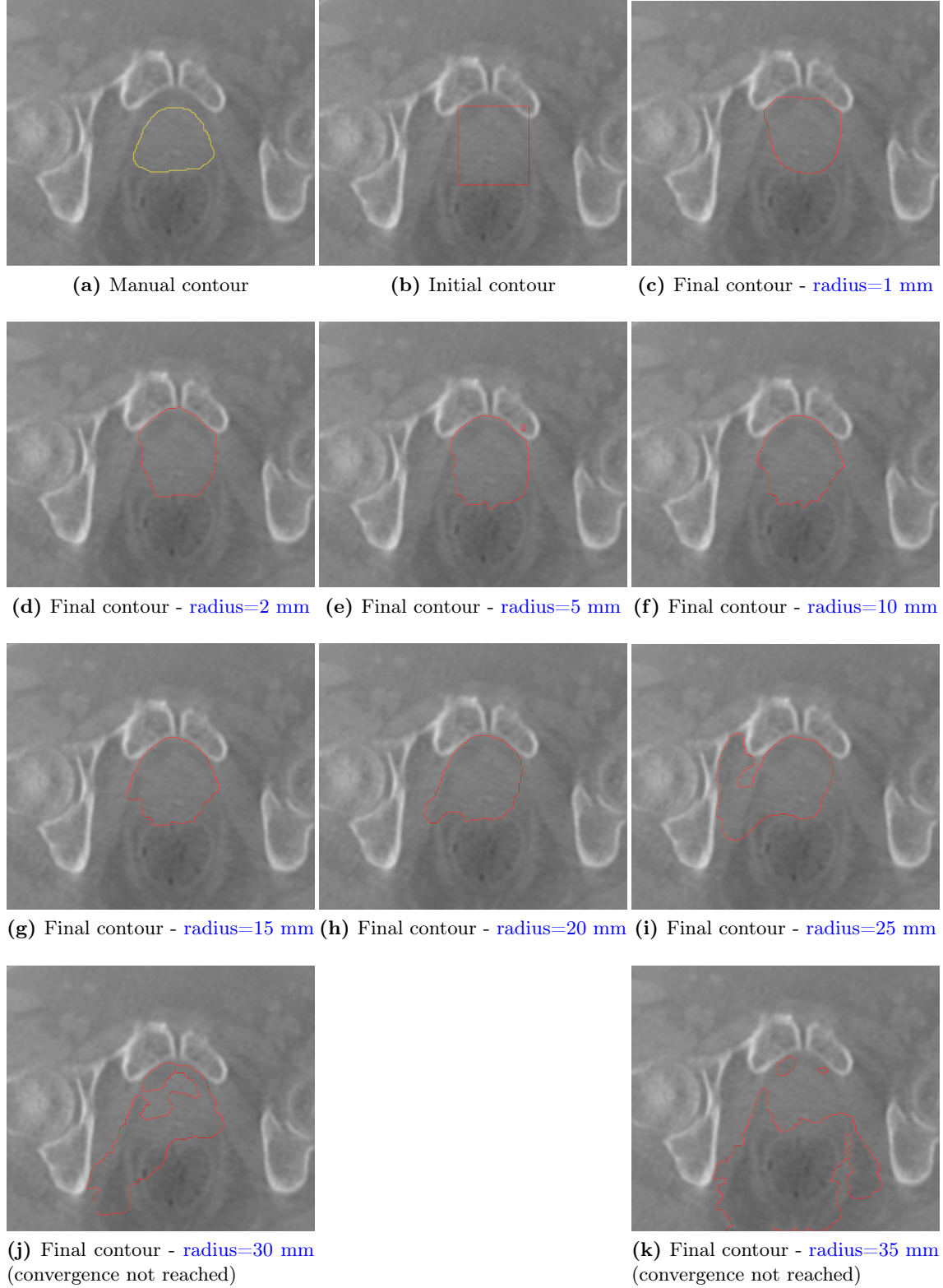


Figure 4.5: Prostate segmentation of a CBCT slice using an adaptation of the region segmentation model of Chan and Vese with local statistics based on local image statistics, as proposed by [Lankton & Tannenbaum 2008]. Figure (a) shows the prostate contour drawn manually (ground truth), Figure (b) shows the initialization and Figures (c)-(k) show the resulting segmentations using different localizing radii.

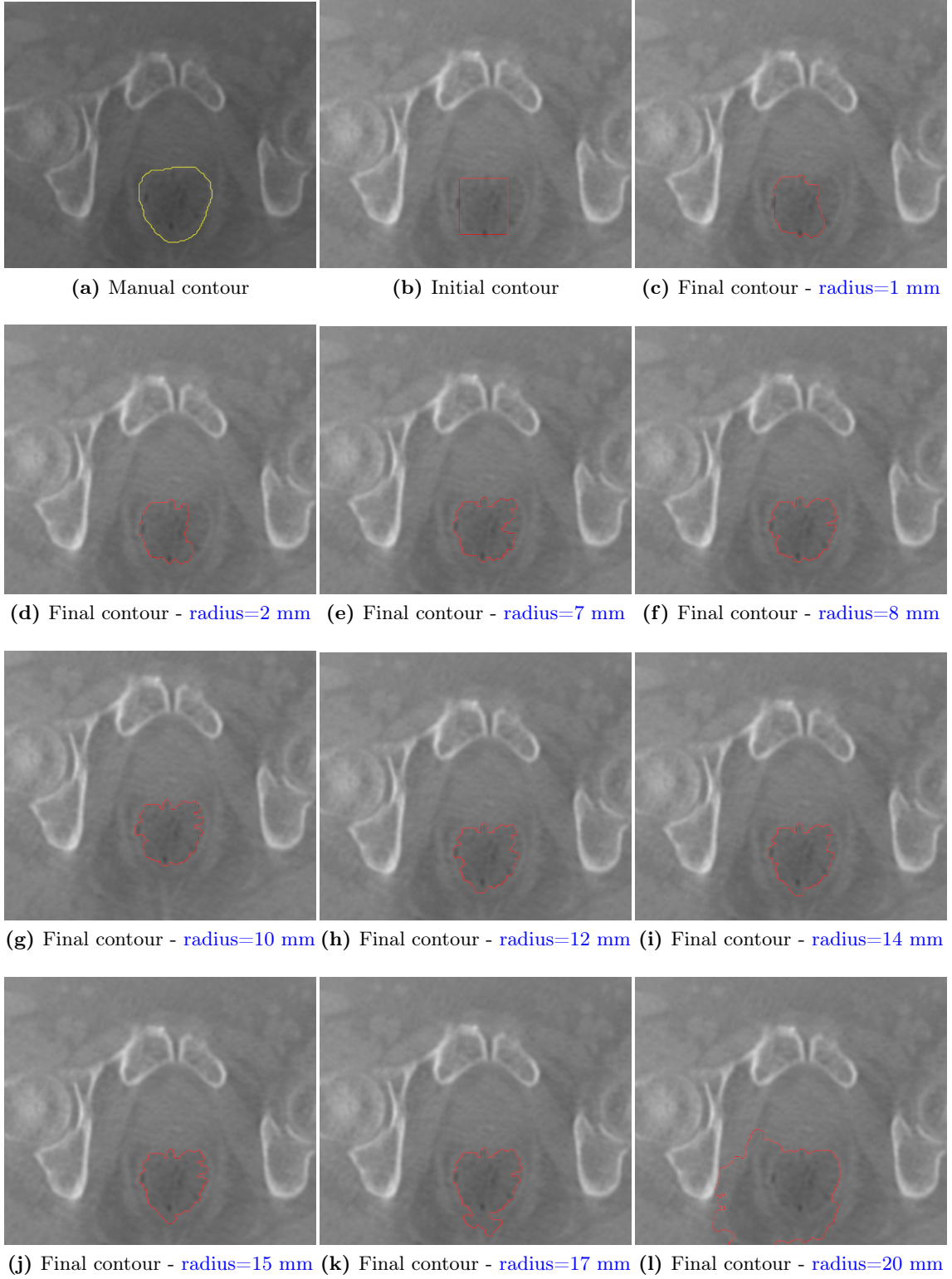


Figure 4.6: Rectum segmentation of a CBCT slice using an adaptation of the region segmentation model of Chan and Vese with local statistics based on local image statistics, as proposed by [Lankton & Tannenbaum 2008]. Figure (a) shows the rectum contour drawn manually, Figure (b) shows the initialization and Figures (c)-(h) show the resulting segmentations using different localizing radii.

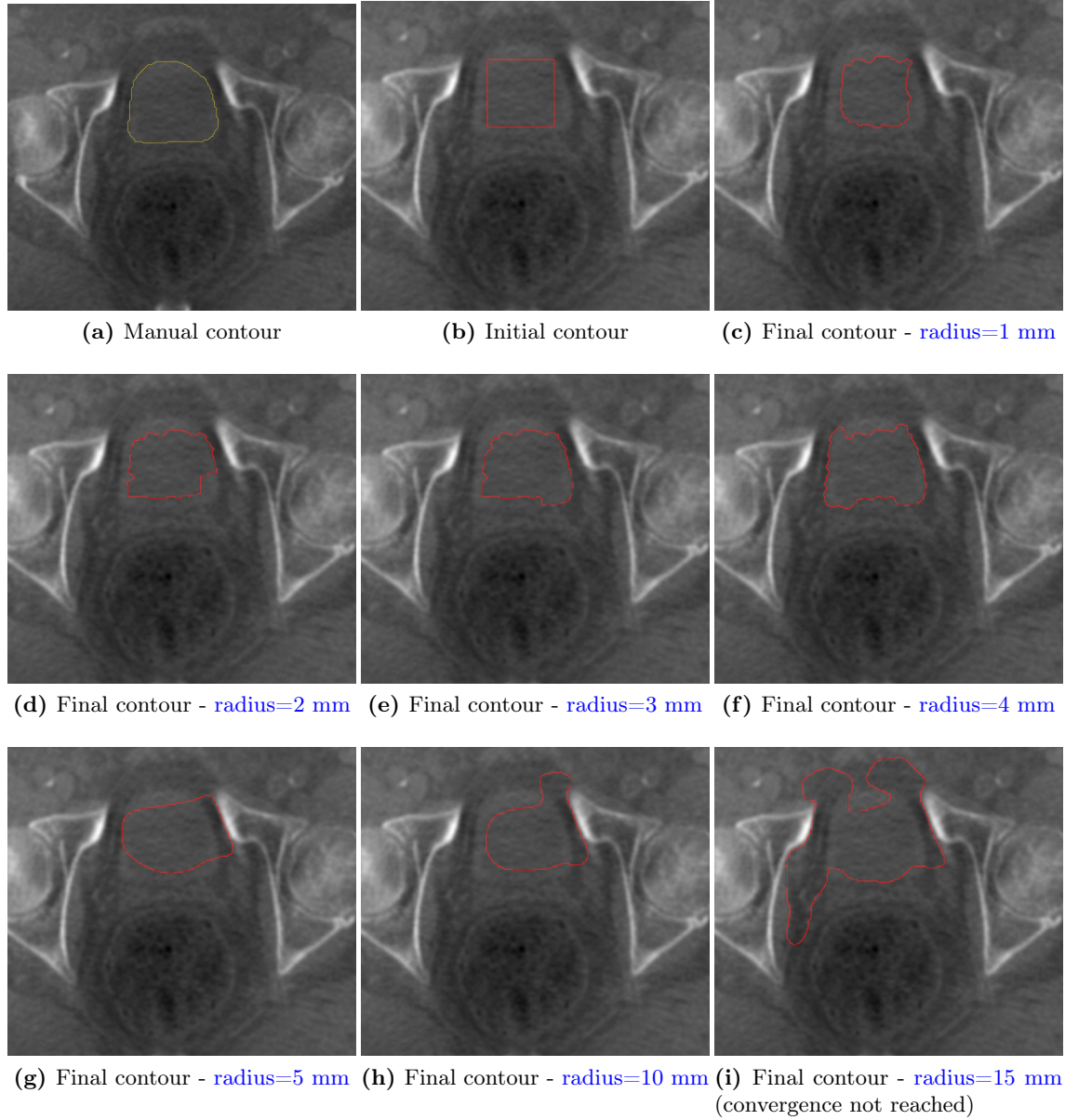


Figure 4.7: Bladder segmentation of a CBCT slice using an adaptation of the region segmentation model of Chan and Vese with local statistics based on local image statistics, as proposed by [Lankton & Tannenbaum 2008]. Figure (a) shows the prostate contour drawn manually, Figure (b) shows the initialization and Figures (c)-(i) show the resulting segmentations using different localizing radii.

4.3.2 The proposed method

We present the potential of this method applied to one patient for which the bony RR resulted into a fairly good localization of the target and a poor localization of the OARs with Dice coefficients of 0.70, 0.46 and 0.59 for the prostate, the rectum and the bladder, respectively. For this patient, who we will refer to as Patient A, we used the same CBCT image as the one that served for the preliminary segmentation study (Section 4.3.1). We will present the results obtained with only one evolving curve. We recall that the curve evolves in the CBCT image domain. We chose to first focus our efforts on the target, that is, the prostate. A fine-tuning of the weights λ and μ from Equation 4.14 yielded $\lambda = 1$ and $\mu = 10^{-10}$. We verified that this couple of parameters lead to a non negligible contribution of the segmentation term to the total energy. Regarding the cubic neighborhood used for

the computation of the local statistics along the evolving curve, we used a radius of 2 mm which seemed to be an acceptable radius according to our preliminary segmentation study (Figure 4.5).

Figure 4.8 shows the curve used for initialization. For the sake of consistency, the same CBCT image slice as the one serving in Section 4.3.1 was inspected. The initial curve corresponded to the automatic CBCT contour obtained after propagation of the manual CT contour using a bony RR. Table 4.1 incorporates the results obtained for these patient and images in terms of the Dice coefficient and the bidirectional distance (BD) for the prostate with (columns 2-5) the RR methods of Chapter 3, (column 6) an ordinary NCC B-spline DIR and (column 7) the proposed method. The Dice coefficient was slightly improved by the proposed method relative to the NCC DIR, but the BD was slightly deteriorated. Both methods achieved a better registration accuracy than the bony RR but did not outperform the 8-mm local RR in terms of the BD. Figure 4.9 illustrates the resulting contours of the prostate in the fixed image domain, that is, the manual CBCT contours of the prostate mapped into the CT image domain using the resulting deformation fields of the NCC DIR and the proposed method, respectively. We observe that on the inspected slice, the two automatic contours are close to the manual segmentation of the prostate but their shape are quite different, proving that the segmentation term of the proposed method has an impact on the registration result. Figure 4.10 depicts the evolution of the NCC throughout the optimization process of the proposed method and the NCC DIR, as well as that of the segmentation terms relative to the inner and outer local statistics throughout the optimization process of the proposed method, respectively. The curves of the global NCC image similarity are decreasing in a fairly similar way (Figure 4.10d). Nevertheless, in the proposed method, the NCC seemed to decrease faster during the earliest dozens of iterations, which lead us to believe that the segmentation terms had a beneficial effect on the registration process. The segmentation terms did also decrease over iterations (except in the last iterations), which is consistent with the fact that the resulting segmentation of the prostate was found to be more accurate than the initial one.



Figure 4.8: Initialization of the evolving contour used for the calculation of the segmentation term of the proposed model superimposed on the same CBCT image slice as that in Figure 4.5. The initialization corresponded to the automatic CBCT contour obtained after propagation of the manual CT prostate contour using a bony RR. Only one evolving contour was involved in the registration process, but in an extended, future version of this model, three evolving contours could be involved simultaneously.

Table 4.1: Results for the prostate after RR and DIR for Patient A.

	Without RR	Manual-contour RR	Bony RR	8-mm local RR	NCC DIR	the proposed method
Dice	0.67	0.83	0.70	0.81	0.81	0.82
BD* (mm)	3.58	1.81	2.91	1.96	2.29	2.44

*BD stands for Bidirectional Distance. It was calculated for each contour comparison by averaging the BLD values over the reference contour.

In the context of IGART, the ultimate goal of CT-to-CBCT DIR is to estimate the dose that would be delivered to the organs on the day of the treatment, and help the radiation oncologist to make a decision on whether adapting the treatment is necessary (see 4.2.3). Figure 4.11 shows the DVHs of the CTV, the rectum and the bladder using the automatic

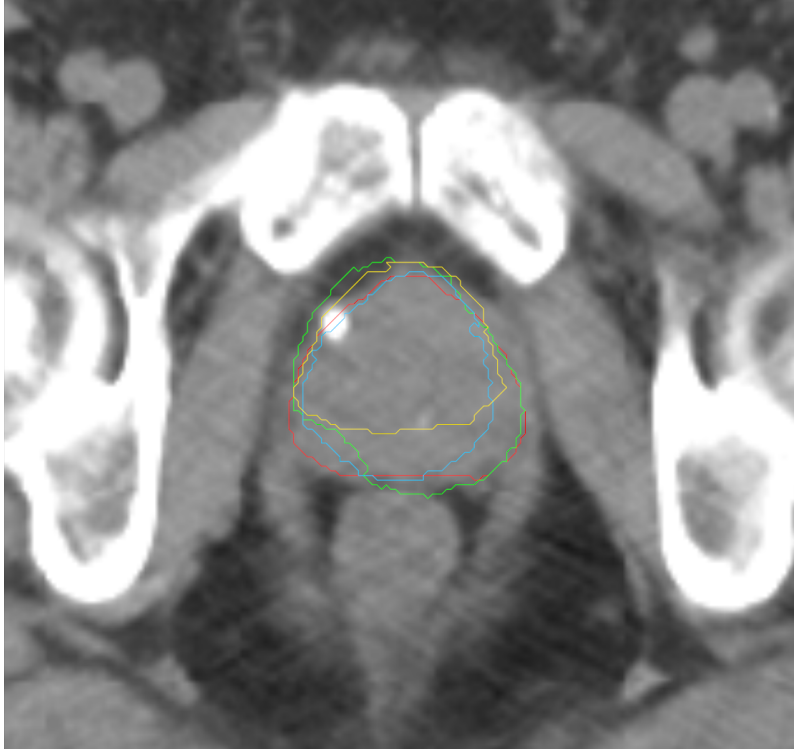
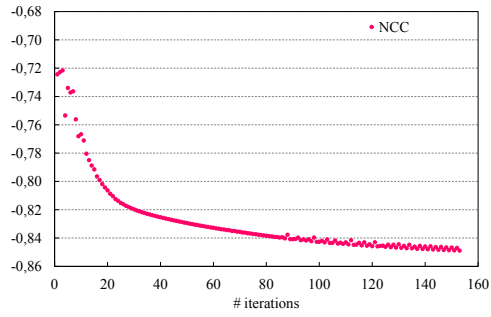
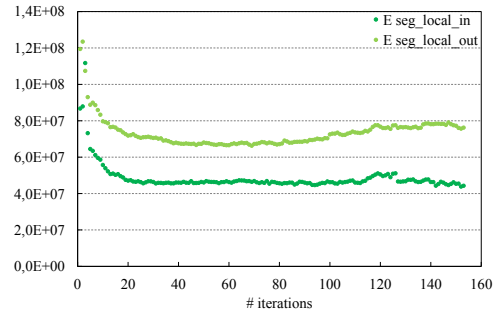


Figure 4.9: Slice of a CT scan with the corresponding prostate contours: (red) the manual contour drawn by the radiation oncologist, (yellow) the automatic contour obtained with a bony RR serving as initialization for the evolving contour of the proposed method, (blue) the automatic contour obtained with an ordinary NCC DIR and (green) the automatic contour obtained with the proposed method using a 2-mm radius. We note that the automatic contours are presented onto the fixed image, that is, the CT image, as the transformation that is optimized by the registration is the one mapping from the fixed image to the moving image.

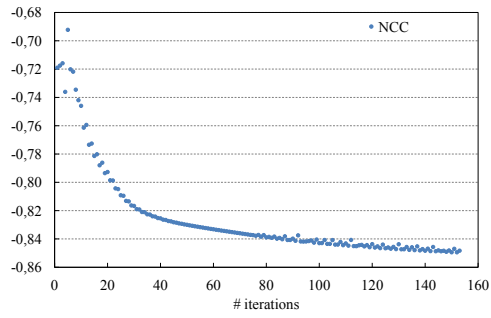
segmentations obtained with the proposed method and the NCC DIR. To compute the DVHs, the procedure presented in Figure 4.4 was followed. One first comment is that given that, in this particular case, the Dice coefficients (for the three organs of interest) obtained with the proposed method and the NCC DIR were close, it was logical to see similar DVHs. Only significant differences in Dice coefficients would produce visible differences in DVHs. This is particularly true for the CTV as the target considered in the dose planning is not the CTV but the PTV ($= \text{CTV} + \text{a treatment margin}$, see Section 1.2.3) to account for geometrical uncertainties occurring during treatment. That said, both methods gave DVHs of the CTV identical to the planned DVH. Regarding the OARs, the DVH of the rectum obtained with the proposed method seemed to correspond to a better avoidance of the rectum compared to the NCC DIR. However, due to poor Dice coefficients regarding the bladder and the rectum for both methods (the proposed method: 0.47 and 0.54, the NCC DIR: 0.48 and 0.54, for the rectum and the bladder, respectively), no clear conclusion could be drawn from the DVHs. We recall that for this example, only one active contour evolving around the prostate was considered in proposed method, which explains why the results concerning the OARs are similar between the proposed method and the NCC DIR.



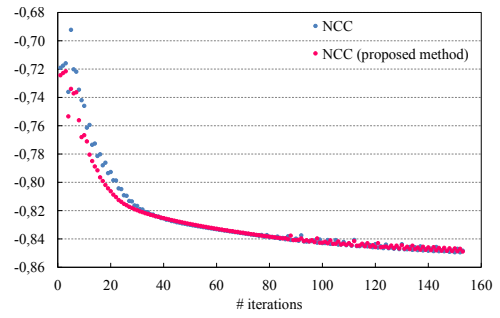
(a) The proposed method



(b) The proposed method

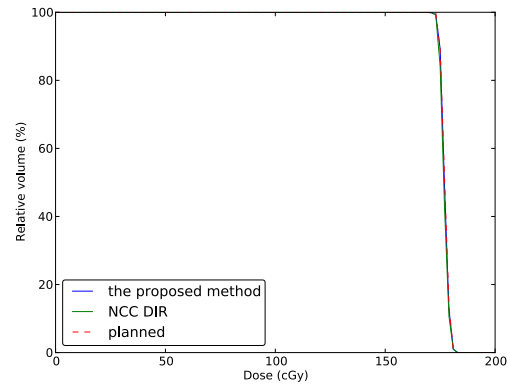


(c) NCC DIR

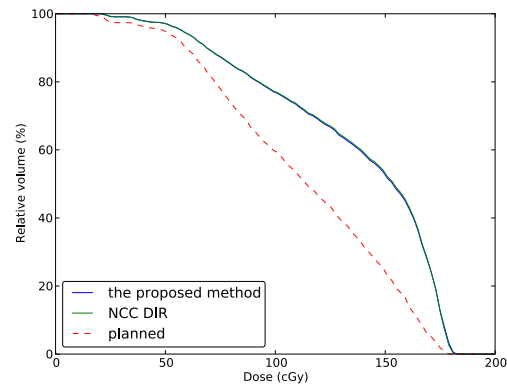


(d) The proposed method and the NCC DIR

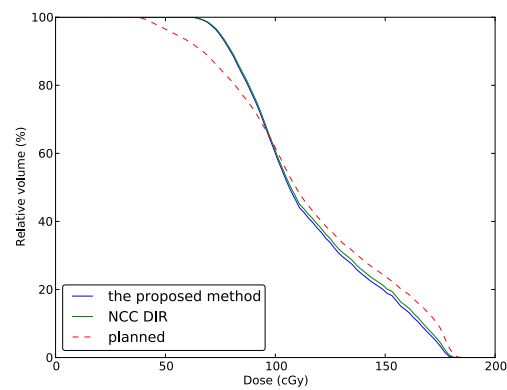
Figure 4.10: Sequence of the values of the different terms constituting the total energy at each iteration during (a)-(b) the optimization process of the proposed method using $\lambda = 1$ and $\mu = 10^{-10}$, and (c) an ordinary NCC DIR. Figure (d) shows the evolution of the NCC throughout the iterative process for the two registrations (simple superimposition of (a) and (c)).



(a) CTV



(b) Rectum



(c) Bladder

Figure 4.11: Comparison of the DVHs of (a) the CTV, (b) the rectum and (c) the bladder using (red dashed line) the manual segmentations and the automatic segmentations obtained with (blue line) the proposed method and (green line) the NCC DIR.

4.4 Conclusion

In this chapter, we consider the organs deformable. In fact, IGART requires an accurate localization of the organs from the treatment-day image to understand whether the initial treatment plan will be/is being/has been delivered properly, and the organs in the pelvis, in particular, the rectum and the bladder, can significantly deform in the course of radiotherapy. Regarding the prostate, we observed in Chapter 3 that RR could fail in allowing for localization, albeit in a very small number of cases. With the aim to improve the localization of the organs compared with RR, this chapter was entirely devoted to the methodological development of a new joint segmentation and deformable registration framework for use in IGART. To deal with the poor contrast-to-noise ratio in CBCT images likely to misguide registration, we have conceived a new metric which included two terms: a global similarity term (the NCC was used, but any other one could be used instead) and a segmentation term based on a localized adaptation of the piecewise-constant region-based model of Chan-Vese using an evolving contour in the CBCT image. The idea was to take advantage of the knowledge of the organ segmentations from the planning CT image, manually delineated by the radiation oncologist for clinical requirements. Our principal aim was to improve the accuracy of the registration compared with an ordinary NCC metric. Our registration algorithm is fully automatic and takes as inputs (1) the planning CT image, (2) the daily CBCT image and (3) the binary image associated with the CT image and corresponding to the organ of interest that we want to segment in the CBCT image in the course of the registration process. We have presented the results for one patient and a contour evolving around the prostate. The results are promising and encourages the continuation of efforts to extend the proposed method and evolve a contour around the rectum or the bladder and investigate its impact on the resulting deformation field. In an extended, future version of our model (the code can be easily modified to fulfil this objective), multiple segmenting contours could evolve simultaneously in the course of the registration process.

Bibliography

- [Carole Le Guyader 2009] Luminita A. Vese Carole Le Guyader. *A Combined Segmentation and Registration Framework with a nonlinear Elasticity Smoother*, 2009. (Cité en page 92.)
- [Chan & Vese 2001] T.F. Chan et L.A. Vese. *Active contours without edges*. vol. 10, no. 2, pages 266–277, 2001. (Cité en pages 89, 90, 91, 92 et 93.)
- [Chen *et al.* 2009] Ting Chen, Sung Kim, Jinghao Zhou, Dimitris Metaxas, Gunaretnam Rajagopal et Ning Yue. *3D meshless prostate segmentation and registration in image guided radiotherapy*. Med Image Comput Comput Assist Interv, vol. 12, no. Pt 1, pages 43–50, 2009. (Cité en page 89.)
- [Greene *et al.* 2009] W. H. Greene, S. Chelikani, K. Purushothaman, J P S. Knisely, Z. Chen, X. Papademetris, L. H. Staib et J. S. Duncan. *Constrained non-rigid registration for use in image-guided adaptive radiotherapy*. Med Image Anal, vol. 13, no. 5, pages 809–817, Oct 2009. (Cité en pages 89, 93 et 101.)
- [Ibanez *et al.* 2005] Luis Ibanez, Will Schroeder, Lydia Ng, Josh Cates et The Insight Software Consortium. *The ITK Software Guide*. Kitware, Inc. ISBN 1-930934-15-7, second édition, 2005. (Cité en pages 13, 59, 99 et 100.)
- [Kim *et al.* 2013] Jinkoo Kim, Sanath Kumar, Chang Liu, Hualiang Zhong, Deepak Pradhan, Mira Shah, Richard Cattaneo, Raphael Yechieli, Jared R Robbins, Mohamed A Elshaikhet *et al.* *A novel approach for establishing benchmark CBCT/CT deformable image registrations in prostate cancer radiotherapy*. Physics in medicine and biology, vol. 58, no. 22, page 8077, 2013. (Cité en pages 89 et 101.)
- [Klein *et al.* 2007] S. Klein, M. Staring et J.P.W. Pluim. *Evaluation of Optimization Methods for Nonrigid Medical Image Registration Using Mutual Information and B-Splines*. vol. 16, no. 12, pages 2879–2890, 2007. (Cité en page 101.)
- [Klein *et al.* 2010] Stefan Klein, Marius Staring, Keelin Murphy, Max A. Viergever et Josien P W. Pluim. *elastix: a toolbox for intensity-based medical image registration*. IEEE Trans Med Imaging, vol. 29, no. 1, pages 196–205, Jan 2010. (Cité en pages 38, 99 et 117.)
- [Lankton & Tannenbaum 2008] Shawn Lankton et Allen Tannenbaum. *Localizing region-based active contours*. IEEE Trans Image Process, vol. 17, no. 11, pages 2029–2039, Nov 2008. (Cité en pages 13, 90, 91, 92, 101, 104, 105 et 106.)
- [Lu *et al.* 2010] Chao Lu, S. Chelikani, X. Papademetris, L. Staib et J. Duncan. *Constrained non-rigid registration using Lagrange multipliers for application in prostate radiotherapy*. In Computer Vision and Pattern Recognition Workshops (CVPRW), 2010 IEEE Computer Society Conference on, pages 133–138, 2010. (Cité en pages 89, 93 et 101.)
- [Lu *et al.* 2011] Chao Lu, Sudhakar Chelikani, Xenophon Papademetris, Jonathan P. Knisely, Michael F. Milosevic, Zhe Chen, David A. Jaffray, Lawrence H. Staib et James S. Duncan. *An integrated approach to segmentation and nonrigid registration for application in image-guided pelvic radiotherapy*. Med Image Anal, vol. 15, no. 5, pages 772–785, Oct 2011. (Cité en pages 89, 93 et 101.)
- [Paquin *et al.* 2009] Dana Paquin, Doron Levy et Lei Xing. *Multiscale registration of planning CT and daily cone beam CT images for adaptive radiation therapy*. Med Phys, vol. 36, no. 1, pages 4–11, Jan 2009. (Cité en page 89.)

- [Rit *et al.* 2011] S. Rit, R. Pinho, V. Delmon, M. Pech, G Bouilhol, J. Schaerer, B. Navalpakkam, J. Vandemeulebroucke, P. Seroul et D. Sarrut. *VV, a 4D slicer*. In Medical Imaging and Computer-Assisted Intervention MICCAI, Fourth International Workshop on Pulmonary Image Analysis, pages 171–175, 2011. (Cité en pages 12, 52 et 99.)
- [Rohlfing 2012] Torsten Rohlfing. *Image similarity and tissue overlaps as surrogates for image registration accuracy: widely used but unreliable*. IEEE Trans Med Imaging, vol. 31, no. 2, pages 153–163, Feb 2012. (Cité en page 89.)
- [Smitsmans *et al.* 2008] Monique H P. Smitsmans, Floris J. Pos, Josien de Bois, Wilma D. Heemsbergen, Jan-Jakob Sonke, Joos V. Lebesque et Marcel van Herk. *The influence of a dietary protocol on cone beam CT-guided radiotherapy for prostate cancer patients*. Int J Radiat Oncol Biol Phys, vol. 71, no. 4, pages 1279–1286, Jul 2008. (Cité en pages 13, 88 et 117.)
- [Staring 2006] M. Staring. *Contributions to the Normalized Correlation and the Mean Squares Metric*. <http://hdl.handle.net/1926/190>, 04 2006. (Cité en page 98.)
- [Thor *et al.* 2011] Maria Thor, Jørgen B B. Petersen, Lise Bentzen, Morten Høyer et Ludvig Paul Muren. *Deformable image registration for contour propagation from CT to cone-beam CT scans in radiotherapy of prostate cancer*. Acta Oncol, vol. 50, no. 6, pages 918–925, Aug 2011. (Cité en page 88.)
- [Unal & Slabaugh 2005] Gozde Unal et Greg Slabaugh. *Coupled PDEs for non-rigid registration and segmentation*. In Computer Vision and Pattern Recognition, 2005. CVPR 2005. IEEE Computer Society Conference on, volume 1, pages 168–175. IEEE, 2005. (Cité en pages 91 et 92.)
- [Yang *et al.* 2007] Yong Yang, Eduard Schreibmann, Tianfang Li, Chuang Wang et Lei Xing. *Evaluation of on-board kV cone beam CT (CBCT)-based dose calculation*. Phys Med Biol, vol. 52, no. 3, pages 685–705, Feb 2007. (Cité en pages 33 et 93.)
- [Yezzi *et al.* 2003] A. Yezzi, L. Zöllei et T. Kapur. *A variational framework for integrating segmentation and registration through active contours*. Med Image Anal, vol. 7, no. 2, pages 171–185, Jun 2003. (Cité en pages 91 et 92.)

Conclusions and perspectives

In the workflow of a radiation therapy, the last step is to ensure the maximum possible geometric precision and accuracy for the radiation delivery. For that purpose, two complementary image-guided approaches are considered. The first approach (IGRT) is to verify the positioning of the patient on the treatment table right before the beam delivery using image guidance, and if necessary to improve the alignment of the patient to the position used during planning, and hence the position of the target with respect to the system coordinates of the treatment machine. The adjustment/correction of the position of the patient is achieved by a displacement of the treatment table which allows a maximum of 6 degrees of freedom, that is, 3 translations and 3 rotations. Thus, in this approach, a RR between the planning CT image and the treatment CBCT image is required in order to find the displacements to apply to the treatment table. The second approach (IGART), which is to be adopted after the first one, consists in determining whether the anatomy of the treatment day needs an adaptation of the dose plan. It requires a CT-to-CBCT DIR. The resulting deformation field could be used to automatically segment the organs from the treatment image by propagating the manual segmentations from the CT image, allowing to estimate the dosimetric effect of the initial plan on the treatment-day anatomy. The final goal is to enable the radiation oncologist to make a reasonably informed decision on updating or not the dose plan to account for organ deformation.

In this two-fold context, the main goal of the thesis was to provide methodological contributions for automatic intra-patient image registration between the planning CT image and the treatment CBCT image for prostate cancer. The challenge The prostate organe rigide donc OK

5.1 Contributions

In the very beginning of the thesis, a number of efforts were made to harmonize our clinical dataset. All the CT and CBCT images were associated with the segmentations of the prostate, rectum and bladder which the radiation oncologist had manually delineated with a great deal of care. The fact that the CT and CBCT images did not have the same slice thickness and that not all slices were not delineated purposely for sake of time prompted us to implement an interpolation algorithm dedicated to binary images (Chapter 2). We needed to be able to (1) downsample the binary images associated with the CT images and made of continuously delineated slices, and (2) interpolate those associated with the CBCT images and made of sparsely and equally spaced delineated slices, amounting to estimate the missing contours. For that purpose, we used the shape-based interpolation

method of Raya and Udupa [Raya & Udupa 1990] as such for case (1), and with a couple of additional essential steps for case (2) allowing to return to the same configuration as case (1). The difficulty lied in case (2) and it is now possible to estimate the missing contours in a set of sparsely and equally spaced delineated slices. The source code is available at the Insight Journal [Boydev *et al.* 2012] and the dataset is available on request.

Then the thesis was naturally divided into two parts of equal importance.

The first part (Chapter 3) was dedicated to IGRT, and more particularly, to the development of a CBCT-based prostate setup correction strategy using CT-to-CBCT RR. We have established a comparison between different RR algorithms: (a) global RR, (b) bony RR, and (c) bony RR refined by a local RR using the prostate CTV in the CT image expanded with 1-to-20-mm varying margins. A comprehensive statistical analysis of the quantitative and qualitative results was carried out using the whole dataset. We have shown that in a great majority of cases, the bony CT-to-CBCT RR performed fairly well in the pelvis but was outperformed by our proposed 8-mm local RR. In fact, this finding adds evidence to the common hypothesis that the prostate gland behaves as a rigid body [van Herk *et al.* 1995] and that the deformation of the prostate during the course of radiotherapy is small compared to the organ motion [Deurloo *et al.* 2005]. The bony RR algorithm proved to be a good candidate to localize the prostate in the CBCT image but relying only on the bony structure of the pelvis to guide the registration could be delusive in cases where the prostate moves relative to the bones. We showed that in these cases, an 8-mm local RR was beneficial. Besides, we have successfully identified the reasons why the 8-mm local RR could fail in outperforming the bony RR. This happened in a very small number of cases where the difference in the rectum anatomy (or intensity appearance of the rectum) in the vicinity of the prostate between the CT and the CBCT was found to be larger than a certain threshold. To quantify this threshold, we have defined a novel practical method to automatically estimate rectal distension occurred in the vicinity of the prostate between the CT and the CBCT images. It makes use of the manual CT contours only and requires calculations of mean intensities in the prostate and in the portion of the rectum included in the registration mask in both images after bony RR. Using our measure of rectal distension, we have evaluated the impact of rectal distension on the quality of local RR and we have provided a way to predict registration failure. On this basis, we have devised recommendations for clinical practice for the use of automatic RR for prostate localization on CBCT scans. We suggest starting with a bony RR, and refining it by means of an 8-mm local RR if the difference in the rectum anatomy is limited.

The above-mentioned setup correction strategy using CT-to-CBCT RR allows accounting for the (rigid) motion of the target but not for organ deformations. In particular, the rectum and the bladder can significantly deform in the course of radiotherapy, bringing the need for adaptive radiotherapy. IGART requires an accurate localization of the organs from the treatment-day image to understand whether the initial treatment plan will be/is being/has been delivered properly. Chapter 4 was entirely devoted to the methodological development of a new joint segmentation and deformable registration framework for use in IGART. To deal with the poor contrast-to-noise ratio in CBCT images likely to misguide registration, we have conceived a new metric which included two terms: a global similarity term (the NCC was used, but any other one could be used instead) and a segmentation term based on a localized adaptation of the piecewise-constant region-based model of Chan-Vese using an evolving contour in the CBCT image. The idea was to take advantage of the knowledge of the organ segmentations from the planning CT image, manually delineated by the radiation oncologist for clinical requirements. Our principal aim was to improve

the accuracy of the registration compared with an ordinary NCC metric. Our registration algorithm is fully automatic and takes as inputs (1) the planning CT image, (2) the daily CBCT image and (3) the binary image associated with the CT image and corresponding to the organ of interest that we want to segment in the CBCT image in the course of the registration process. We have presented the results for one patient and a contour evolving around the prostate. The results are promising and encourages the continuation of efforts to evolve a contour around the rectum or the bladder and investigate its impact on the resulting deformation field. Our source code, that is, a new generic metric component integrated in the registration framework of `elastix`, an ITK-based software for image registration [Klein *et al.* 2010], is available on request in the spirit of reproducible research and open science.

5.2 Perspectives

Surprisingly enough, our study on prostate localization in CBCT images using RR yielded particularly accurate results in terms of Dice coefficients and BD values between the automatic and the manual segmentations of the prostate (Chapter 3). We classified very few cases out of 115 as failed registrations: 8, 6 and 3 with bony RR, our proposed strategy (i.e. bony RR followed by 8-mm local RR) and our proposed strategy after replacing air in rectum by soft tissue in the images, respectively. Indeed, on this basis, it was an ambitious goal to improve the accuracy of the localization of the prostate in CBCT images using DIR. We selected a case for which the localization of the prostate was fairly good (Dice 0.70) using bony RR. The Dice was increased up to 0.81 using our proposed setup correction strategy (i.e. bony RR followed by 8-mm local RR), also 0.81 using an ordinary NCC B-spline DIR and 0.82 using our proposed DIR algorithm. However, the localization of the organs at risk (rectum and rectum) remained poor and was not improved by any of the DIR algorithms tested. There is hope that using our proposed DIR method with a contour evolving around the rectum or the bladder improves the deformation field there. To go even further, one could consider involving simultaneously as many evolving contours as there are organs of interest in the image. In terms of the implementation, the code is easily extendable for that.

Interestingly, the proposed DIR method can be generalized to any other anatomical location, provided that the segmentation of one or more organs are given in the fixed image. In the context of IGART, as explored in this thesis, the fixed image would be the planning CT image, and hence the segmentations of all the organs of interest (target and OAR) would be available.

As said earlier in the thesis, pelvic CT-to-CBCT DIR is challenging due to a poor contrast-to-noise ratio in the CBCT image. Any DIR method would inevitably entail errors. A natural and legitimate reflex is to try and improve upon the DIR algorithm by exploiting and integrating as much a priori information as possible in order to reduce registration errors. Indeed, that is precisely what we do in our proposed DIR method where we use the known manual segmentations of the organs of interest from the planning CT image to guide the registration process. However, other valuable approaches that aim to reduce registration errors are worth attention. For example, improving the image quality of the CBCT images will be beneficial for registration [Jin *et al.* 2010, Mail *et al.* 2009]. Also a dietary protocol received by the patient to achieve empty rectum and full bladder before the planning CT image and during treatment was shown to have a positive influence on the performance of RR [Smitsmans *et al.* 2008]. We believe that such a protocol, applied in a strict way so that the rectum and the bladder look similar from one day to another,

will also have a great influence on the performance of DIR. Another approach would be to use another imaging modality with higher soft-tissue contrast such as MRI. In fact, recent MR-guided radiation therapy systems have been developed to facilitate real-time prostate localization during treatment time (<http://www.viewray.com/system>).

Bibliography

- [Boydev *et al.* 2012] C. Boydev, D. Pasquier, F. Derraz, L. Peyrodie, A. Taleb-Ahmed et J. Thiran. *Shape-based Interpolation of a Set of 2D Slices*. 10 2012. (Cité en pages 38, 48 et 116.)
- [Deurloo *et al.* 2005] Kirsten E I. Deurloo, Roel J H M. Steenbakkers, Lambert J. Zijp, Josien A. de Bois, Peter J C M. Nowak, Coen R N. Rasch et Marcel van Herk. *Quantification of shape variation of prostate and seminal vesicles during external beam radiotherapy*. *Int J Radiat Oncol Biol Phys*, vol. 61, no. 1, pages 228–238, Jan 2005. (Cité en pages 56 et 116.)
- [Jin *et al.* 2010] Jian-Yue Jin, Lei Ren, Qiang Liu, Jinkoo Kim, Ning Wen, Huaqun Guan, Benjamin Movsas et Indrin J. Chetty. *Combining scatter reduction and correction to improve image quality in cone-beam computed tomography (CBCT)*. *Medical Physics*, vol. 37, no. 11, 2010. (Cité en page 117.)
- [Klein *et al.* 2010] Stefan Klein, Marius Staring, Keelin Murphy, Max A. Viergever et Josien P W. Pluim. *elastix: a toolbox for intensity-based medical image registration*. *IEEE Trans Med Imaging*, vol. 29, no. 1, pages 196–205, Jan 2010. (Cité en pages 38, 99 et 117.)
- [Mail *et al.* 2009] N. Mail, D. J. Moseley, J. H. Siewerdsen et D. A. Jaffray. *The influence of bowtie filtration on cone-beam CT image quality*. *Medical Physics*, vol. 36, no. 1, 2009. (Cité en page 117.)
- [Raya & Udupa 1990] S. P. Raya et J. K. Udupa. *Shape-based interpolation of multidimensional objects*. *IEEE Trans Med Imaging*, vol. 9, no. 1, pages 32–42, 1990. (Cité en pages 38, 48, 49 et 116.)
- [Smitsmans *et al.* 2008] Monique H P. Smitsmans, Floris J. Pos, Josien de Bois, Wilma D. Heemsbergen, Jan-Jakob Sonke, Joos V. Lebesque et Marcel van Herk. *The influence of a dietary protocol on cone beam CT-guided radiotherapy for prostate cancer patients*. *Int J Radiat Oncol Biol Phys*, vol. 71, no. 4, pages 1279–1286, Jul 2008. (Cité en pages 13, 88 et 117.)
- [van Herk *et al.* 1995] M. van Herk, A. Bruce, A. P. Kroes, T. Shouman, A. Touw et J. V. Lebesque. *Quantification of organ motion during conformal radiotherapy of the prostate by three dimensional image registration*. *Int J Radiat Oncol Biol Phys*, vol. 33, no. 5, pages 1311–1320, Dec 1995. (Cité en pages 56, 63, 78, 79 et 116.)

Appendices

Appendix 1: elastix parameter file

```
// Parameter file for the proposed B-spline registration using a new generic metric based
// on a normalized cross-correlation similarity term and a segmentation term that uses
// local statistics in the neighborhood of points along an evolving curve.

// C-style comments: //

// The internal pixel type, used for internal computations
// Leave to float in general.
// NB: this is not the type of the input images! The pixel
// type of the input images is automatically read from the
// images themselves.
// This setting can be changed to "short" to save some memory
// in case of very large 3D images.
(FixedInternalImagePixelType "float")
(MovingInternalImagePixelType "float")

// The dimensions of the fixed and moving image
// Up to elastix 4.5 this had to be specified by the user.
// From elastix 4.6, this is not necessary anymore.
//(FixedImageDimension 2)
//(MovingImageDimension 2)

// Specify whether you want to take into account the so-called
// direction cosines of the images. Recommended: true.
// In some cases, the direction cosines of the image are corrupt,
// due to image format conversions for example. In that case, you
// may want to set this option to "false".
(UseDirectionCosines "true")

// ***** Main Components *****

// The following components should usually be left as they are:
(Registration "MultiResolutionRegistration")
(Interpolator "BSplineInterpolator")
(ResampleInterpolator "FinalBSplineInterpolator")
(Resampler "DefaultResampler")
```

```
// These may be changed to Fixed/MovingSmoothingImagePyramid.
// See the manual.
(FixedImagePyramid "FixedRecursiveImagePyramid")
(MovingImagePyramid "MovingRecursiveImagePyramid")

// The following components are most important:
// The optimizer AdaptiveStochasticGradientDescent (ASGD) works
// quite ok in general. The Transform and Metric are important
// and need to be chosen careful for each application. See manual.
(Optimizer "AdaptiveStochasticGradientDescent")
//(Optimizer "QuasiNewtonLBFGS")
(Transform "BSplineTransform")
//(Metric "AdvancedMattesMutualInformation")
(Metric "NormalizedCorrelationWithActiveContours")

// ***** Transformation *****

// The control point spacing of the bspline transformation in
// the finest resolution level. Can be specified for each
// dimension differently. Unit: mm.
// The lower this value, the more flexible the deformation.
// Low values may improve the accuracy, but may also cause
// unrealistic deformations. This is a very important setting!
// We recommend tuning it for every specific application. It is
// difficult to come up with a good 'default' value.
(FinalGridSpacingInPhysicalUnits 10)

// Alternatively, the grid spacing can be specified in voxel units.
// To do that, uncomment the following line and comment/remove
// the FinalGridSpacingInPhysicalUnits definition.
//(FinalGridSpacingInVoxels 16)

// By default the grid spacing is halved after every resolution,
// such that the final grid spacing is obtained in the last
// resolution level. You can also specify your own schedule,
// if you uncomment the following line:
//(GridSpacingSchedule 4.0 4.0 2.0 1.0)
// This setting can also be supplied per dimension.

// Whether transforms are combined by composition or by addition.
// In generally, Compose is the best option in most cases.
// It does not influence the results very much.
(HowToCombineTransforms "Compose")

// ***** Similarity measure *****

// Number of grey level bins in each resolution level,
// for the mutual information. 16 or 32 usually works fine.
// You could also employ a hierarchical strategy:
//(NumberOfHistogramBins 16 32 64)
```


(NumberOfHistogramBins 32)

```
// If you use a mask, this option is important.
// If the mask serves as region of interest, set it to false.
// If the mask indicates which pixels are valid, then set it to true.
// If you do not use a mask, the option doesn't matter.
```

(ErodeMask "false")

```
// ***** Multiresolution *****
```

```
// The number of resolutions. 1 Is only enough if the expected
// deformations are small. 3 or 4 mostly works fine. For large
// images and large deformations, 5 or 6 may even be useful.
```

(NumberOfResolutions 1)

```
// The downsampling/blurring factors for the image pyramids.
// By default, the images are downsampled by a factor of 2
// compared to the next resolution.
```

```
// So, in 2D, with 4 resolutions, the following schedule is used:
```

```
//(ImagePyramidSchedule 8 8 4 4 2 2 1 1 )
```

```
// And in 3D:
```

```
//(ImagePyramidSchedule 8 8 8 4 4 4 2 2 1 1 1 )
```

```
// You can specify any schedule, for example:
```

```
//(ImagePyramidSchedule 4 4 4 3 2 1 1 1 )
```

```
// Make sure that the number of elements equals the number
// of resolutions times the image dimension.
```

```
// ***** Optimizer *****
```

```
// Maximum number of iterations in each resolution level:
```

```
// 200-2000 works usually fine for nonrigid registration.
```

```
// The more, the better, but the longer computation time.
```

```
// This is an important parameter!
```

(MaximumNumberOfIterations 151)

```
// The step size of the optimizer, in mm. By default the voxel size is used.
```

```
// which usually works well. In case of unusual high-resolution images
```

```
// (eg histology) it is necessary to increase this value a bit, to the size
```

```
// of the "smallest visible structure" in the image:
```

```
//(MaximumStepLength 1.0)
```

```
// ***** Image sampling *****
```

```
// Number of spatial samples used to compute the mutual
// information (and its derivative) in each iteration.
```

```
// With an AdaptiveStochasticGradientDescent optimizer,
// in combination with the two options below, around 2000
// samples may already suffice.
```

```
//(NumberOfSpatialSamples 4096)
```

```
// Refresh these spatial samples in every iteration, and select
```

```
// them randomly. See the manual for information on other sampling
// strategies.
(NewSamplesEveryIteration "true")
(ImageSampler "Random")

// ***** Interpolation and Resampling *****

// Order of B-Spline interpolation used during registration/optimisation.
// It may improve accuracy if you set this to 3. Never use 0.
// An order of 1 gives linear interpolation. This is in most
// applications a good choice.
(BSplineInterpolationOrder 1)

// Order of B-Spline interpolation used for applying the final
// deformation.
// 3 gives good accuracy; recommended in most cases.
// 1 gives worse accuracy (linear interpolation)
// 0 gives worst accuracy, but is appropriate for binary images
// (masks, segmentations); equivalent to nearest neighbor interpolation.
(FinalBSplineInterpolationOrder 3)

//Default pixel value for pixels that come from outside the picture:
(DefaultPixelValue -1000)

// Choose whether to generate the deformed moving image.
// You can save some time by setting this to false, if you are
// not interested in the final deformed moving image, but only
// want to analyze the deformation field for example.
(WriteResultImage "true")

// The pixel type and format of the resulting deformed moving image
(ResultImagePixelType "short")
(ResultImageFormat "mhd")
```

Appendix 2: Minimization of the cost function of the proposed DIR method

The minimization of the total energy E is performed using the gradient descent which requires the computation of the gradient of E , i.e. the partial derivatives of E with respect to the transform parameters, p_1, \dots, p_m . For $p \in \{p_1, \dots, p_m\}$,

$$\frac{\partial E}{\partial p} = \lambda \frac{\partial E_{reg}}{\partial p} + \mu \frac{\partial E_{seg}}{\partial p} \quad (1)$$

Derivative of the similarity term E_{reg} We define $E_{reg} = \frac{A}{B}$ with A the numerator and B the denominator of Equation 4.27. By taking the first variation of A and B with respect to p , we have:

$$\frac{\partial A}{\partial p} = \frac{\partial A}{\partial \hat{I}} \underbrace{\left. \frac{\partial \hat{I}}{\partial \mathbf{x}} \right|_{\mathbf{x}+\mathbf{u}}}_{\text{grad} \hat{I}(\mathbf{x}+\mathbf{u})(\mathbf{x}+\mathbf{u})} \underbrace{\frac{\partial (\mathbf{x} + \mathbf{u})}{\partial p}}_{\frac{\partial T(\mathbf{x})}{\partial p} = j(\mathbf{x})} \quad (2)$$

$$= \int_{\Omega} I(\mathbf{x}) \text{grad} \hat{I}(\mathbf{x} + \mathbf{u}) j(\mathbf{x}) \, d\mathbf{x} - \frac{SI}{N} \int_{\Omega} \text{grad} \hat{I}(\mathbf{x} + \mathbf{u}) j(\mathbf{x}) \, d\mathbf{x} \quad (3)$$

and

$$\frac{\partial B}{\partial p} = \left(SII - \frac{SI^2}{N} \right) \left(\int_{\Omega} \hat{I}(\mathbf{x} + \mathbf{u}) \text{grad} \hat{I}(\mathbf{x} + \mathbf{u}) j(\mathbf{x}) \, d\mathbf{x} - \frac{S\hat{I}}{N} \int_{\Omega} \text{grad} \hat{I}(\mathbf{x} + \mathbf{u}) j(\mathbf{x}) \, d\mathbf{x} \right) \quad (4)$$

Given that $\frac{\partial E_{reg}}{\partial p} = \frac{B \frac{\partial A}{\partial p} - A \frac{\partial B}{\partial p}}{B^2}$, we obtain by substitution:

For $p \in \{p_1, \dots, p_m\}$,

$$\frac{\partial E_{reg}}{\partial p} = \frac{1}{\sqrt{\left(SII - \frac{SI^2}{N}\right) \left(S\hat{I}\hat{I} - \frac{S\hat{I}^2}{N}\right)}} \left[\int_{\Omega} I(\mathbf{x}) \text{grad} \hat{I}(\mathbf{x} + \mathbf{u}) j(\mathbf{x}) d\mathbf{x} \right. \quad (5)$$

$$\left. - \frac{SI}{N} \int_{\Omega} \text{grad} \hat{I}(\mathbf{x} + \mathbf{u}) j(\mathbf{x}) d\mathbf{x} \right. \quad (6)$$

$$\left. - \frac{S\hat{I}\hat{I} - \frac{SI \cdot S\hat{I}}{N}}{S\hat{I}\hat{I} - \frac{S\hat{I}^2}{N}} \left(\int_{\Omega} \hat{I}(\mathbf{x} + \mathbf{u}) \text{grad} \hat{I}(\mathbf{x} + \mathbf{u}) j(\mathbf{x}) d\mathbf{x} \right. \right. \quad (7)$$

$$\left. \left. - \frac{S\hat{I}}{N} \int_{\Omega} \text{grad} \hat{I}(\mathbf{x} + \mathbf{u}) j(\mathbf{x}) d\mathbf{x} \right) \right] \quad (8)$$

Derivative of the segmentation terms Just as in Section 4.2.1.2, for sake of simplicity, let us first treat the case that deals with global statistics.

$$\frac{\partial E_{seg}}{\partial p} = \frac{\partial E_{seg_global_in}}{\partial p} + \frac{\partial E_{seg_global_out}}{\partial p} \quad (9)$$

Taking the first variation of $E_{seg_global_in}$ (4.23) w.r.t. p yields:

$$\frac{\partial E_{seg_global_in}}{\partial p} = \frac{\partial (S\hat{I}\hat{I}_{in})}{\partial p} - \frac{\partial \left(\frac{S\hat{I}_{in}^2}{N_{in}} \right)}{\partial p} \quad (10)$$

where

$$\frac{\partial (S\hat{I}\hat{I}_{in})}{\partial p} = \int_{\Omega} \hat{I}^2(\mathbf{x} + \mathbf{u}) \frac{\partial H(\hat{\Phi}(\mathbf{x} + \mathbf{u}))}{\partial p} d\mathbf{x} + \int_{\Omega} H(\hat{\Phi}(\mathbf{x} + \mathbf{u})) \frac{\partial \hat{I}^2(\mathbf{x} + \mathbf{u})}{\partial p} d\mathbf{x} \quad (11)$$

$$\begin{aligned} &= \int_{\Omega} \hat{I}^2(\mathbf{x} + \mathbf{u}) \underbrace{\frac{\partial H}{\partial \hat{\Phi}} \frac{\partial \hat{\Phi}}{\partial \mathbf{x}}}_{\text{grad} \hat{\Phi}} \bigg|_{\mathbf{x}+\mathbf{u}} \underbrace{\frac{\partial (\mathbf{x} + \mathbf{u})}{\partial p}}_{j(\mathbf{x})} d\mathbf{x} \\ &\quad + \int_{\Omega} H(\hat{\Phi}(\mathbf{x} + \mathbf{u})) \underbrace{\frac{\partial \hat{I}^2}{\partial \hat{I}} \frac{\partial \hat{I}}{\partial \mathbf{x}}}_{\text{grad} \hat{I}(\mathbf{x}+\mathbf{u})} \bigg|_{\mathbf{x}+\mathbf{u}} \frac{\partial (\mathbf{x} + \mathbf{u})}{\partial p} d\mathbf{x} \end{aligned} \quad (12)$$

$$\begin{aligned} &= \int_{\Omega} \delta \hat{\Phi}(\mathbf{x} + \mathbf{u}) \text{grad} \hat{\Phi} j(\mathbf{x}) \hat{I}^2(\mathbf{x} + \mathbf{u}) d\mathbf{x} \\ &\quad + 2 \int_{\Omega} H(\hat{\Phi}(\mathbf{x} + \mathbf{u})) \hat{I}(\mathbf{x} + \mathbf{u}) \text{grad} \hat{I}(\mathbf{x} + \mathbf{u}) j(\mathbf{x}) d\mathbf{x} \end{aligned} \quad (13)$$

and

$$\begin{aligned} \frac{\partial \left(\frac{S\hat{I}_{in}^2}{N_{in}} \right)}{\partial p} &= + \frac{1}{\hat{N}_{in}^2} \left[2\hat{N}_{in} \cdot S\hat{I}_{in} \left(\int_{\Omega} \delta \hat{\Phi}(\mathbf{x} + \mathbf{u}) \text{grad} \hat{\Phi} j(\mathbf{x}) \hat{I}(\mathbf{x} + \mathbf{u}) d\mathbf{x} \right. \right. \\ &\quad \left. \left. + \int_{\Omega} H(\hat{\Phi}(\mathbf{x} + \mathbf{u})) \text{grad} \hat{I}(\mathbf{x} + \mathbf{u}) j(\mathbf{x}) d\mathbf{x} \right) \right. \\ &\quad \left. - S\hat{I}_{in}^2 \int_{\Omega} \delta \hat{\Phi}(\mathbf{x} + \mathbf{u}) \text{grad} \hat{\Phi} j(\mathbf{x}) d\mathbf{x} \right] \end{aligned} \quad (14)$$

Similarly,

$$\frac{\partial E_{seg_global_out}}{\partial p} = \frac{\partial (S\hat{I}_{out})}{\partial p} - \frac{\partial \left(\frac{S\hat{I}_{out}^2}{\hat{N}_{out}} \right)}{\partial p} \quad (15)$$

where

$$\begin{aligned} \frac{\partial (S\hat{I}_{out})}{\partial p} = & - \int_{\Omega} \delta \hat{\Phi}(\mathbf{x} + \mathbf{u}) \text{grad} \hat{\Phi} j(\mathbf{x}) \hat{I}^2(\mathbf{x} + \mathbf{u}) \, d\mathbf{x} \\ & + 2 \int_{\Omega} \left[1 - H(\hat{\Phi}(\mathbf{x} + \mathbf{u})) \right] \hat{I}(\mathbf{x} + \mathbf{u}) \text{grad} \hat{I}(\mathbf{x} + \mathbf{u}) j(\mathbf{x}) \, d\mathbf{x} \end{aligned} \quad (16)$$

and

$$\begin{aligned} \frac{\partial \left(\frac{S\hat{I}_{out}^2}{\hat{N}_{out}} \right)}{\partial p} = & + \frac{1}{\hat{N}_{out}^2} \left[2\hat{N}_{out} \cdot S\hat{I}_{out} \left(- \int_{\Omega} \delta \hat{\Phi}(\mathbf{x} + \mathbf{u}) \text{grad} \hat{\Phi} j(\mathbf{x}) \hat{I}(\mathbf{x} + \mathbf{u}) \, d\mathbf{x} \right. \right. \\ & \left. \left. + \int_{\Omega} \left[1 - H(\hat{\Phi}(\mathbf{x} + \mathbf{u})) \right] \text{grad} \hat{I}(\mathbf{x} + \mathbf{u}) j(\mathbf{x}) \, d\mathbf{x} \right) \right. \\ & \left. - S\hat{I}_{out}^2 \int_{\Omega} \delta \hat{\Phi}(\mathbf{x} + \mathbf{u}) \text{grad} \hat{\Phi} j(\mathbf{x}) \, d\mathbf{x} \right] \end{aligned} \quad (17)$$

(18)

With local statistics, and by neglecting the first variations of $\delta \hat{\Phi}(\mathbf{x} + \mathbf{u})$ and $\mathcal{B}(\mathbf{x} + \mathbf{u}, \mathbf{y} + \mathbf{u})$ w.r.t. p , Equation 9 becomes:

For $p \in \{p_1, \dots, p_m\}$,

$$\frac{\partial E_{seg}}{\partial p} = \frac{\partial E_{seg_local_in}}{\partial p} + \frac{\partial E_{seg_local_out}}{\partial p} \quad (19)$$

where

$$\begin{aligned}
& \frac{\partial E_{seg_local_in}}{\partial p} \\
&= \int_{\Omega} \delta \Phi(\mathbf{x} + \mathbf{u}) \left[\int_{\Omega} \mathcal{B}(\mathbf{x} + \mathbf{u}, \mathbf{y} + \mathbf{u}) \delta \hat{\Phi}(\mathbf{y} + \mathbf{u}) \operatorname{grad} \hat{\Phi} j(\mathbf{y}) \hat{I}^2(\mathbf{y} + \mathbf{u}) \, d\mathbf{y} \right. \\
&+ 2 \int_{\Omega} \mathcal{B}(\mathbf{x} + \mathbf{u}, \mathbf{y} + \mathbf{u}) H(\hat{\Phi}(\mathbf{y} + \mathbf{u})) \hat{I}(\mathbf{y} + \mathbf{u}) \operatorname{grad} \hat{I}(\mathbf{y} + \mathbf{u}) j(\mathbf{y}) \, d\mathbf{y} \\
&- \frac{1}{\hat{N}_{in_local}(\mathbf{x} + \mathbf{u})^2} \left[2 \hat{N}_{in_local}(\mathbf{x} + \mathbf{u}) \cdot S \hat{I}_{in_local}(\mathbf{x} + \mathbf{u}) \right. \\
&\quad \times \left(\int_{\Omega} \mathcal{B}(\mathbf{x} + \mathbf{u}, \mathbf{y} + \mathbf{u}) \delta \hat{\Phi}(\mathbf{y} + \mathbf{u}) \operatorname{grad} \hat{\Phi} j(\mathbf{y}) \hat{I}(\mathbf{y} + \mathbf{u}) \, d\mathbf{y} \right. \\
&\quad \left. + \int_{\Omega} \mathcal{B}(\mathbf{x} + \mathbf{u}, \mathbf{y} + \mathbf{u}) H(\hat{\Phi}(\mathbf{y} + \mathbf{u})) \operatorname{grad} \hat{I}(\mathbf{y} + \mathbf{u}) j(\mathbf{y}) \, d\mathbf{y} \right) \\
&\quad \left. - S \hat{I}_{in_local}(\mathbf{x} + \mathbf{u})^2 \int_{\Omega} \mathcal{B}(\mathbf{x} + \mathbf{u}, \mathbf{y} + \mathbf{u}) \delta \hat{\Phi}(\mathbf{y} + \mathbf{u}) \operatorname{grad} \hat{\Phi} j(\mathbf{y}) \, d\mathbf{y} \right] \Bigg] d\mathbf{x}
\end{aligned}$$

(20)

and

$$\begin{aligned}
& \frac{\partial E_{seg_local_out}}{\partial p} \\
&= \int_{\Omega} \delta \Phi(\mathbf{x} + \mathbf{u}) \left[- \int_{\Omega} \mathcal{B}(\mathbf{x} + \mathbf{u}, \mathbf{y} + \mathbf{u}) \delta \hat{\Phi}(\mathbf{y} + \mathbf{u}) \operatorname{grad} \hat{\Phi} j(\mathbf{y}) \hat{I}^2(\mathbf{y} + \mathbf{u}) \, d\mathbf{y} \right. \\
&+ 2 \int_{\Omega} \mathcal{B}(\mathbf{x} + \mathbf{u}, \mathbf{y} + \mathbf{u}) \left[1 - H(\hat{\Phi}(\mathbf{y} + \mathbf{u})) \right] \hat{I}(\mathbf{y} + \mathbf{u}) \operatorname{grad} \hat{I}(\mathbf{y} + \mathbf{u}) j(\mathbf{y}) \, d\mathbf{y} \\
&- \frac{1}{\hat{N}_{out_local}(\mathbf{x} + \mathbf{u})^2} \left[2 \hat{N}_{out_local}(\mathbf{x} + \mathbf{u}) \cdot S \hat{I}_{out_local}(\mathbf{x} + \mathbf{u}) \right. \\
&\quad \times \left(- \int_{\Omega} \mathcal{B}(\mathbf{x} + \mathbf{u}, \mathbf{y} + \mathbf{u}) \delta \hat{\Phi}(\mathbf{y} + \mathbf{u}) \operatorname{grad} \hat{\Phi} j(\mathbf{y}) \hat{I}(\mathbf{y} + \mathbf{u}) \, d\mathbf{y} \right. \\
&\quad \left. + \int_{\Omega} \mathcal{B}(\mathbf{x} + \mathbf{u}, \mathbf{y} + \mathbf{u}) \left[1 - H(\hat{\Phi}(\mathbf{y} + \mathbf{u})) \right] \operatorname{grad} \hat{I}(\mathbf{y} + \mathbf{u}) j(\mathbf{y}) \, d\mathbf{y} \right) \\
&\quad \left. - S \hat{I}_{out_local}(\mathbf{x} + \mathbf{u})^2 \int_{\Omega} \mathcal{B}(\mathbf{x} + \mathbf{u}, \mathbf{y} + \mathbf{u}) \delta \hat{\Phi}(\mathbf{y} + \mathbf{u}) \operatorname{grad} \hat{\Phi} j(\mathbf{y}) \, d\mathbf{y} \right] \Bigg] d\mathbf{x}
\end{aligned}$$

(21)

CV

Christine BOYDEV

Chemin du Vaugueny, 15
1066 Epalinges
Suisse
Tél : +41 (0)78 661 65 33
Email : boydevchristina@gmail.com

Nationalité française
29 juin 1984

EDUCATION

- | | |
|----------------------------|----------------------------------------------------------------------------------------------------------------------------------------------------------------------------------------------------------------------------------------------------------------------------------------------------------------------------------------------------------------------------------------------------------------------------------------------------------------------------------------------------------------------------------------------------------------------------------------------------------------------------------------------------------------------------------------------------------------------------------------------------------------------------------|
| Mai 2011 -
Aujourd'hui | Doctorat sur le thème : « Automatic segmentation of cone-beam computed tomography images for prostate cancer radiation therapy ». (Soutenance prévue en décembre 2015)
Co-encadrement : <ul style="list-style-type: none">• le Laboratoire de Traitement des Signaux (LTS5) de l'Ecole Polytechnique Fédérale de Lausanne (EPFL), Suisse
(Prof. Jean-Philippe Thiran, jean-philippe.thiran@epfl.ch)• le Laboratoire d'Automatique, de Mécanique et d'Informatique Industrielles et Humaines (LAMIH) de l'Université de Valenciennes et du Hainaut-Cambrésis, France
(Prof. Abdelmalik Taleb-Ahmed, taleb@univ-valenciennes.fr) |
| Sept. 2009 -
Déc. 2010 | Formation DQPRM (Diplôme de Qualification en Physique Radiologique et Médicale) : 2 mois de cours à l'INSTN (Saclay) suivis de 12 mois de stage au Centre de lutte contre le cancer Léon Bérard (Lyon) |
| Sept. 2008 -
Sept. 2009 | Master M2 Recherche de Physique Médicale à l'Université Paris-Sud 11 (Orsay) |
| Sept. 2007 -
Juin 2008 | Année d'échange à Imperial College London , Département de Physique (Programme ERASMUS) |
| 2005 - 2008 | Etudes d'ingénieur à l' ENSPG (Ecole Nationale Supérieure de Physique de Grenoble, renommée PHELMMA)
Filière "Instrumentation pour les Biotechnologies" |
| 2002 - 2005 | Classes préparatoires aux Grandes Ecoles (filières PCSI-PC) au lycée Saint-Louis (Paris VI) |

Juin 2002 Baccalauréat général S, option mathématiques, mention bien

1995 - 2002 Collège et lycée aux Maisons d'Education de la Légion d'Honneur

Langues :	Français et bulgare	- Bilingue
	Anglais	- Très bon niveau
	Espagnol	- Bon niveau
	Russe	- Niveau scolaire

Programmation : C++ (ITK), Python, R, Bash, LaTeX

Systèmes d'exploitation : Linux, Windows

ECOLE D'ETE

28 Juillet – 1er août 2014 (1 semaine) :

- « Medical Imaging Summer School 2014 »
- Organisation : University of Catania, Italie

22 Juillet – 9 Août 2013 (3 semaines) :

- « Graduate Summer School: Computer Vision at Institute for Pure and Applied Mathematics (IPAM) »
- Organisation : Prof. Alan Yuille (University of California, Los Angeles (UCLA), USA)

8-12 Juillet 2013 (1 semaine) :

- « 2nd Biomedical Image Analysis Summer School: Modalities, Methodologies & Clinical Research »
- Organisation : Prof. Nikos Paragios (Ecole Centrale Paris, France)

EXPERIENCE PROFESSIONNELLE

Févr. 09 – Août 09 **Stage recherche à l'hôpital MCH Westeinde à la Haye (Pays-Bas)**

- Domaine : Assurance qualité des traitements de Radiothérapie Conformationnelle à Modulation d'Intensité (RCMI)
- Mission : Mettre en place une méthode de validation expérimentale des plans de traitement avec modulation d'intensité (RCMI) sur les accélérateurs linéaires des marques Elekta et Novalis (comparaison

calculs/mesures), en vue de remplacer la dosimétrie par films radiographiques.

- Matériel et méthodes : Comparaison des propriétés dosimétriques de trois matrices de détecteurs 2D différentes (chambres d'ionisation: l'mRT MatriXX et 2D-ARRAY seven29; diodes: MapCheck2) et de l'EPID de type iViewGT monté sur l'accélérateur linéaire Elekta. Utilisation de concepts de traitement du signal (condition de Nyquist). Variables considérées : distance entre chaque détecteur et taille de chaque détecteur.
- Résultats : Etude de l'influence des différentes interpolations effectuées par chaque matrice de détecteurs lors du calcul de l'index gamma visant à comparer les distributions de dose calculées par le système de planification de traitement et les distributions de dose mesurées.
- Direction : Anna en Andrei Petoukhov (petoukhovs@hotmail.com)

**Nov. 07 – Mai 08 Projet de fin d'études à Imperial College London,
Department of Bioengineering (Royaume-Uni)**

- Domaine : Neurosciences
- Mission : Appliquer la théorie d'information à l'analyse de données enregistrant l'activité de la zone MT du cortex visuel.
- Matériel et méthodes : Programmation à l'aide de Matlab – Utilisation des concepts théoriques de la théorie d'information pour analyser les trains de potentiels d'action.
- Résultats : Construction de courbes présentant les réponses des neurones du système visuel à différents stimuli dynamiques selon deux points de vue algorithmiques différents : *the spike counting code, and the spike timing code*.
- Direction : Simon Schultz (s.schultz@imperial.ac.uk)

Juin 07 – Août 07 Stage recherche à l'Institut d'Optique à Palaiseau (France)

- Domaine : Tomographie par Cohérence Optique (technique d'imagerie des milieux biologiques capable d'explorer des profondeurs allant jusqu'au mm).
- Mission : Tester une nouvelle source lumineuse capable de soumettre l'objet biologique en mouvement à des temps d'exposition très brefs (une combinaison de diodes électroluminescentes émettant dans l'infrarouge).
- Matériel et méthodes : Simulation à l'aide de Matlab – Test de la nouvelle source lumineuse – Expériences sur des têtards.
- Résultats : Création et test de la nouvelle source lumineuse. Comparaison avec les simulations. Mise en évidence des avantages et inconvénients de cette source vis-à-vis de la source halogène anciennement utilisée.
- Direction : Arnaud Dubois (arnaud.dubois@institutoptique.fr)

Juil 06 – Août 06 **Stage recherche au laboratoire U2R2M (CNRS) à Orsay (France)**

- Mission : Programmer trois types de séquences IRM en vue de faire de l'imagerie médicale par RMN sur l'Hélium 3 hyperpolarisé, gaz injecté dans les poumons (à faible champ: 0.1 Tesla).
- Matériel et méthodes : Expériences en élastographie sur un imageur 0.1 Tesla. Utilisation de Matlab pour la programmation et du logiciel NTNMR pour écrire les séquences IRM.
- Résultats : Deux séquences sur trois programmées, et testées. Mise en évidence de leurs avantages et inconvénients.
- Direction : Xavier Maître (Xavier.Maitre@u2r2m.u-psud.fr)

EMPLOIS OCCASIONNELS

- Août 2005 Relation clientèle à la Société Générale (agence d'Enghien-les-Bains, 95)
- Août 2004 Standard et archivage à la société Safège, entreprise d'ingénierie dans le génie civil (Nanterre, 92)
- Août 2003 Travail au service reprographie de la société Safège (Nanterre, 92)

CENTRES D'INTERET

Natation, tennis
Lecture
Musées

PUBLICATIONS

Articles de revues internationales avec comité de sélection :

- C. Boydev, A. Taleb-Ahmed, F. Derraz, L. Peyrodie, J.P. Thiran and D. Pasquier. Development of CBCT-based prostate setup correction strategies and impact of rectal distension. Radiation Oncology, 2015. doi.org/10.1186/s13014-015-0386-8
- F. Derraz, A. Taleb-Ahmed, A. Chikh, C. Boydev, L. Peyrodie, and G. Forzy. Segmentation of Prostate Using Interactive Finsler Active Contours and Shape Prior. Image and Signal Processing, Lecture Notes in Computer Science, vol. 7340, 2012, pp 397-405. [doi:10.1007/978-3-642-31254-0_45](https://doi.org/10.1007/978-3-642-31254-0_45)

Article de revue nationale française avec comité de sélection :

- N. Zahra, C. Monnet, E. Bartha, G. Bouilhol, C. Boydev, M. Courbis, M. Le Grévellec, M. Bosset, M. Zouai, B. Fleury et S. Clippe. Tomographie conique quotidienne pour les traitements pelviens et prostatiques : étude interobservateurs. Cancer/Radiothérapie, 19(5), 303-307.

Articles de conférences internationales avec comités de sélection :

- C. Boydev, D. Pasquier, F. Derraz, L. Peyrodie, A. Taleb-Ahmed and J.P. Thiran. A comparison of rigid registration methods for prostate localization on CBCT and the dependence on rectum distension. In Journal of Physics: Conference Series (Vol. 489, No. 1, p. 012025). IOP Publishing. In 2013 International Conference on the Use of Computers in Radiation Therapy. [doi:10.1088/1742-6596/489/1/012025](https://doi.org/10.1088/1742-6596/489/1/012025)
- C. Boydev, D. Pasquier, F. Derraz, L. Peyrodie, A. Taleb-Ahmed and J.P. Thiran. Automatic Prostate Segmentation in Cone-Beam Computed Tomography Images using Rigid Registration. In Engineering in Medicine and Biology Society (EMBC), 2013 35th Annual International Conference of the IEEE, pp 3993-3997. [doi:10.1109/EMBC.2013.6610420](https://doi.org/10.1109/EMBC.2013.6610420)

Résumé de conférence nationale française avec comité de sélection :

- C. Boydev, A. Taleb-Ahmed, F. Derraz, L. Peyrodie, J.P. Thiran et D. Pasquier. Développement d'une méthode de recalage automatique rigide pour la radiothérapie prostatique guidée par l'image. Cancer/Radiothérapie, 18(5), pp 611-612. doi.org/10.1016/j.canrad.2014.07.076

Article de revue internationale sans comité de sélection :

- C. Boydev, D. Pasquier, F. Derraz, L. Peyrodie, A. Taleb-Ahmed and J.P. Thiran. Shape-based Interpolation of a Set of 2D Slices. The Insight Journal, 2012 January-December, <http://hdl.handle.net/10380/3390>